UNIVERSIDADE DE SÃO PAULO
INSTITUTO DE FÍSICA DE SÃO CARLOS

Maria Carolina Kherlakian

Indirect dark matter searches in ultra faint dwarf galaxies

São Carlos

2020

Maria Carolina Kherlakian

Indirect dark matter searches in ultra faint dwarf galaxies

Dissertation presented to the Graduate Program in Physics at the Instituto de Física de São Carlos, Universidade de São Paulo, to obtain the degree of Master of Science.

Concentration area: Basic Physics

Advisor: Prof. Dr. Vitor de Souza
Co-advisor: Dr. Aion Viana

Corrected version
(Original version available on the Program Unit)

São Carlos
2020

Ficha catalográfica revisada pelo Serviço de Biblioteca e Informação Prof. Bernhard Gross, com os dados fornecidos pelo(a) autor(a)

Kherlakian, Maria Carolina
Indirect dark matter searches in ultra faint dwarf galaxies / Maria Carolina Kherlakian ; advisor Prof. Dr. Vitor de Souza; co-advisor Dr. Aion Viana. – corrected version – São Carlos, 2020.
119 p.

Dissertation (Masters - Graduate Program in Basic Physics) – Instituto de Física de São Carlos, Universidade de São Paulo, 2020.

1. Dark matter indirect searches. 2. The Cherenkov Telescope Array. 3. Milky Way satellites. 4. Dwarf galaxies. I. de Souza, Vitor, advisor. II. Viana, Aion, co-advisor. III. Title.

ACKNOWLEDGEMENTS

First, I want to thank Prof. Vitor de Souza for guiding me through this dissertation. He believed in my potential and always pushed me further to be a better professional and make better choices in my career. Not only the compliments made me develop as a scientist but also the criticism was of vital importance to me. I also thank him for treating his students like a big family and for the enriching coffee break talks that made me grow as an individual as well. His support just made me be where I am today. I also want to show my gratitude for Prof. Aion Vianna, who was my co-supervisor. His suggestions and clarifications were essential for the development of this project.

I express my full gratitude for my parents, Eduardo and Adriana, my brother Eduardo and my grandmother Maria Aparecida, for always being there for me and never measuring efforts to support me in my education. For all my friends, who made life funnier during this time, a huge thanking. Special greetings for Marcin Jurke, who made time much lighter when I was writing this dissertation.

For all the scientific conversations and get-togethers during this 1 and a half year, I thank my coworkers from the Astrophysics group of the Physics Institution of São Paulo (IFSC). In particular, thanks go for Dr. Humberto Martinez, Rodrigo Lang, Luan Arbeletche and Edyvania Emily Martins for being my friends and for always being available to clear up my questions.

I acknowledge all the staff and professors from IFSC, Dr. Miguel A. Sánchez-Conde, Dr. Tibaldo Luigi, who clarified a lot of questions at the CTOOLS forum, and Dr. Oliver Newton, who clarified very important topics.

Finally, but actually the most important, I thank all Brazilian citizens that supported both the University of São Paulo and the São Paulo Research Foundation, that funded this master project through process 2018/25793-7.

"Slow down, you crazy child
You're so ambitious for a juvenile
But then if you're so smart, then tell me
Why are you still so afraid?"
Billy Joel

ABSTRACT

KHERLAKIAN, M. C. **Indirect dark matter searches in ultra faint dwarf galaxies**. 2020. 119p. Dissertation (Master of Science) - Instituto de Física de São Carlos, Universidade de São Paulo, São Carlos, 2020.

The nature of dark matter is still one of the biggest mysteries of modern cosmology. Unveiling its complexion through indirect observations of gamma-rays requires state of the art observatories, such as the Cherenkov Telescope Array (CTA). The Milky Way satellites constitute a promising target for the search of Weakly Interacting Massive Particles (WIMPs) via indirect searches due to their low astrophysical background. However, the overall census of the dark matter galactic substructures is incomplete. This is owing to the sky coverage and sensitivity limitations of sky-survey experiments. Moreover, N-body simulations indicate that a much higher number of satellites should exist. In this work we present a modelling of the galactic sub-clumps based on statistical estimations of the full Milky Way satellite population. We introduce 10 substructure modellings (SM_i, $i \in \{1, \ldots, 10\}$) with the following varying parameters: the substructure inner dark matter profile, its mass and radial distribution around the Milky Way, the expected number of satellites given by various studies and the mass-concentration relation. We simulate hundreds of skymaps with the `CLUMPY` code based on the sub-halo modellings. We show that the mass-concentration parametrization and the predicted number of sub-halos handed over the most substantial effects on the source J-factor. The sources are then used to investigate the detectability of sub-halos with the CTA. We assume two cases: if a dark matter signal is seen by the CTA or if there is no detection. For both we calculate the sensitivity curves of sources resolved in the simulations for the $\tau^+\tau^-$ and $b\bar{b}$ channels. In general, the $\tau^+\tau^-$ channel maintained the most constrained sensitivity curves. There was no substantial difference on the sensitivity curve for sources placed on the north and south hemisphere. In the case of detection of a signal with the CTA, no model was effective to access the thermal values of $\langle\sigma v\rangle$. In case of no signal observation, only the model with the highest median J-factcor could probe the thermal values of $\langle\sigma v\rangle$.

Keywords: Dark matter indirect searches. The Cherenkov Telescope Array. Milky Way satellites. Dwarf galaxies.

RESUMO

KHERLAKIAN, M. C. **Busca indireta de matéria escura em galáxias anãs ultra-fracas**. 2020. 119p. Dissertação (Mestrado em Ciências) - Instituto de Física de São Carlos, Universidade de São Paulo, São Carlos, 2020.

A natureza da matéria escura ainda é um dos maiores mistérios da astrofísica moderna. Revelar sua compleição através de observações indiretas de raios gama requer observatórios de última geração, como o CTA (Cherenkov Telescope Array). Os satélites da Via Láctea constituem um alvo promissor para a busca de Partículas Massivas que Interagem Fracamente (WIMPs) através de buscas indiretas devido ao seu baixo ruído astrofísico. Entretanto, o censo geral das subestruturas galácticas de matéria escura é incompleto. Isso se deve a incompleta cobertura do céu e às limitações de sensibilidade dos experimentos de busca de objetos extragalácticos. Além disso, as simulações de N-corpos indicam que deveria existir um número muito maior de satélites. Neste trabalho apresentamos uma modelagem dos subgrupos galácticos com base em estimativas estatísticas da população total de satélites da Via Láctea. Introduzimos 10 modelos de subestruturas (SM_i, $i \in \{1, ..., 10\}$) com os seguintes parâmetros variáveis: o perfil da subestrutura interna de matéria escura, sua massa e distribuição radial em torno da Via Láctea, o número esperado de satélites dado por differentes estudos e a parametrização entre a massa e concentração de subestruturas. Simulamos centenas de mapas do céu com o código `CLUMPY` baseando-nos em modelos de subestruturas. Mostramos que a parametrização entre massa e concentração e o número previsto de satélites geram os efeitos mais substanciais sobre o fator J da fonte. As subestruturas são então utilizadas para investigar a detectabilidade de sub-halos com a CTA. Supomos dois casos: se um sinal de matéria escura é visto pela CTA ou se não há detecção. Para ambos, calculamos as curvas de sensibilidade das fontes resolvidas nas simulações para os canais de aniquilação $\tau^+\tau^-$ e $b\bar{b}$. Em geral, o canal de $\tau^+\tau^-$ manteve as curvas de sensibilidade mais restritas. Não houve diferença subestancial na curva de sensibilidade das fontes posicionadas nos hemisférios norte e sul. No caso da detecção de um sinal com a CTA, nenhum modelo foi eficaz em acessar os valores térmicos de $\langle\sigma v\rangle$. Em caso de não observação do sinal, somente o modelo com a mediana mais alta do fator J poderia sondar os valores térmicos de $\langle\sigma v\rangle$.

Palavras-chave: Buscas indiretas de matéria escura. Cherenkov Telescope Array. Satélites da Via Láctea. Galáxias anãs.

LIST OF FIGURES

LIST OF TABLES

CONTENTS

1 INTRODUCTION

It is known for some decades now that around 26 % of the total energy density of the Universe (1) is made of a mysterious particle called dark matter, which does not emit or absorb light. In the 1930s the first evidence for the existence of dark matter was seen through the measurements of the mass-to-light ratio of the Coma cluster, made by Fritz Zwicky. (2) A few decades later, Vera Rubin brought to light more evidence for the existence of a non-luminous matter through the measurement of the rotation curve of galaxies. (3, 4) Her results showed that the circular velocity of stars in a galaxy is not compatible with the mass that is calculated by analysing the light from these objects. To explain why rotation curves follow a flat-like behaviour as stars get farther from the galactic center, it is required that most of the matter in a galaxy can not be seen through light.

With the improvement of sophisticated experiments and computational simulations, it is known that dark matter is partially made of non-relativistic, neutral particles, that do not interact electromagnetically, but interact weakly with itself and ordinary matter. In fact, no particle known today satisfies these conditions, therefore scientists search for dark matter beyond the Standard Model. The Weakly Interacting Massive Particles (WIMPs) (5) gained a lot of popularity in the dark matter theory. This is due to the fact that the velocity averaged cross-section of WIMPs remarkably resembles the one for weak interactions, known as the WIMP miracle. Moreover, these particles provide the right relic abundance, yielded by measurements of CMB fluctuations. (1)

Detecting a WIMP signal is a very hard task. One way of looking for it is through indirect (6) detection techniques, that search for standard model particles produced when a WIMP self-annihilates. The process of annihilation can generate pairs of stable particles, for example electrons and positrons, neutrinos and ultimately gamma-rays. The former one is a very interesting multi-messenger in astrophysics because it points directly to the source location.

WIMP annihilation, however, rarely occurs in the Universe. (7) A signal can only be seen if we look to regions rich in dark matter, such as the dwarf galaxies that orbit the Milky Way (MW). These targets also provide a clear signal due to the almost lack of astrophysical background. Unfortunately, only a partial census of satellites is known because of the limited sky area and flux sensitivity yielded by current experiments, such as the Dark Energy Survey (DES) (8) and the Sloan Digital Sky Survey (SDSS). (9) It is believed that future sky survey telescopes will be able to increase the number of Milky Way satellites.

Identifying gamma-rays is possible with third generation Imaging Atmospheric Cherenkov Telescopes (IACTs), such as the Cherenkov Telescope Array (CTA). (10) The CTA will have unprecedented sensitivity in the TeV energy scale. Its baseline design calls for 118 telescopes to be installed at two sites, covering areas of 0.6 km^2 on La Palma, Spain and 4 km^2 near Paranal, Chile. In this scenario, gamma-rays of 20 GeV up to 300 TeV will be observed with great accuracy.

This work seeks to probe the WIMP scenario by analysing the signal that could be measured by the CTA from undiscovered satellites. We do this by 1.) simulating sources of dark matter that statistically agree with data from dark matter simulations, 2.) calculating the signal of dark matter from the substructures and last, 3.) provinding the constraints on the parameter phase space of WIMP dark matter that is yielded by the CTA .

This dissertation is structured as follows: chapter 2 presents the dark matter problem, candidates, characteristics, results from numerical simulations and possible ways for WIMP detection, in particular indirect techniques. Chapter 3 establishes the principles of observing gamma-rays produced by dark matter annihilation and possible targets for IACTs, in specific the dwarf spheroidal galaxies. Chapter 4 outlines the Chrenkov Telescope Array and its prospects for probing the WIMP scenario. Chapter 5 reports the simulation of sources, calculation of the dark matter signal and the analysis pipeline. Our results are addressed in chapter 6 and conclusions, in chapter 7.

2 INTRODUCTION TO DARK MATTER PHYSICS

This chapter is dedicated to a review of the dark matter theory: its evidences (section 2.1), properties (section 2.3), candidates (section 2.3) and possible ways to detect it (section 2.4).

2.1 Evidences of dark matter

In the following section we discuss the key evidences for dark matter on galactic, extra-galactic and cosmological scales. We also review the case of the Bullet Cluster in the development of the dark matter theory.

In 1933, Fritz Zwicky (2) inferred the mass-to-light ratio of the Coma cluster from measurements of the velocity dispersion of galaxies in the cluster. Coma showed a mass-to-light ratio of 400 $M_\odot/L_\odot$, which is two orders of magnitude higher than the one in the sun neighbourhood. The mass of the cluster, calculated via virial theorem, was 10 times bigger than the one derived from the bright components in the group of galaxies, i.e., stars and gas. That was the first evidence for the existence of a non-luminous matter, today recalled as dark matter.

Some decades later, Vera Rubin showed that dark matter should also be present in individual galaxies by measuring the rotation curve (RC) of these objects. (3,4) The RC relates the circular velocity of stars and gas to their galactocentric distance. According to the Newton law, the RC should exhibit a decreasing behaviour of circular velocity as objects get further from the galactic center. Because stars from spiral galaxys have nearly circular orbits, the gravitational and centripetal forces are equal, as shown in the following equation

$$F_{grav} = F_{cent} = \frac{mv_c^2(r)}{r} = \frac{GM(r)m}{r^2} \rightarrow v_c = \sqrt{\frac{GM(r)}{r}}. \tag{2.1}$$

As a consequence, the circular velocity is proportional to the square root of the mass by the distance from the galaxy center, $v_c \propto M(r)^{1/2}/r$. As objects get further from the center, the total mass of stars and gass gets roughly constant and as a result, the circular velocity should only experience a softening behaviour due to the increase of r.

Measured circular velocities, however, get flattened for high distances from the center. This could be explained by Newtonian dynamics if the mass distribution was proportional to the galatocentric distance and, therefore, the mass density $\rho_M(r)$, to r^{-2} [1].

[1] The relation of the mass distribution $M(r)$ and mass density $\rho_M(r)$ is given by $M(r) = \int \rho_M(r)\, dV$.

The comparison of measured and expected RCs give us two possibilities: the Newtonian dynamics is incorrect or incomplete for galactic scales or there is dark matter surrounding the galaxy. Figure 1 shows the the measured values (solid line plus dots) of the RC from the NGC 3198 galaxy and single contributions from stars (dashed line), gas (dotted line) and a non-luminous component (dashed-dotted line). For radii greater than 10 kpc, the measured points follow practically a horizontal line. On the other hand, the sum of the contributions regarding stars and gas lessens after that radius. The dark matter component is responsible for the flattening of the RC.

The most recent measurement of the Milky Way's RC shows a similar nature, as presented in figure 2, where red dots are measured points, the grey shadowed area comprises the predicted behaviours from only-baryonic matter models and the black line is the fiducial model. For distances greater than 6 kpc, there is an increasing discrepancy between the expected behaviour and measured points.

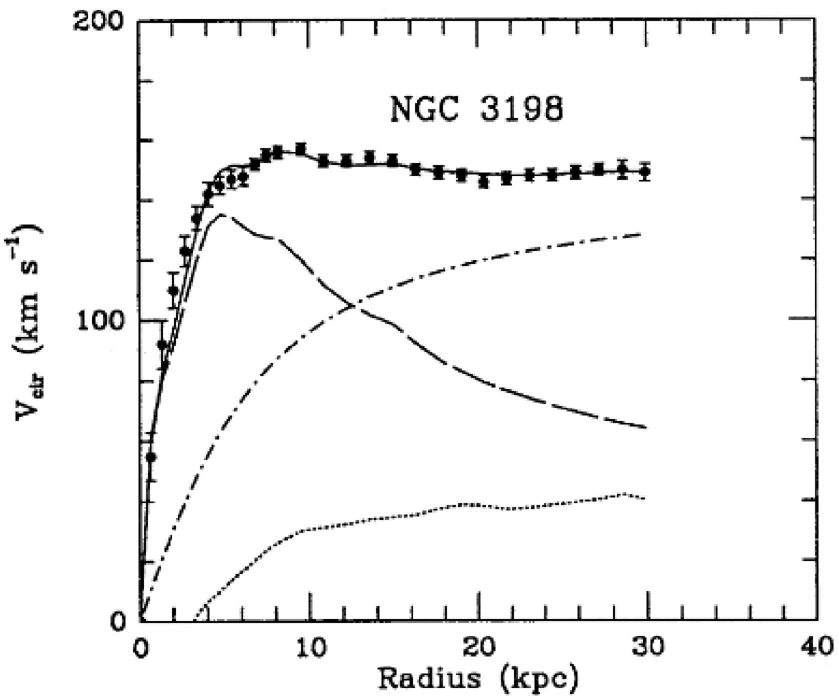

Figure 1 – Rotation curve of NGC 3198. Dashed line: contribution from star component, dotted line: contribution from gas, dashed-dotted line: contribution from non-luminous matter and solid line: sum of three components. The dots represent measured data with errors.

Source: BEGEMAN (11)

Evidences for dark matter is also present in the oscillations of the Cosmic Microwave Background (CMB). (7) The CMB is a black body radiation in the microwave spectrum, known to be isotropic up to the 10^{-5} K level. During recombination, free protons (p^+) and electrons (e^-) that existed in the hot, dense and opaque early Universe combined

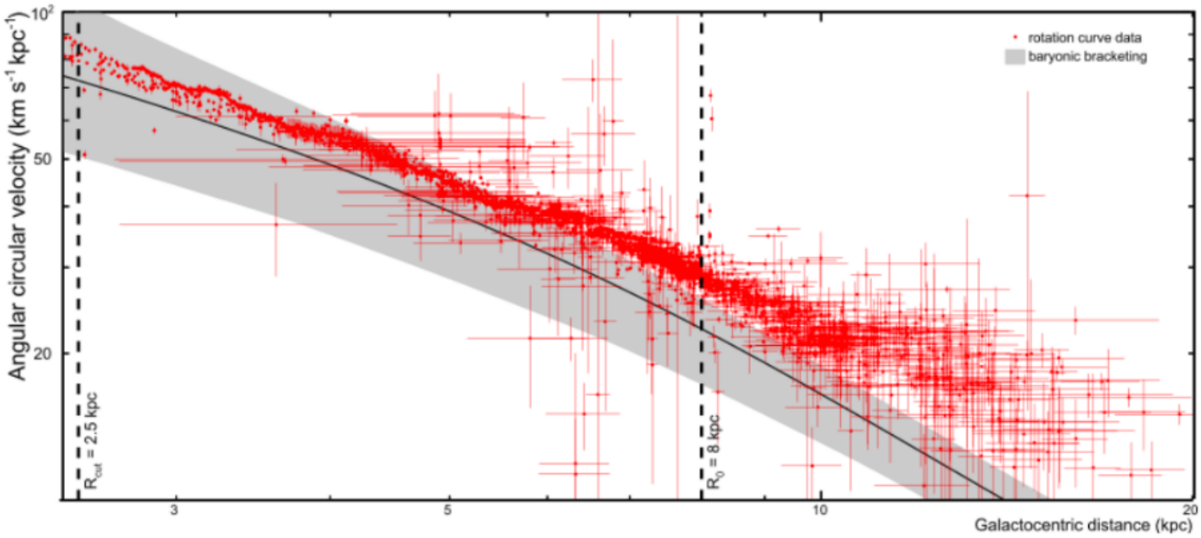

Figure 2 – The rotation curve of the Milky Way. The red dots are the measured points, the grey area contains variations of predicted RCs based on only-baryonic models and the black line is the fiducial model.

Source: IOCCO (12)

and formed neutral hydrogen atoms. As a consequence, a electromagnetic radiation in the infrared and red-optical spectrum was emitted, at a temperature of around 3000 K. This radiation was red-shifted by a factor of 1100 to the microwave spectrum. Unlike the plasma, the neutral atoms are not able to scatter thermal photons by Thomson scattering, therefore the Universe became transparent to radiation.

The CMB looks roughly uniform in all directions. However, detailed measurements show small scale variations that follow a precise shape. This pattern is the same as the one expected for a uniformly distributed gas that expanded to the size of the current observable Universe. As a matter of fact, sensitive instruments measure anisotropies in the spectral radiance of the CMB for different angles of observation in the sky. Figure 3 shows the temperature irregularities of the CMB temperature in a galactic sky-map, measured by seven years of operations of the Wilkinson Microwave Anisotropy Probe (WMAP).

The detailed temperature fluctuations detected by Planck (red dots) as a function of the angular scale and multipole moment of the multipole expansion of the CMB is presented in figure 4. The green curve represents a fit with the standard model of cosmology, that favours the Big Bang theory, while the green shaded area represents variations of the cosmological standard model that still give good fits to the Planck data.

The discovery of CMB anisotropies was of crucial importance for the confirmation of the Big Bang cosmology. In this model, it is understood that the Universe began in a dense and hot state that expands with time. The rate of expansion is determined by the types of matter and energy in the Universe and whether the total density is above, below

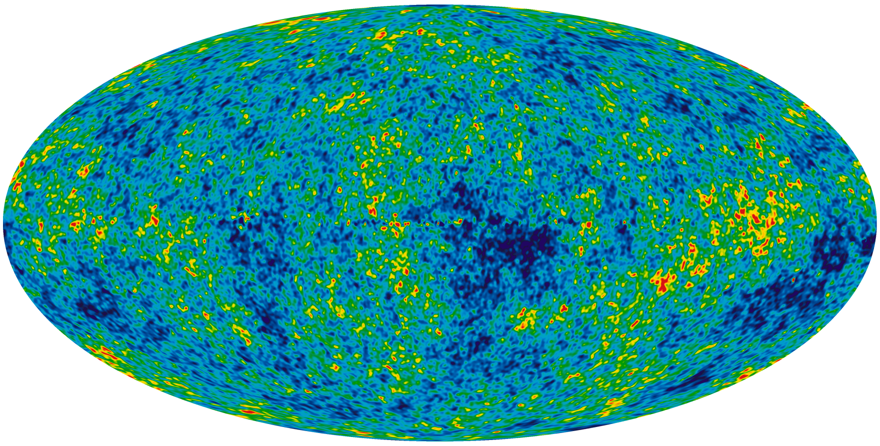

Figure 3 – The CMB temperature map in galactic coordinates. Results from seven years of WMAP operations.

Source: NASA/WMAP Science Team (13)

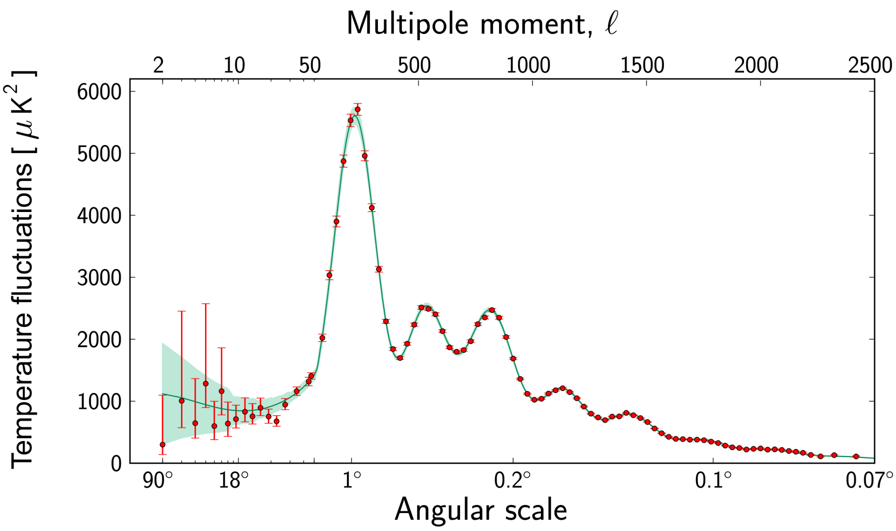

Figure 4 – The temperature fluctuations of the CMB as a function of the angular scale and multipole moment. Red dots are measured points by the Planck telescope. The green line is the fit of the measured points with the Standard Model Cosmology (SMC). The green shaded area are variations of the SMC that provide good fits of the measured points.

Source: ESA AND THE PLANCK COLLABORATION (14)

or equal to the critical density.

The cosmological principle, which is the base of most modern cosmological models, states that on large scales the Universe is isotropic and homogeneous, i.e., it looks the same from all directions and locations. Moreover, it also comprises an expanding space metric, well established by the red shift of absorbing or emitting spectral lines by distant galaxies and by the decrease in luminosity of distant type Ia supernovae [2]. While the expansion increases the distance between objects that are not gravitationally bounded, their size remains the same. In general relativity, a positive vacuum energy, recalled today as dark energy and represented by the constant Λ, can be responsible by an accelerated expansion.

The current cosmological model, known as ΛCDM (16), is a parametrisation of an Universe composed of dark energy (Λ), cold dark matter (CDM)[3], ordinary matter and radiation. The ΛCD is usually referred to as the cosmological standard model of Big Bang, since it provides the most simple explanations of the CMB, the hierarchical formation of structures, the observed abundances of light elements (H, He and Li) and the accelerated expansion of the Universe. Hierarchical structure formation predicts that dark matter clumps formed first because dark matter does not interact with radiation. Later, baryons fall in the gravitational potential of the dark clumps, when the former decouples from radiation.

Ordinary matter and radiation were strongly coupled before recombination because they interact via photon scattering on free electrons. The pressure generated by the photons in the fluid prevented baryons to couple gravitationally with dark matter and to form their own potential wells. If the Universe was composed only of baryonic matter, we should see imprints of the CMB fluctuations in the spatial distribution of galaxies. However, this was not observed.

As the structures grow bigger, small scale ones fall into their gravitational potential, forming sub-halos or streams [4]. Therefore, the Milky Way contain lots of small scale structures orbiting around it.

The fitting of the CMB according to the ΛCDM model allows the calculation of the present abundances of baryonic matter $\Omega_b = 0.0493(6)$ (1), total matter $\Omega_m = 0.315(7)$ (1) and dark energy $\Omega_\Lambda = 0.685(7)$ (1), based on the 2018 release of the Planck satellite data. Since Ω_b and Ω_m are not equal, the CMB fluctuations indicate the existence of a non-baryonic component of matter, which accounts for $\Omega_{cdm} = \Omega_m$ - $\Omega_b = 0.265(7)$. (1)

2 Supernovae are classified into type I, characterised by the absence of the Balmer hydrogen series in their spectral features, and type II, that contain these lines. More specifically, type Ia supernovae have a line at at 615.0 nm from ionised silicon Si II, observed near the peak light. The light curves of this type, which correlates the magnitude with time, are remarkably similar. This characteristic, together with their very high typical absolute B magnitude $M_B =$ -19.5 $\pm$ 0.1, enables the determination of their absolute magnitude M_V and redshift-distance relation very precisely. (15)

3 A question one may ask is in which range spans the dark matter's temperature. Dark matter created with non-relativistic velocities are cold (CDM), otherwise warm (WDM) or hot (HDM). We will address the preference for CDM in modern cosmology in the next section.

4 Streams are structures formed from remnant stars, or more rarely gas, that once composed a neighbouring galaxy or cluster that was disembowelled and stretched out due to tidal forces.

Measurements of primordial abundances of light elements also constrain Ω_b. During Big Bang nucleosynthesis, light elements, such as deuterium (^{2}H), helium (^{4}He) and lithium (^{3}Li), were created from protons and neutrons. Only the interior of stars and supernovas produce heavier elements. One important result from this study was hypothesizing that the plethora of the light elements depends critically on the density of baryonic matter (neutrons and protons) during the epoch of nucleosynthesis. Most importantly, one value of Ω_b can explain the myriad of all light elements at once. Comparing to the present day critical density of matter, the required value of Ω_b to explain the observed abundance of ^{4}He ($\sim$ 25 %), ^{2}H ($\sim$ 0.01 %) and ^{3}Li (<0.01 %) is only a few percent. This shows that not all dark matter is baryonic, i.e., it is necessary to search for exotic massive particles.

2.1.1 The case of the Bullet Cluster

In 2006 the Chandra observatory (17) presented the weak-lensing analysis of the Bullet Cluster, a merge of two clusters that collided. Through gravitational lensing and X-ray methods, it was observed that the mass of the cluster merge does not follow the distribution of the intergalactic gas, which makes up most of baryonic mass. Rather, it follows the galaxy distribution. The reconstructed gravitational potential (green lines) and gas dominated regions (white areas) identified via X-ray emissions of gas is shown in figure 5.

If dark matter should interact with the ordinary one, there should be only one potential peak, following the intergalactic gas distribution. With 8σ confidence level (C. L.), the separation between the peak of the total mass and the baryonic mass could not be explained by different gravitational models. Therefore, most matter of the Bullet Cluster should be non-luminous. Moreover, the results show that when dark and ordinary matter collide, the intergalactic gas sticks together and heats, while galaxies and dark matter pass through with no interaction. This fact is responsible for the bullet aspect of cluster merges.

2.2 Review of simulations of dark matter

Numerical studies of galactic halos give important information about the dark matter nature. They test big structures hierarchical formation, dark matter distribution in galaxies and substructures properties. With computational power advancing, it is possible to resolve simulations of bigger parts of the Universe with higher resolution. In present date, the biggest challenge is actually to create simulations that combine both dark and normal matter.

In the early 1980s, the first simulations of cold dark matter were carried out with just a few hundred particles. In these, clustering of galaxies were simulated in specific cubes of the Universe. One important result was the confirmation of the growing hierarchical feature of cold dark matter, in which small structures form first because of self gravity

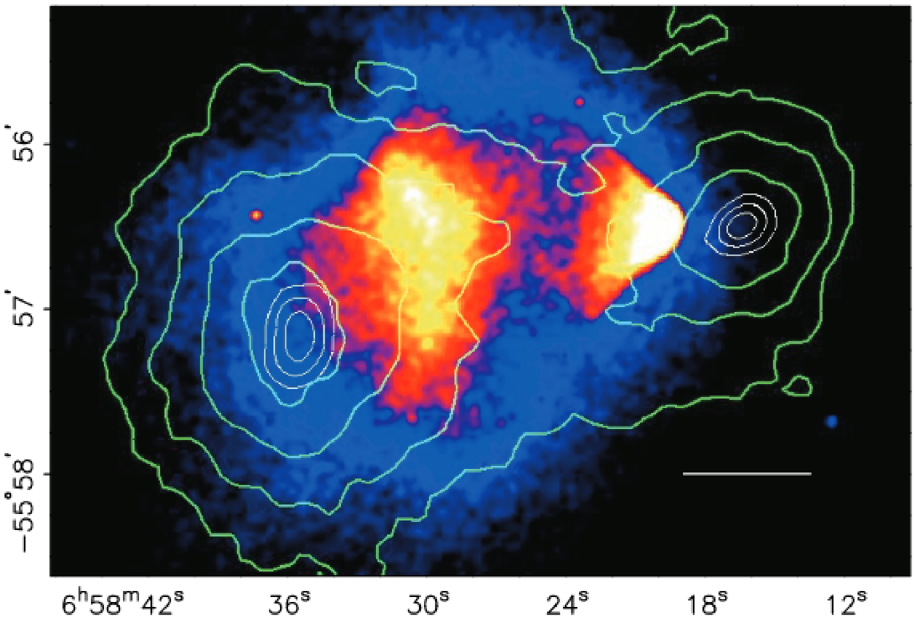

Figure 5 – The gravitational potential of the Bullet Cluster in angular coordinates, measured by weak-lensing methods and X-ray emissions from gas. The green lines represent the measured gravitational potential and white areas represent the gas distribution.

Source: CLOWE (17)

and after they merge to form bigger and more massive objects. WDM became disfavoured because it would be too fast to be confined in low mass over-densities, since its velocity is higher than the scape velocity of small structures.

Although cold dark matter agrees with the development of cosmological large-scale structures, three paradigms of results from CDM simulations have to be noted. First, CDM simulations produce halos with cusp profiles, while observations show that they should be smooth in the center. This is known as the cusp halo problem. Another paradigm is the missing satellites problem. High resolution simulations of the Milky Way resolve thousand to millions of substructures, while up to now sky-survey experiments, for example the Dark Energy Survey (DES) (8) and Sloan Digital Sky Survey SDSS (9), found only a few dozens. This question could be sorted out with the argument that many more satellites of the Milky Way indeed exist but we are not able to detect them because they lost their star component due to tidal forces. This explanation, however, creates a new question: the too big to fail problem. This dilemma atests that the resolved Mily Way substructures are just too big to not have visible stars. Another way to cope with this problem is noticing that the observed satellites are not massive enough to be consistent with the simulations.

In 1991, Dubinski and Carlberg (18) were the first ones to run simulations that effectively resolved the shapes of dark halos. Using up to 3 $\times 10^5$ particles, they showed that the mass density in dark halos vary with the radial distance from the center, as shown in figure 6.

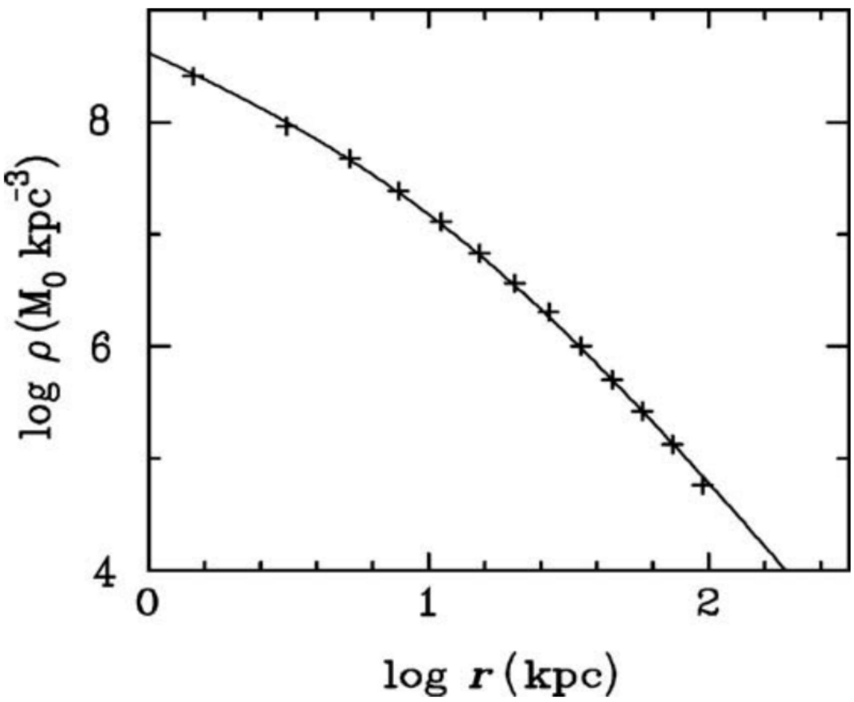

Figure 6 – Density profile of the simulation from Dubinski and Carlberg (1991) (crosses) and best fit with NFW profile.

Source: BERTONE (7)

In 1995, Navarro-Frenk-White (NFW) (19) showed that from single galaxies to galaxy clusters, one function, that peaks as r^{-1} at the disk center, can well fit the dark matter distribution from simulated halos. This function is expressed in equation 2.2.

$$\rho_{NFW} = \frac{\rho_s}{\left(\frac{r}{r_s}\right)\left(1 + \frac{r}{r_s}\right)^2}. \tag{2.2}$$

Other profiles for dark matter distribution have been proposed through time, either from simulations, either from fitting observations. For example, the Einasto (20) parametrisation,

$$\rho_{Ein} = \rho_s \; exp\left[-\frac{2}{\alpha}\left(\frac{r}{r_s}\right)^{\alpha}\right], \tag{2.3}$$

suggests a flat behaviour close to the disk center, unlike the NFW that tends to infinity in that region. A classification according to the behavior of dark matter close to the center of the halo was conceived: cored profiles, like Einasto, present a smoother dark matter behavior close to the center. On the other hand, cusp ones, like NFW, show a very steep behaviour in that region.

All dark matter profiles depend on at least two physical parameters, the typical scale radius r_s and the typical scale density ρ_s. The Einasto profile, described in equation 2.3, depends not only on r_s and ρ_s, but also on a free parameter α. According to observations, a fit of the dark disk of the Milky Way with an Einasto profile suggests $\alpha = 0.17$.

Other often used profiles, for example Burket (21),

$$\rho_{Burk} = \frac{\rho_s}{\left(\frac{r}{r_s}\right)\left(1+\left(\frac{r}{r_s}\right)^2\right)}, \tag{2.4}$$

and isothermal (22),

$$\rho_{iso} = \frac{\rho_s}{\left(1+\frac{r}{r_s}\right)}, \tag{2.5}$$

emerge from the Zhao parametrical function family, from which NFW is part of. They are characterized by a set of three parameters (α, β, γ), that vary to generate different shapes for the dark matter distribution:

$$\rho_{Zhao} = \frac{\rho_s}{\left(\frac{r}{r_s}\right)^{\gamma}\left[1+\left(\frac{r}{r_s}\right)^{\alpha}\right]^{\frac{\beta-\gamma}{\alpha}}}. \tag{2.6}$$

Table 1 expresses r_s and ρ_s that fit the Milky Way with NFW, Einasto, Burket and Isothermal profiles (23). The values of ρ_s are such that the dark mass in 60 kpc (a bit further from the distance of the Large Magellanic Cloud (LMC), 50 kpc) is $M_{60} = 4.7 \times 10^{11}$ $M_{\odot}$. (24) Moreover, it is also assumed that at $R_{\odot} = 8.33$ kpc (25), $\rho_{\odot}^{DM} = 0.3$ GeV/cm^3. (26) The dark matter density as a function of the distance from the disk center are shown in figure 7. The dashed lines is the local dark matter density, $\rho_{\odot}^{DM} = 0.3$ GeV/cm^3 at $R_{\odot} = 8.33$ kpc. [5].

Table 1 – Parameters α, r_s and ρ_s for the parametrisations NFW, Einasto, Isothermal and Burket. The values of α, r_s and ρ_s were taken from reference (23).

Profile	α	r_s [kpc]	ρ_s [GeV/cm^3]
NFW	-	24.42	0.184
Einasto	0.17	28.44	0.033
Isothermal	-	4.38	1.387
Burkert	-	12.67	0.712

Source: By the author

In fact, the inner dark matter density of an individual halo depends on its mass and its location around the host halo. Independent on the chosen parametrisation, the

[5] In this dissertation we use $R_{\odot} = 8.5$ kpc and $\rho_{\odot}^{DM} = 0.39 \pm 0.03$ GeV/cm^3. (27)

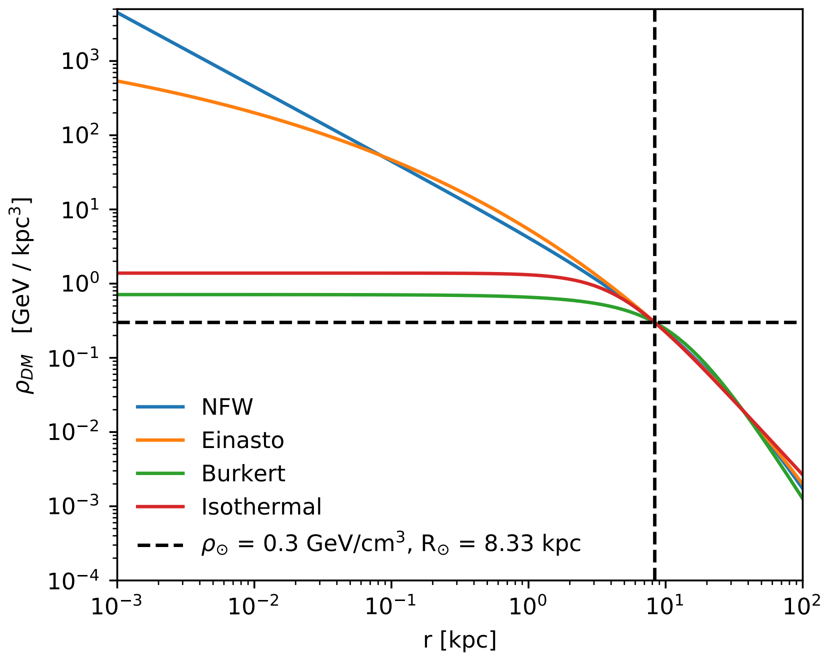

Figure 7 – The dark matter density as a function of the distance from the halo center for the NFW, Einasto Burket and isothermal parametrisations. The dashed line represents the local dark matter density, $\rho_\odot^{DM} = 0.3$ GeV/kpc^3 (26) at R$_\odot$ = 8.33 kpc. (25)

Source: By the author

physical parameters r_s and ρ_s of the sub-halo can be determined by the concentration relation (28):

$$c = c(m, r) \equiv \frac{r_{200}}{r_s}, \tag{2.7}$$

where r_{200} is the distance at which the density is larger than 200 times the critical density $\rho_{cr}(z)$. Given the mass M_{200} of a halo, r_{200} can be calculated by

$$M_{200} = \frac{4\pi}{3} r_{200}^3 200 \rho_{cr}(z). \tag{2.8}$$

The concentration parameter can be derived by the properties of the dark matter halos resolved in N-body simulations. Given the mass of the sub-halo, or its r_{200}, and the concentration parameter, the profile is completely determined.

Gravitational dynamics is very complex to be analytically analysed since linear perturbation theory covers only limited cases of structure formation. Therefore numerical methods are needed to infer how dark matter collapse and distribute around galaxies, in particular the Milky Way. Because the Universe is mostly dominated by dark matter, simulations with only this type of matter are good enough to describe the behaviour of structures. Only recently computational power increased sufficiently to approximately trace baryons in the simulations via hydro-dynamical processes. Following we describe the principles of only dark matter simulations.

2.2.1 Modern many-body simulations of dark matter halos

This section is dedicated to give an overview of the steps taken to simulate the interactions of a set of dark matter particles.

First it is important to note that simulations do not trace single dark matter particles. Because they are presumably elementary particles, therefore they have a high number density, simulations could only analyse a microscopic part of the Universe. Instead, bodies with higher mass M, usually of $10^2 - 10^6$ solar masses, are simulated.

The next step is to choose the volume of the Universe that will be simulated. Obviously, it is impossible to simulate the entire Universe, so comoving cubes of length L are simulated. It is necessary, however, that L is greater than the largest structures of the Universe so that the effect of large-scale structures is not neglected. Usually, no structures larger than $L \gtrsim 200\mathrm{h}^{-1}$ Mpc are observed, therefore that is a reasonable value of L. The number of grids N_{grid} that can be simulated inside the comoving cube depends of the computational power, i.e. the speed and memory of the computer that runs the simulation. Once N_{grid} is set, the lenght-scale of the numerical simulation is determined $\Delta x = L/ \sqrt[1/3]{N_{grid}}$. The minimum mass that can be resolved is determined by the grid length, by the dark matter particle mass and by the total number of particles being simulated.

It is also necessary to set the boundary conditions. The exterior region should not be considered empty because the particles that are close to the cube walls also feel a gravitational force from the matter located outside. To overcome this issue, simulations are periodic, which is based on the fact that the Universe is essentially homogeneous for distances greater than L. Therefore, when particles reach the bounders, they automatically re-enter the cube from the opposite side with the same velocity vector. Given that, the mass distribution and force field in the cube is periodic, with period L. The assumption of periodicity, however, affects the simulation results on scales comparable to L. Therefore, quantitative analysis of the simulations should be based on scales of the order $\backsim L/2$.

With the basic structure of the simulation settled, it is time to define the force field. The sum of forces acting in an individual particle i is represented by

$$F_i = \sum_{j \neq i} \frac{M^2 \times (\mathbf{r_j} - \mathbf{r_i})}{|\mathbf{r_j} - \mathbf{r_i}|^3}, \tag{2.9}$$

where j represents all other particles. For a simulation with 10^{10} particles, it would be necessary to calculate 10^{20} force interactions in every time step, which is not computationally doable. Instead, the force is calculated with an approximation method, except for the nearest particles. The mass of the particle j is distributed in the neighbouring grid points of the particle i. The portion of the mass of the particle j that is assigned to each grid point is determined by the particle distance to the point. Then, the force is calculated via Fast Fourier Transform (FFT).

For a better spatial resolution, the force field of the nearest particles are calculated separately. The gravitational potential $\phi(r) = -GM/r$ of a particle is split into a short and long term $\phi(r) = \phi_s(r) + \phi_l(r)$. For example, one can define the short-term potential as $\phi(r)f(r/r_s)$, with $f(r/r_s)$ being a function that declines until it reaches $r = r_s$, whence it becomes zero. On the other hand, the long-term potential is defined as $\phi(r)[1 - f(r/r_s)]$ and has the opposite behaviour. The force of particles closer than r_s are determined via the gradient of the short-term potential. As for the rest, the force corresponds to the long-term potential and is calculated via the grid method.

Finally, it is needed to set the initial conditions of the simulation. The particles are distributed in the comoving cube so that the power spectrum of the mass distributions resembles the one from the cosmological model[6].

Then the equations of motion of the particles are integrated in time. The time step can be chosen so that one can see quick variations of velocities of the particles that have close neighbours, in comparison with the particles that are relatively isolated. On the other hand, it is also possible to define different time steps for each particle, which would increase the difficulty of the simulation. The velocity and position of particles are then stored and used to produce the results.

Following we describe the properties of two set of simulations that will be analysed in this work: `AQUARIUS` and `ELVIS`.

The `AQUARIUS` (29) is a suite of 6 Milky Way sized simulations performed in periodic cubes with $L = 100h^{-1}$ Mpc, with the following cosmological parameters $\Omega_m = 0.25$, $\Omega_L = 0.75$, $\sigma_8 = 0.9$, $n_s = 1$ and $H_0 = 100$ kms^{-1}Mpc^{-1}, which are consistent within uncertainties to the WMAP 1- and 5- data analysis. The mass of the dark matter particle spans from few thousands to millions of solar masses. The main results of the `AQUARIUS` suit of simulations are

- in the largest simulation, around 300000 sub-halos were resolved in the region of the virialized host halo,
- up to four generations of sub-halos were found within the simulations,

[6] The origin of macroscopic density fluctuations from quantum perturbations can actually be studied quantitatively and the initial power spectrum of such fluctuations can be calculated. The density fluctuations can be decomposed as a Fourier series: $\delta(\mathbf{x}) = \sum a_k \, cos(\mathbf{x} \cdot \mathbf{k})$. The power spectrum $P(k)$ describes the mean of $|a_k|^2$ averaged between all vectors $\mathbf{k}$ of the same length. The larger the value of $P(k)$, the larger is the fluctuation in the distance scale given by $2\pi/k$.

- the inner dark matter profiles of sub-halos are well fit by Einasto functions but the profile parameters do not converge,

- the spatial distribution of sub-halos around the host halo is also fitted by an Einasto profile with $\alpha = 0.678$ and $r_s = 199$ kpc. The left panel of figure 8 plots the radial distribution of satellites,

- the differential sub-halo abundance per mass was proved to follow a power law with spectral index $\beta = 1.9$. This distribution is plotted in the right panel of figure 8,

- the mass fraction contained in sub-halos reaches up to $\approx 13\%$.

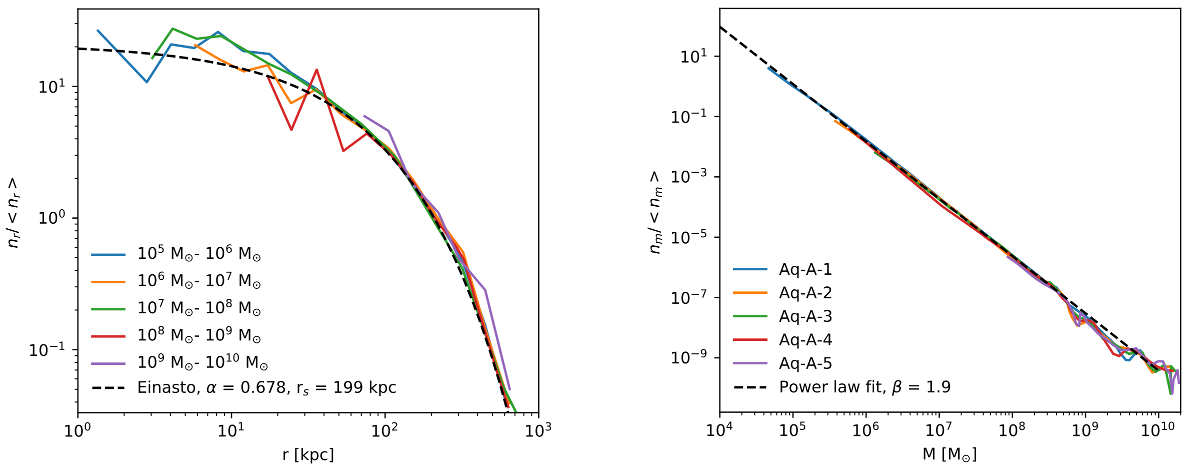

Figure 8 – Left panel: radial distribution of sub-halos resolved by the `AQUARIUS` simulations. The normalisation of the distributions separated in each mass decade converges to an Einasto function with $\alpha = 0.678$ and $r_s = 199$ kpc. Right panel: mass distribution of sub-halos resolved in each set of the `AQUARIUS` simulations. The distribution follows a power law with $\beta = 1.9$.

Source: Adapted from SPRINGEL (29)

The Exploring the Local Volume in Simulations (`ELVIS`) (30) simulates the Local Group (LG) in a suite of 48 halos, half of them mimic the paired Milky-Way and M31 halos, while the other half are simulations of isolated Milky-Way and M31 sized halos. `ELVIS` simulates a cube of 70.4 Mpc, with particle mass $M = 2.35 \times 10^4\ M_{\odot}$, and assumes the WMAP-7 cosmological parameters results: $\Omega_m = 0.266$, $\Omega_L = 0.734$, $\sigma_8 = 0.801$, $n_s = 0.963$ and $h = 0.71$. The mass distribution of the sub-halos in the `ELVIS` suite is also given by a power law, but with spectral index $\beta = 1.95$.

2.3 Dark matter properties and candidates

In this section we analyse the most important candidates for dark matter. In section 2.1, it was shown that according to the fluctuations of the CMB temperature, dark matter is most probably not, or at least not completely, composed of baryonic matter. Other properties that a dark matter candidate must follow are:

- part of it must be cold (or non-relativistic): dark matter needs to be cold so that structures grow hierarchically. If all dark matter was relativistic, it would be too fast to be captured by the gravitational potential of non-extremely massive objects, like galaxies;
- it must be neutral: since no light is emitted from dark matter, they must be neutral, i.e, not interact electromagnetically;
- weakly self-interacting: dark matter must interact weakly with itself and ordinary particles. The level of interaction is constrained by observations of cluster merges;
- it must be stable: the dark matter lifetime must be of cosmological scales, otherwise all of it would have decayed by now;
- consistent with Big Bang Nucleosynthesis (BBN): the fraction of deuterium (De) and helium (^{4}He) in the phase of the BBN determines $\Omega_b \approx 0.04$, while $\Omega_m > 0.1$, as pointed out by temperature fluctuations of CMB;
- compatible with direct and indirect detection constraints: dark matter properties should match the constraints already determined by past and running experiments that search for dark matter.

There is a wide variety of dark matter candidates that fit these requirements. In the Standard Model (SM) of particle physics [7], only one massive and stable particle is known to be neutral, the neutrino (ν). Neutrinos are good candidates for HDM, but as noted before, it could not form all of dark matter. Therefore all dark matter characteristics suggest that this particle is not part of the SM theory. Several models extend SM to include new physics. Following, we discuss the most successful one.

2.3.1 Weakly Interacting Massive Particles

The most successful beyond the Standard Model (BSM) theory predicts the existence of a neutral, weakly interacting, stable and cold particles known as Weakly Interacting

[7] The Standard Model (SM) of particle physics classifies all elementary particles and describes three of the four known fundamental forces in the Universe: weak, strong and electromagnetical (the canonical theory of gravity, the general relativity, is yet not explained in the matter of quantum field theory, which would cause it to have no impact on subatomic interactions explained by the SM). The current status of the SM states the existence of 6 flavours of quarks, 6 of leptons (this includes 3 neutrinos), 1 gluon, 2 weak bosons, the photon and the Higgs boson. Each elementary particle is associated with a respective antiparticle.

Massive Particles (WIMPs). (5) Their mass are expected to range from 100 GeV to 10 TeV.

In early Universe, WIMPs (χ) could annihilate into (be produced by) collisions with SM particles of the thermal plasma:

$$\chi\bar{\chi} \leftrightarrow SM, S\bar{M}. \tag{2.10}$$

Initially, this reaction was in thermodynamic equilibrium and its rate was given by $\Gamma_{DM} = \langle\sigma v\rangle n_{eq}$, in which $\langle\sigma v\rangle$ is the velocity averaged cross-section of the reaction and n_{eq} is the WIMP number density in thermal equilibrium. As the Universe expanded, the temperature of particles became smaller, which reduced their number density and with it, the rate of production and annihilation.

When Γ_{DM} became lower than the expansion rate of the Universe, no more WIMPs annihilated or were produced, because the mean free path for these reactions became smaller than the Hubble radius [8]. (7) After that, WIMP number density in a comoving volume remained constant. This event is known as WIMP freeze-out and is represented in figure 9, that plots the WIMP density Y as a function of the WIMP mass by the temperature of the Universe. As seen in figure 9, as the temperature drops with time, the WIMP abundance decreases exponentially until the freeze-out temperature is reached and Y gets to the equilibrium value. Then, WIMP production and annihilation are ceased and WIMP abundance in a comoving volume becomes steady.

From estimations of the present number density and relic density of WIMPs, the velocity averaged cross-section can be determined as $\langle\sigma v\rangle \approx 3 \times 10^{-26}$ cm^3/s for a generic mass of WIMP. This value is remarkably close to the cross-section of weak interactions, showing that this candidate could indeed couples weakly with SM particles. This result, known as "the WIMP miracle" launched the WIMP hypotheses as the benchmark for dark matter candidates. The thermal $\langle\sigma v\rangle$ as a function of the WIMP mass (31) is shown in figure 10.

2.3.2 Neutrinos

As discussed above, neutrinos are good candidates for hot dark matter. In SM, neutrinos were believed to be massless, however this is known to be wrong due to observations and by the theory of oscillations of neutrino flavours. The current best upper limits of the neutrino relic abundance, $\Omega_\nu < 0.003$ (1) is much smaller than the known total relic abundance of dark matter. Therefore, neutrinos are not abundant enough to make up all dark matter

[8] The Hubble radius defines the spherical volume of the observable universe that surrounds the observer. Objects beyond this radius depart from the observer with speed greater than the speed of light because of the expansion of the Universe.

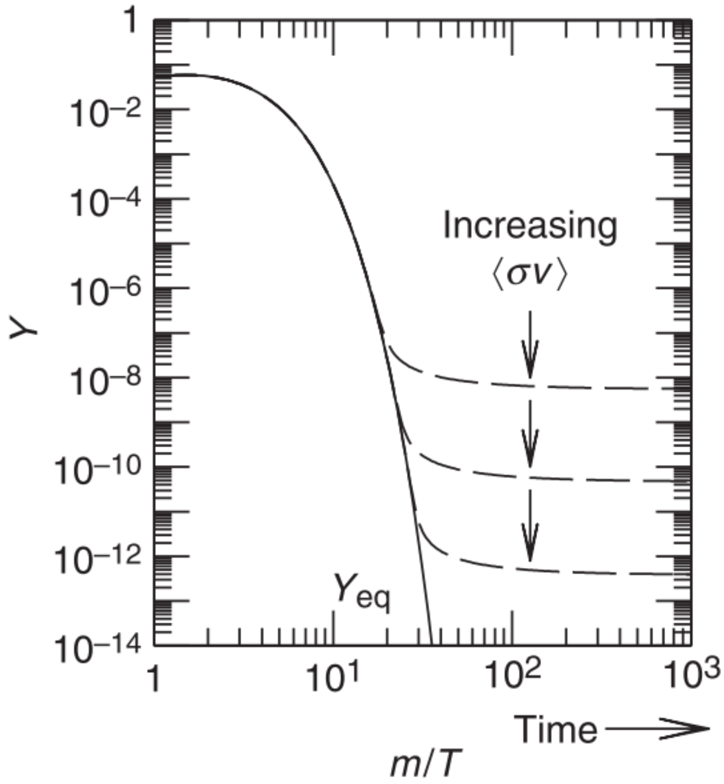

Figure 9 – WIMP density Y as a function of the WIMP mass divided by the temperature of the Universe (m/T). The solid line represents the case of thermal equilibrium. Dashed lines represent the values of Y in case of freeze-out with different values for $\langle \sigma v \rangle$.

Source: BERTONE (7)

The particle zoo of dark matter candidates can get quite long. The most diverse hypothesis are proposed to explain the mystery of dark matter. For example, some models postulate that dark matter is made of MAssive Compact Halo Objects (MACHOs) (32), which are astronomical objects composed of ordinary matter, like brown dwarfs, jupiters or black hole remnants. These bodies would not be seen because of their very low or no light emission. Attention has also been put on axions (33), which are low-mass, neutral and slow-moving particles that interact extremely weakly with SM particles. In the rest of this work, we analyse only the assumption of WIMP dark matter. The possible ways to detect this particle are discussed in the next section.

2.4 Detection of dark matter

The dark matter theory can be experimentally tested in three ways: direct detection, indirect detection and production in particle colliders. Figure 11 schematically shows these procedures, where χ is the dark matter and SM is a particle from the Standard Model. In a nutshell, the direct detection is based on the identification of the nuclear recoil after

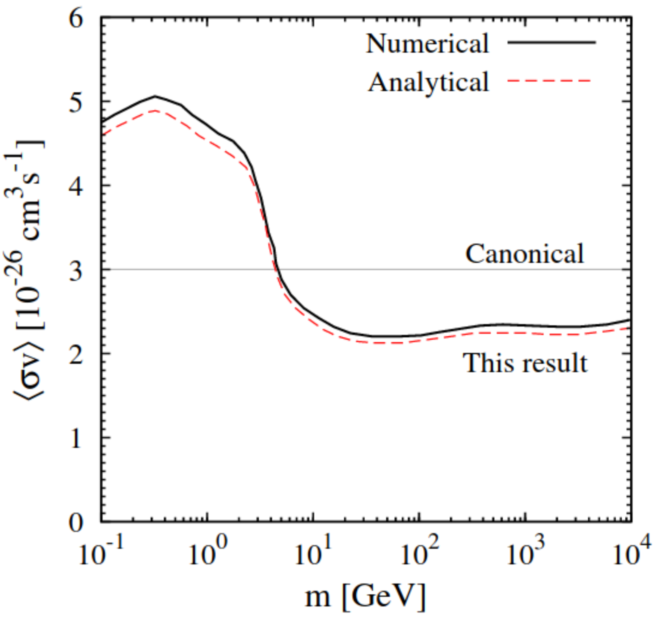

Figure 10 – Thermal $\langle\sigma v\rangle$ as a function of WIMP mass. The numerical integration of the evolution of Y as a function of m/T is represented as the solid black line, while the analytical approximation is given by the dashed red line. Reference (31) considered $\Omega_{cmb}h^2 = 0.11$, where h is the Hubble constant. The black horizontal line represents the canonical thermal value, $\langle\sigma v\rangle \approx 3 \times 10^{-26}$ cm^3/s.

Source: STEIGMAN (31)

interactions with dark matter. The indirect one relies on the detection of SM particles produced after dark matter annihilation or decay. By its turn, collider detection depends on the recognition of the missing transverse energy.

2.4.1 Direct detection

In direct detection it is expected that dark matter particles in the solar neighbourhood should interact weakly with standard model particles when passing through Earth. Direct experiments search for the scattering of atomic nuclei induced by dark matter. The dark matter particles transfer momentum to the nuclei, which gain energy. This energy can be detected by the measurement of the slight increase in the ordinary matter temperature. The scattering, however, is hard to detect because the cross-section of the interaction is very small. For a dark matter mass of 300 GeV with characteristic velocity of 200 km/s, a typical velocity in galaxies, the recoil energy is around $\approx$ 100 keV. Therefore direct experiments need to discriminate the background with extreme sensitivity. For that, they are placed underground, so the detector material is almost completely shielded from the interference of cosmic rays. Existing experiments have constrained the parameter space of dark matter, which relates the mass and the velocity averaged cross-section. The DAMA (35) experiment has even claimed a dark matter detection. However interpreting this result as a true signal is still controversial.

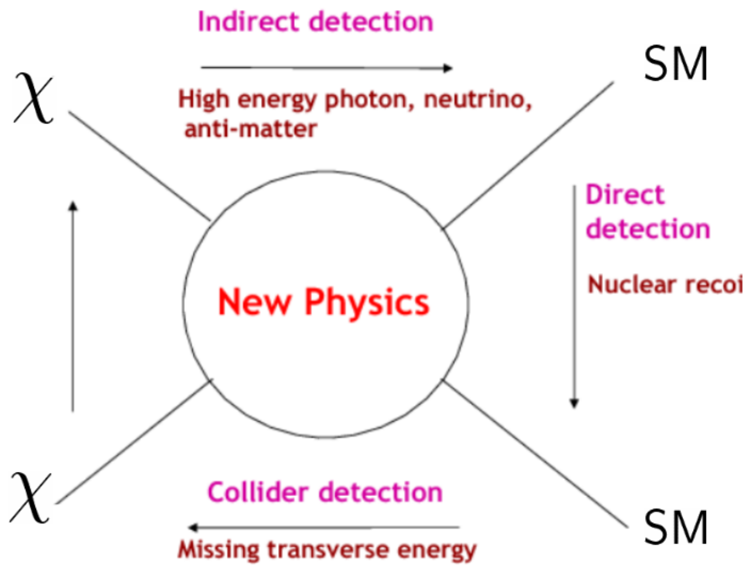

Figure 11 – Different techniques for dark matter detection. Indirect detection (right-oriented arrow) depends on the detection of SM particles produced after dark matter annihilation or decay. Direct detection (lower-oriented arrow) identifies the recoil of nuclei after interactions with dark matter. Collider detection (left-oriented arrow) is based on the measurement of the missing transverse energy of the final particles after collision. In this case, SM particles could produce dark matter in collisions.

Source: Adapted from BI (34)

2.4.2 Production in colliders

This technique, as shown by the left-oriented arrow of figure 11, relies on the production of dark matter particles by ordinary matter collisions in laboratory, such as the Large Hadron Collider (LHC). The LHC key projects are the search of the Higgs particle [9] and the search of physics beyond the Standard Model.

In colliders, the sum of momentum, energy and charge of particles before and after collisions could point to the production of dark matter. The identification of dark matter production can only be reconstructed by the missing momentum of the final products after the collision because dark matter would escape the collider due to its neutral and stable properties. Colliders provide a well known experimental environment. On the other hand, they can only probe particles whose mass lie on the energy reach of the detector.

2.4.3 Indirect detection

Dark matter and its anti-particles may annihilate, producing a flux of standard model particles, such as neutrinos, charged cosmic rays and photons. By its turn, telescopes

[9] The Higgs boson is an elementary particle from the Standard Model, produced through the quantum excitation of the Higgs field. The Higgs mechanism explains why particles have mass.

can detect SM particles on Earth. As mentioned in section 2.3.1, after freeze-out, dark matter production and annihilation have become very rare. However, in regions of high dark matter density, the annihilation rate is large enough to produce a detectable SM flux.

The type of particles generated in the chain of dark matter annihilation will determine the type of signal seen on Earth. Generally it is expected that photons with energy from a few GeV up to hundreds of TeV are the final products of annihilation. The SM particles have such energy that is twice the value of the dark matter particle. Remember that if dark matter is cold, its total energy is practically equal to its rest energy because its velocity should be reasonably low. In the case of WIMPs, photons generated in the annihilation chain lie in the gamma-ray (γ) spectrum.

Because gamma-rays can travel long distances in the Universe without being absorbed [10] and they are not charged, therefore are not deflected by interstellar magnetic fields, the observable flux has intrinsic information about the mass and annihilation cross-section of dark matter, as well as the source direction. Detecting gamma-rays directly require experiments on space so that the photons do not interact with the Earth's atmosphere, producing an electromagnetic cascade. The FERMI Large Area Space Telescope (FERMI-LAT) (37) is a such gamma-ray observatory orbiting Earth since 2008. It covers the energy range from about 20 MeV to above 300 GeV. Nevertheless, efforts have been made so that gamma-rays can be indirectly observed by ground based telescopes, such as the Major Atmospheric Gamma Imaging Cherenkov Telescopes (MAGIC) (38), the High Energy Stereoscopic System (H.E.S.S.) (39) and the forthcoming Cherenkov Telescope Array (CTA). (40)

Electron and positron (e^+) pairs are produced by the electromagnetic cascades induced by photons when they pass through the atmosphere. Ground-based experiments can observe the cascade as the e^+e^- pairs emit Cherenkov light when they interact with the atmosphere. Cosmic rays, however, are responsible for most of the observed Cherenkov light. Therefore, rejecting the cosmic-ray background is of critical importance.

Numerical simulations of atmospheric cascades, such as CORSIKA (41) and AIRES (42), are used to differentiate photons and cosmic ray showers. However, this task is not so simple as simulations depend on the uncertainties of the density and magnetic fields of the atmosphere. Figure 12 shows the different distributions expected for a cascade induced by a muon (μ), a gamma-ray and a hadron. The blue array represents the spatial distribution of particles detected by the telescopes, while the collor bar represents the energy of the events.

The search for neutrinos produced by dark matter annihilation is also favoured by

[10] The observed flux of gamma-rays can be suppressed by the pair production process ($\gamma \to e^-e^+$). The mean free path of this mechanism is of the order 0.01-1000 Mpc, for a photon energy spanning from 100 GeV to 1000 TeV. (36)

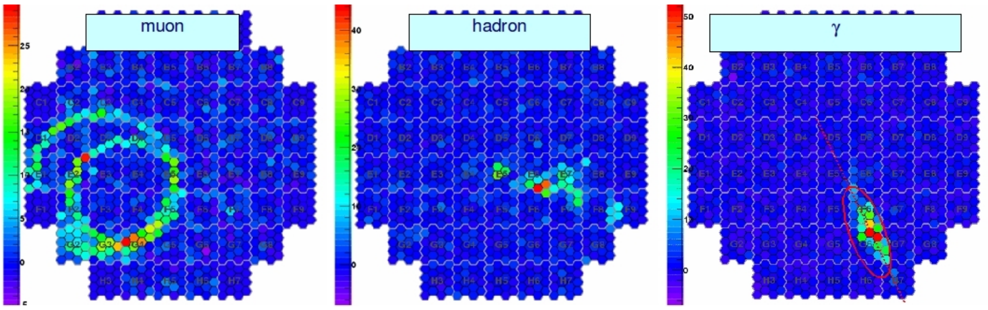

Figure 12 – Different shapes of cascades induced by particles interacting with the atmosphere. The blue array represents the spatial distribution of particle hits identified by the experiment and the color bar is the energy intensity of the hit. Left panel: shape of cascade induced by a muon. Middle panel: cascade induced by a hadron. Right panel: cascade induced by a gamma-ray.

Source: DE ANGELIS; PIMENTA (43)

their neutral charge. Here, WIMPs that cross the Earth suffer scattering from nuclei, which changes the dark matter velocity, that may be lower than the escape velocity of the planet. WIMPs are, then, gravitationally bound and reach the center of the Earth, which becomes a region of high dark matter density and accordingly, the rate of annihilation is enhanced. Except for neutrinos, the Earth structure will stop all annihilation products. The spectrum of specific neutrinos coming from the center of the Earth could be a distinctive signature of dark matter because the neutrinos produced in the annihilation process have higher energy than the ones generated in nuclear reactions. An experiment that could probe dark matter in this way is the IceCube (44), in Antarctica.

Indirect searches of dark matter regarding cosmic rays are based on the detection of the antimatter components of the annihilation, mainly antiprotons, positrons and anti-nuclei, like anti-deuterium and anti-helium. The antimatter flux, however, is observed and expected to be much smaller than the correspondent particle flux, i.e., protons and electrons. Because antiparticles were believed to be only secondary ones, i.e., produced strictly during the propagation of primary particles through the Universe, a source of primary antiparticles, like dark matter, influences the shape of the anti-flux. The Alpha Magnetic Spectrometer (AMS-02) (45) and the Payload for Antimatter Matter Exploration and Light-nuclei Astrophysics (PAMELA) (46) are examples of cosmic ray experiments.

A summary of dark matter annihilation signatures and correspondent experiments, advantages and challenges can be seen in table 2.

Figure 13 shows a summary of the $\langle \sigma v \rangle$ constraints as a function of WIMP mass from indirect searches of different experiments, assuming annihilation of dark matter into bottom quarks ($b\bar{b}$) and following decay into gamma-rays, neutrinos and cosmic rays.

Table 2 – The signal of dark matter annihilation, correspondent experiments that probe the specific particle via indirect detection and advantages and challenges for that signal. Experiments highlighted in blue are still in the planning or construction phase.

Particle	Experiments	Advantages	Challenges
Gamma-ray[†] photons	Fermi LAT, GAMMA-400, H.E.S.S.(-II), MAGIC, VERITAS, HAWC, CTA	point back to sources, spectral signatures	backgrounds, attenuation
Neutrinos	IceCube/DeepCore/PINGU, ANTARES/KM3NET, BAIKAL-GVD, Super-Kamiokande/Hyper-Kamiokande	point back to sources, spectral signatures	backgrounds, low statistics
Cosmic rays	PAMELA, AMS-02, ATIC, IACTs, Fermi LAT, Auger, CTA, GAPS	spectral signatures, low backgrounds for antimatter searches	diffusion, do not point back to sources

Source: GASKINS (6)

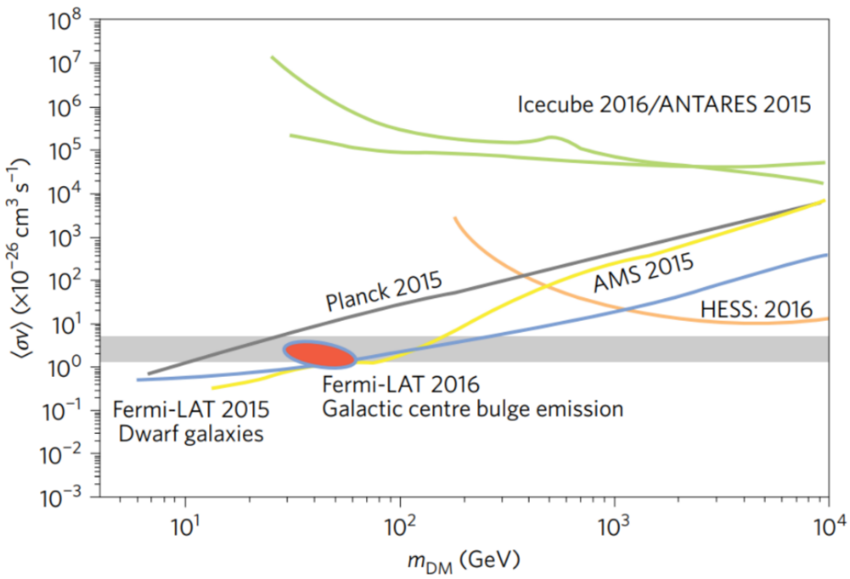

Figure 13 – The constraints on the parameter phase space of WIMP dark matter determined via indirect detection by different experiments. Curves are calculated for final products of dark matter annihilation that include photons, cosmic rays and neutrinos. The gray band represents the thermal velocity averaged croos-section for a WIMP mass ranging from 100 GeV to 100 TeV.

Source: CONRAD (47)

3 OBSERVING GAMMA-RAYS FROM DARK MATTER ANNIHILATION

3.1 The gamma-ray flux

Gamma-rays travel through the Universe without being deviated by magnetic fields because of their neutral charge. When travelling from distances relatively close, they suffer no energy loss. Therefore, gamma-rays that reach the Earth carry intrinsic characteristics of the source emitter. The differential photon flux that reaches the observer is defined as the number of photons hitting a unit area, per unit time and per unit energy. This quantity is proportional to the velocity averaged annihilation cross-section $\langle \sigma v \rangle$, to the integral in the solid angle $\Delta\Omega$ and line of sight (l.o.s.) of the dark matter density squared by the source distance from the observer squared ρ_{DM}^2/d^2 and to the energy spectrum of the gamma-rays produced via dark matter annihilation dN_f/dE in the channel f, weighted by the specific branching ratio B_f. It is also inversely proportional to the square of the dark matter mass m_χ. The complete equation of the differential gamma-ray flux is

$$\frac{d\phi_\gamma}{dE} = \frac{\langle \sigma v \rangle}{4\pi m_\chi^2} \frac{dN_f}{dE} B_f \times \int_{\Delta\Omega} \int_{l.o.s.} \left(\frac{\rho_{DM}(l, \Omega)}{d} \right)^2 d\Omega dl. \tag{3.1}$$

Conveniently, the flux is separated between an astrophysical (AP) and a particle physics (PP) term. The first one is given by

$$J_f = \int_{\Delta\Omega} \int_{l.o.s.} \left(\frac{\rho_{DM}(l, \Omega)}{d} \right)^2 d\Omega dl, \tag{3.2}$$

and is known as J-factor. This quantity reflects the dark matter distribution in the target of observation. As discussed in 2.2, dark matter distributions are parametrised as a function of the radial distance from the center of the astrophysical object.

The a particle physics (PP) term comprises all information of the dark matter model. It is given by

$$\frac{d\phi_{PP}}{dE} = \frac{\langle \sigma v \rangle}{4\pi m_\chi^2} \frac{dN_f}{dE} B_f. \tag{3.3}$$

Dark matter can annihilate directly into a pair of photons. However, the probability of this process occurring is very low. Therefore, it is interesting to study different annihilation channels that later decay into a continuous flux of photons. The left panel of figure 14 shows the spectrum of the final gamma-rays yield by dark matter annihilation weighted by the gamma-ray energy into the channels given by bottom (b), up (u) and down (d) quarks, tau leptons (τ), and W and Z bosons for $m_\chi = 1000$ GeV, assuming

100 % branching ratio in all signals. The right panel of figure 14 brings the spectrum of the final gamma-rays produced by dark matter annihilation weighted by the gamma-ray energy into the same channels, with $B_f = 100\%$, for m_χ spanning from 10 GeV to 100 TeV.

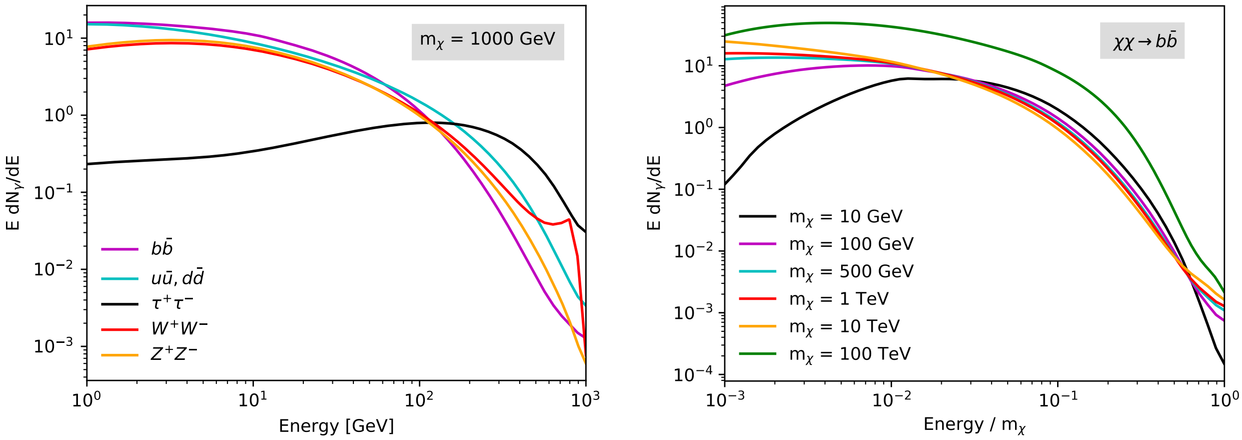

Figure 14 – Left panel: the spectra of dark matter annihilation into $b\bar{b}$ (magenta), $u\bar{u}$ and $d\bar{d}$ (cyan), $\tau^+\tau^-$ (black), W^+W^- (red) and Z^+Z^- (orange) for $m_\chi = 1000$ GeV. Right panel: the spectra of dark matter annihilation into $b\bar{b}$ ($B_f = 100\%$) for $m_\chi = 10$ GeV (black), $m_\chi = 100$ GeV (magenta), $m_\chi = 500$ GeV (cyan), $m_\chi = 1$ TeV (red), $m_\chi = 10$ TeV (orange), $m_\chi = 100$ TeV (green). For all channels it was assumed 100% branching ratio. The spectra were generated with the function *astro.darkmatter* from the GAMMAPY package. (48) Values are based on results from reference (23).

Source: By the author

The final gamma-ray flux is a consequence of the decay of τ, Z and W particles, and hadronization of quarks[1].

The hadronic final state is characterised, first, by the decay of heavy quarks into lighter ones ($t \rightarrow b \rightarrow c \rightarrow s \rightarrow u/d$). Following, a hadron shower is generated, ending with the production of pions (π). The gamma-rays are produced by the decay of the neutral pion, as will be shown below, while the charged pions produce electrons, positrons and neutrinos.

The decay of τ is known to be distributed as (49)

[1] Quarks do not exist as single particles. When they combine, they create hadrons.

$$\tau^- \to \pi^0\pi^-\nu_\tau \;\; 25.5\%$$
$$\tau^- \to e^-\nu_\tau\bar{\nu_e} \;\; 17.8\%$$
$$\tau^- \to \mu^-\nu_\tau\bar{\nu_\mu} \;\; 17.4\%$$
$$\tau^- \to \pi^-\nu_\tau \;\; 10.8\%$$
$$\tau^- \to \pi^-2\pi^0\nu_\tau \;\; 9.3\%$$
$$\tau^- \to 2\pi^-\pi^+\nu_\tau \;\; 9.0\%$$
$$\tau^- \to 2\pi^-\pi^+\pi^0\nu_\tau \;\; 2.7\%$$
$$\tau^- \to 3\pi^0\pi^-\nu_\tau \;\; 1.0\%.$$

The first channel, which has the highest probability, contains the π^0 particle as a decay product. It is known that π^0 decays as

$$\pi^0 \to 2\gamma \;\; 98.8\%$$
$$\pi^0 \to e^+e^-\gamma \;\; 1.2\%.$$

From figure 14, it is possible to see that the dark matter annihilation spectra have similar shapes, except for the $\tau^+\tau^-$ channel. Therefore the work is proceeded by analysing the τ and b channels.

3.2 Astrophysical targets for dark matter indirect detection

Indirect searches of dark matter are based on different astrophysical targets, with their own inherit advantages and challenges. The Milky Way center is believed to contain the strongest gamma-ray signal originated from dark matter annihilation. Nevertheless, rejecting the background for this target is challenged by the presence of many astrophysical sources of gamma-rays [2] and the uncertainty on the dark matter content and distribution in this area. On the other hand, nearby dwarf galaxies and dark clumps [3] provide easier separation of signal and background due to the low (or no) presence of astrophysical gamma-rays. The signal, however, is comparatively lower because of their high distance from Earth and lower amount of dark matter. Following, we discuss advantages and challenges of each target.

3.2.1 Galactic center

Because the annihilation rate of dark matter is proportional to the dark matter density squared, galactic halos make up a good target for indirect searches. Since galactic

[2] Some astrophysical sources of gamma-rays are supernova remnants, pulsar wind nebulae and gas acting as target material for cosmic rays.

[3] Dark clumps are dark matter dominated objects, only visible by observing gamma- and cosmic rays originated from dark matter annihilation, i.e., they have no star or gas content.

halos are embedded in a dark matter sphere, galaxies are indeed good targets for dark matter indirect detection, the closest being our own Milky Way. Density profiles of dark matter distribution in galactic disks show that the center is the region where one should expect the most intense flux of gamma-rays from dark matter annihilation. Because of its proximity to Earth, the Milky Way center is one the most promising targets of observation. To reduce the astrophysical background, current observations exclude a central region with galactic latitude $b < 0.3°$. Nevertheless, the background in the remaining region is still complex enough to require a deep study of the spectrum and distribution of Very High Energy (VHE) astrophysical sources, besides an accurate understanding of instrumental and observational systematics. Figure 15 shows the constraints on the dark matter parameter space from observations of the galactic center made by H.E.S.S. and FERMI-LAT.

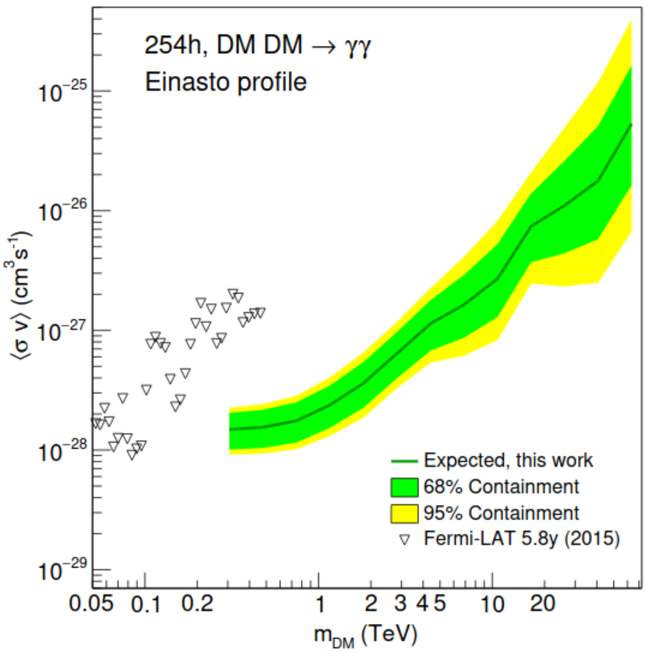

Figure 15 – Constraints on the $\langle \sigma v \rangle$ for $\chi\chi \to \gamma\gamma$ per dark matter mass provided by 254 h of observation made by the H.E.S.S. telescope (solid green line) together with the values for 68 % (green area) and 95 % C. L. (yellow area) containment with respect to the mean. Triangles represent values constrained by FERMI-LAT up to 2015.

Source: RINCHIUSO (50)

3.2.2 Dwarf spheroidal galaxies

The Dwarf spheroidal galaxies (dSphs) of the Local Group are also suitable targets for dark matter indirect detection. They are small galaxies with low luminosity due to their very old stellar population. The best advantage of dSphs is their content of dark matter, that is believed to be around 1000 times higher than the amount of ordinary matter. Moreover, dwarf spheroidal galaxies have very low astrophysical background. On the other hand, they are much more distant comparatively to the galactic center, therefore the dark matter signal is fainter.

Good dwarf galaxies for dark matter studies are selected by analysing their J-factors and respective uncertainties. The more information of the start content of dSphs, the lower is the uncertainty on the J-factor. Therefore, classical dwarf spheroidals [4], like Sculptor, Fornax, Ursa Minor and Draco are currently the best dSPhs targets, comparatively to ultra- and hyper-faint dwarfs[5], whose star content is not so bright. On the other hand, ultra- and hyper-faint dwarfs may have higher J-factors than classical ones, which could outweigh the higher uncertainty of these objects.

A calculation of the J-factor of 8 classical and 13 ultra-faint dSPhs, via spherical Jeans analysis (53) for dark matter annihilation showed that the most promising dSphs target is Ursa Major II, with $\log_{10}[\mathrm{J}(0.5°)/\ \mathrm{GeV}^2\mathrm{cm}^{-5}] = 20.0^{+0.7}_{-0.5}$, in the north hemisphere. (54) An analysis made in (55) using the same method showed that for the Triangulum II, $\log_{10}[\mathrm{J}(0.15°)/\mathrm{GeV}^2\mathrm{cm}^{-5}] = 20.77^{+0.6}_{-0.41}$.

The number of known Milky-Way satellites up to the SDSS Data Release (DR) 9 (9) stands at 56: 34 discovered by the SDSS (9) and DES (56) (57) surveys, 11 classical dSphs and 11 discovered by different surveys. N-body simulations of the Milky Way, such as `AQUARIUS` (29) and `ELVIS` (30), however, expect this number to be thousands of times higher. Moreover, statistical estimations of the real number of satellites based on these simulations (51, 58) show that the true number could actually be 3 to 5 times higher. New ultra-faint satellites are expected to be discovered in the next years by more sensitive telescopes, such as the Vera Rubin Observatory, expected to start operations in 2023 at Cerro Pachón, Chile. (59)

3.2.3 Estimations of the total population of dwarf galaxies

Observation of photon signals originated in dwarf galaxies orbiting the Milky Way constraints the nature of dark matter. Simulations, however, indicate thousands of satellites, while only a partial census of the true number is known due to the sky coverage and flux limits of current satellites. Recent models try to combine the results of simulations and the status of the known satellites to provide more realistic prospects of the true number of satellites.

---

4 Classical dwarf spheroidals are the ones detected before the SDSS and DES sky surveys. Their star content was bright enough to be detected by not so sensitive telescopes.

5 The lower end of the galaxy luminosity function can contain objects with luminosity as low as $L < 10^5\ \mathrm{L}_{\odot}$. These galaxies are the oldest, most dark matter dominated and least metal-abundant systems known. There is no consensus on the classification of dwarf galaxies regarding its luminosity. However, references (51, 52) categorise ultra- and hyper-faint dwarf galaxies according to the absolute magnitude, in the range -8 $< M_V \leq$ -3 and -3 $< M_V \leq 0$, respectively.

Following we summarise the results of the total number of satellites by Newton *et al.* (51), Hargis *et al.* (58) and Koposov *et al.* (58).

Newton *et al.* (this study will be referred as N18 to the end of this dissertation) infer the total number of Milky Way satellites using two key ingredients: a prior to the radial distribution of sub-halos and a Bayesian inference method. The radial number density of the true population of satellites was assumed to be the one obtained in the `AQUARIUS` set of simulations and selected by v_{peak}, the maximum circular velocity achieved in the history of the sub-halo. Imposing a minimum v_{peak} provides a stronger correlation with the probability of the sub-halo hosting a galaxy. (60) The last ingredient necessary in the study was a sample of observed satellites, taken from data releases of SDSS and DES surveys. Together, DES and SDSS observations cover nearly half of the sky.

The Bayesian inference method aims at calculating the Probability Density Function (PDF) of the total number of sub-halos with magnitude below a certain value $N_{tot}(< M_v)$ given that a survey has detected $N_{obs}(< M_v)$ satellites in the effective survey volume $V_{eff}(M_v)$. (61,62) The PDF in the Bayesian methodology is

$$P(N_{tot}(< M_v)|N_{obs}(< M_v), V_{eff}) = \frac{P(N_{obs}(< M_v)|N_{tot}(< M_v), V_{eff})P(N_{tot})}{P(N_{obs}(< M_v), V_{eff})}, \tag{3.4}$$

in which $P(N_{obs}(< M_v)|N_{tot}(< M_v), V_{eff}$ is the probability that a survey will observe $N_{obs}(< M_v)$ in the effective survey volume $V_{eff}(M_v)$ given a total number of sub-halos, $N_{tot}(< M_v)$. The probability of $P(N_{tot})$ is assumed to be flat distribution, while the denominator is a normalisation factor.

The likelihood is computationally calculated via a Monte Carlo method applied to 5 MW analogues simulated by `AQUARIUS`. The method consists of

1. selecting the tracer population of sub-halos within 300 kpc of the Milky Way center. This population consists of sub-halos resolved by `AQUARIUS`;

2. randomly ordering the tracer population into an indexed list;

3. placing the survey at 8 kpc from the MW center, in one of the vertices of an octahedron;

4. generating the conical effective survey volume $V_{eff}(M_v)$ for an observed satellite with magnitude M_v, starting from the brightest one. The apex of the region is located at the observer;

5. generating a random number N_{rand} until $N_{obs}(< M_v)$ sub-halos with magnitude M_v are located inside $V_{eff}(M_v)$. That sets the lower bound of $N_{tot}(< M_v)$;

6. to set the upper limit of $N_{tot}(< M_v)$, the list is checked down until it is found the largest sub-halo index such that there is still $N_{obs}(< M_v)$ satellites inside $V_{eff}(M_v)$;
7. a random number between the lower and upper bound is generated and this amount of sub-halos are removed from the beginning of the list;
8. the procedure is repeated for the next brightest sub-halo.

Such steps, however, represent only one possible realisation of $N_{tot}(< M_v)$. To account for other variations, it is considered 6 positions of the survey at 8 kpc from the host center, 5 different MW analogues resolved by `AQUARIUS`, new randomisation of the tracer population, and 1000 pointings of the survey, evenly distributed in the sky. In total, 3×10^4 realisations were produced.

N18 find that there should be at least 124^{+40}_{-27} (68 % C. L.) satellites within 300 kpc from the Sun and with absolute magnitude brighter than $M_V = 0$. The final radial distribution of Milky Way satellites converge to an Einasto profile, with $\alpha = 0.24$ and $r_s =$ 43.0 kpc. Because simulations show that the radial and mass distributions are reasonably independent [6], the mass distribution of the total number of satellites follows the same power-law observed for the `AQUARIUS` sub-halos.

The left panel of figure 16 contains the radial distribution of observed satellites and sub-halos selected from `AQUARIUS`, while the right one shows the results of the expected luminosity function, i.e., the number of sub-halos as a function of M_v. In the left panel it is shown that the sub-halos selected from `AQUARIUS` and the observed ones follow reasonably the same radial distribution. In the right panel, the magenta line represents the luminosity function when taking into account all satellites observed by DES and SDSS, while the green and blue lines take into account only the satellites observed from a single experiment, DES and SDSS, respectively. The black line describes the known luminosity function of already detected satellites.

Hargis *et al.* (this study will be referred as H14 to the end of this dissertation) predicted the spatial placement and total number of Milky Way satellites by completeness correcting the observed stellites by SDSS up to the DR8. (63) The completeness correction strategy requires a statistical description of the spatial distribution of MW satellites. For this purpose, H14 adopts the radial density of sub-halos given by the `ELVIS` simulations. Three toy models were analysed to determine whether the dark sub-halos resolved in `ELVIS` could host dwarf galaxies:

- *Massive in the past (v_{peak} > 12 km/s)*: Sub-halos massive in the past have deeper potential wells that are likely to capture and cool the gas necessary for star formation.

[6] Such assumption is not valid for sub-halos near the galactic center, where small substructures suffer effects of tidal disruption.

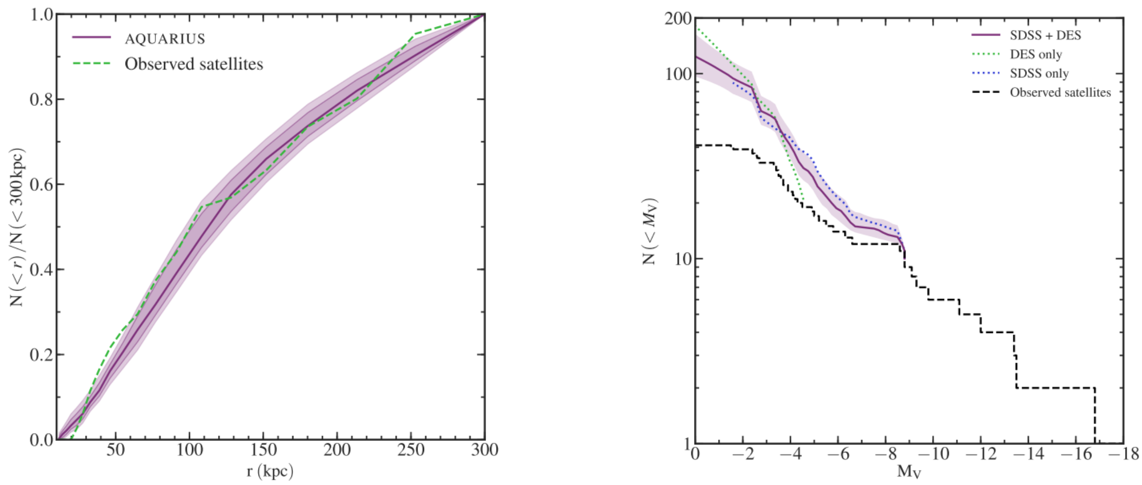

Figure 16 – Left panel: the radial distribution of observed satellites and sub-halos selected from AQUARIUS. Right panel: the luminosity function for satellites expected by the study from N18.

Source: NEWTON (51)

The depth of potential well depends on the value of v_{peak}, i.e the maximum circular velocity achieved by the sub-halo history;

- *formed before reionization ($z > 8$)*: based on photometric and spectroscopic studies of ultra-faint dwarfs, sub-halos could have their start component formed before the reionization era (64–66);

- *earliest infall ($z_{peak} \geq 3$, i.e $t_{infall} \geqslant 11.5$ Gyr)*: early infall of dwarfs into the Milky Way results in lost of gas. (67) Many Milky Way dwarfs show signs of tidal disturbance, which is expected for satellites orbiting its host for the longest time and with the lowest orbital pericenter. (68–70) Because v_{peak} is reached just before the fall of sub-halos into the host potential well, the value of z_{peak} can be used to determine the time of infall.

For all models, sub-halos with $v_{peak} > 25$ km/s were excluded, because their potential well suffices to host the most luminous star components, known as classical dwarfs. That corresponds to a sub-halo peak mass of $M_{peak} = 2.14 \times 10^9\ M_\odot$, calculated by the $v_{peak} - M_{peak}$ relation provided in figure 1 of (30).

The strategy adopted by H14 consists of:

1. generating a randomly placed SDDS effective survey volume for each satellite with a given M_v observed up to the SDSS DR8;

2. computing the fraction of sub-halos $N(< r)$ inside V_{eff} for each toy model;

3. calculating N_{tot} inside V_{eff}, given by $1/(N(<r))$.

To account for variations, 100 mock-SDSS footprints with random pointings were simulated for each observed satellite. Using the strategy described above, H14 predicts a total of 168-896 (90 % C. L.) satellites within 300 kpc.

Figure 17 shows a comparison of the predicted cumulative fraction of total sub-halos for each toy model with Einasto, NFW and Isothermal profiles. The early infall model is best represented by the NFW profile, while the massive in the past and formed before reionization are best characterized by isothermal. An isothermal profile with $r_s = 37.49$ kpc can also describe the total number of sub-halos. Again, as the mass and radial distributions are reasonably independent, it is assumed that the mass distribution of this population of sub-halos follows a power-law with $\beta = 1.95$.

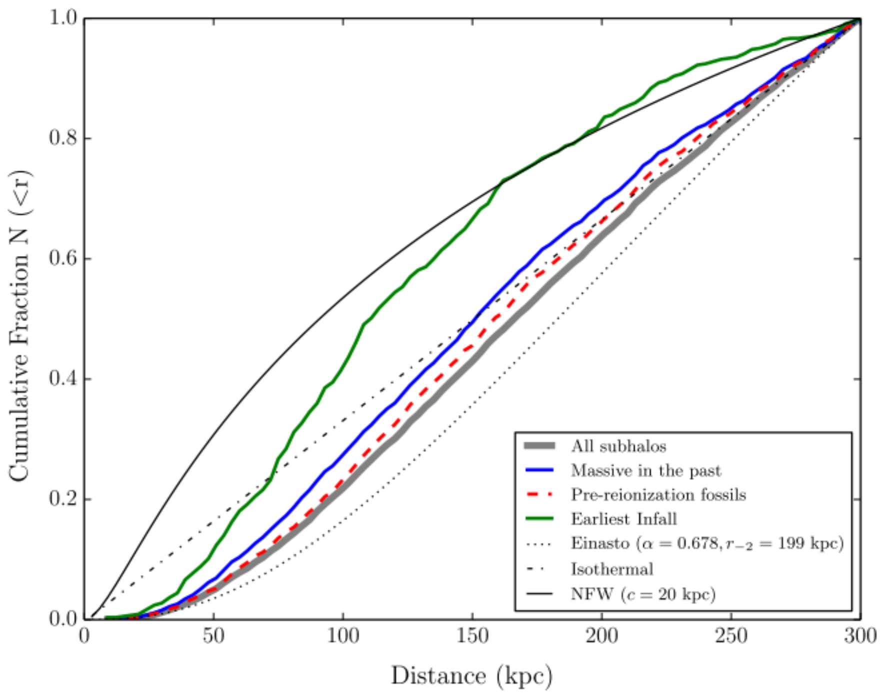

Figure 17 – The cumulative fraction of sub-halos according to the distance from the galactic center for the models: massive in the past (blue-solid), pre-reionization (red-dashed) and earliest infall (green-solid) and sum of all models (grey-solid) from the study of Hargis and comparisons with a NFW (black-solid), isothermal (dash-dotted) and Einasto (dotted) parametrisation (with parameters equal to the radial distribution of substructures in the AQUARIUS simulations).

Source: HARGIS (58)

The last estimation of the total population of satellites we analyse is from Koposov *et al.* (71) (this study will be referred as K8 to the end of this dissertation). K8 also adopts the completeness correction method. However, it assumes that sub-halos should follow the same spatial distribution of the dark halo of the Milky Way, described by an NFW profile with $r_s = 10$ kpc. Moreover, the list of known observed satellites used in the study contains only satellites discovered by the SDSS DR5. (72) K8 finds that the differential cumulative number of sub-halos as a function of the absolute magnitude is

$$\frac{dN}{dM_V} = 10 \times 10^{0.1(M_V+5)}. \tag{3.5}$$

Using equation 3.5, the total number of dwarf satellites between -20 $< M_v <$ 0 is 136.

4 THE CHERENKOV TELESCOPE ARRAY

4.1 Imaging Air Cherenkov Telescopes

Results in VHE astrophysics are mostly due to Imaging Atmospheric Cherenkov Telescopes (IACTs), that detect Cherenkov light emitted by charged particles in atmospheric showers when they pass through detector material.

The first significant signal by an IACT experiment was the detection of the Crab Nebula flux, seen by WHIPPLE in Arizona, 1989. (43) The Cherenkov technology improved with second generation instruments, such as HEGRA (73) and CANGAROO. (74) Currently, instruments of third generation that can detect photons up to few TeV, such as H.E.S.S. (39) in Namibia, VERITAS (75) in Arizona and MAGIC (38) in the Canary Islands are detecting photons from thousands of sources every year with high sensitivity. Due to atmospheric and weather conditions, such telescopes usually operate only around 1000-1500 hours per year.

When high-energy gamma-rays interact with the atmosphere, a shower of secondary particles is produced, as exemplified in figure 18. Cherenkov emission, as represented in figure 19, is characterised by a cone of angle θ that relates to the atmosphere and velocity of particles as $\cos\theta = (\beta n)^{-1}$, in which β is the particle's velocity in units of c[1] and n is the refraction index of the atmosphere. The maximum number of particles in the shower is reached at around 10 km from the point where the shower started. The shower can reach a ground area of about 250 m in diameter, referred to as the Cherenkov light pool. When these secondary particles move in the atmosphere with velocity higher than light in that medium, they emit Cherenkov light.

The particle shower happens due to the pair production and bremmsstrahlung processes. For an energy higher than around 1.052 MeV, photons convert into a pair e^+e^- in the vicinity of the nuclei in the atmosphere, this is known as pair production. On the other hand, the electrons and positrons emit radiation when their trajectories are shifted due to the Columb field of the atoms. As the photons produced from bremsstrahlung have a high energy, they undergo pair production, developing the shower. When the particles reach the threshold energy, pair production and bremstrahlung ceases, and ionization is the main form of energy loss. For a primary gamma-ray of 1 TeV, around 100 Cherenkov photons/m^2 are detected by the telescope mirror on the ground a few microseconds after the shower initiated.

Following, the Cherenkov light is transmitted to a focal camera of typical diameter of 1 m, that basically consists of photomultipliers (PMTs). H.E.S.S., for example, contains

[1] The velocity of light, $c \approx 300000$ km/s.

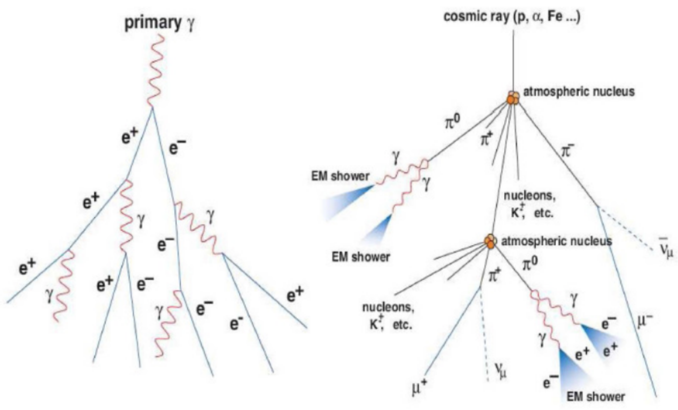

Figure 18 – The air shower produced by a gamma-ray (left) and a cosmic ray (right) when they interact with the atmosphere.

Source: ORAMAS (76)

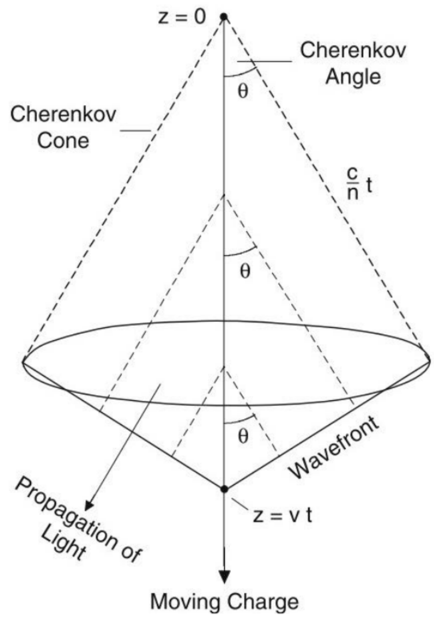

Figure 19 – The cone of Cherenkov light emitted by particles passing through the atmosphere. The z axis denotes the propagation direction of the particle, θ denotes the Cherenkov angle.

Source: GRIEDER (77)

960 PMTs in each camera, with field of view (FoV) of about $5° \times 5°$. The read-out electronics of the telescope is triggered when a number of PMTs detect a signal that exceeds a threshold in a time window. For the H.E.S.S. telescope, it is of about ≈ 1.3 ns. The signal that reached the PMTs are analogically stored while waiting for the trigger check. Following, the signal is digitized and sent from the camera data acquisition system to the control room.

The shower image produced by the signals collected in the array of telescopes contain information about the true incident direction of the shower, true energy and true time interval after the event is treated with the telescope Instrument Response Function (IRF). Treating the image to extract the true properties of the incoming gamma-ray requires background rejection, i.e, discriminating the showers produced by cosmic rays. Showers produced by cosmic rays suffer different physical processes, which results in the presence of mesons and hadrons, while the showers produced by photons contain mainly photons and e^+e^- pairs. This difference leads to different topological and energetic configurations in the images collected by the telescope, as exemplified in figure 12. The aspect of the showers makes it possible to differentiate the type of cascade. The process of collection of the Cherenkov light by telescopes is described in figure 20.

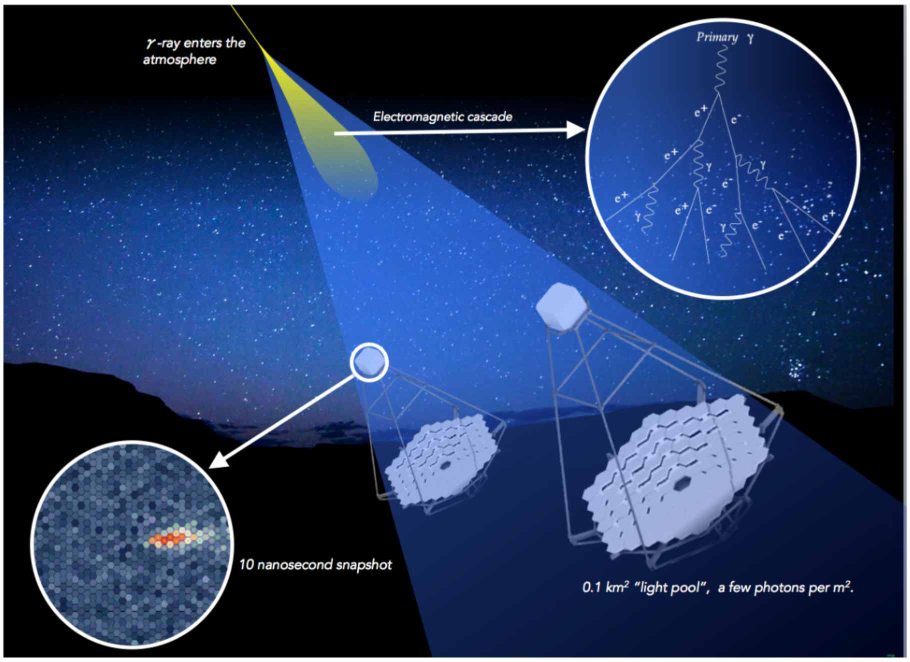

Figure 20 – The observation of Cherenkov light with a IACT telescope. When gamma-rays interact with the atmosphere, a cascade of new particles is produced. Some of these particles can emit Cherenkov light if their valocity is greater than the one from the light in that medium. The emission of Cherenkov light happens in the form of a light pool, that will reach the detectors on Earth.

Source: THE CTA COLLABORATION (10)

The Instrument Response Function (IRF) provides a mathematical function that relates the reconstructed photon arrival direction **p'**, energy E' and trigger time t' to the true arrival direction **p**, energy E and trigger time t of a photon. Equation 4.1 describes the link between the true and reconstructed quantities.

$$e(\mathbf{p}', E', t') = \int d\mathbf{p}\; dE\; dt\; R(\mathbf{p}', E', t'|\mathbf{p}, E, t) \times I(\mathbf{p}, E, t). \tag{4.1}$$

$I(\mathbf{p}, E, t)$ is the gamma-ray flux arriving at Earth as a function of the true quantities. $e(\mathbf{p}, E', t')$ is the expected event rate as a function of the reconstructed quantities. $R(\mathbf{p}', E', t'|\mathbf{p}, E, t)$ is the IRF. The IRFs also predict the background rate as function of position in the field of view and measured energy. The IRF can be written as follows:

$$R(\mathbf{p}', E', t'|p, E, t) = A_{eff}(\mathbf{p}, E, t) \times PSF(\mathbf{p}'|\mathbf{p}, E, t) \times E_{disp}(E'|\mathbf{p}, E, t), \tag{4.2}$$

where A_{eff} is the effective area of the observatory, PSF is the instrument Point Spread Function, which provides the offset angle between the true and measured arrival directions of a photon and E_{disp} is the instrument energy dispersion, which relates to the energy resolution of the instrument.

4.1.1 The current status of IACT telescopes

Arrays with more than one telescope will provide better background rejection and angular and energy resolutions. H.E.S.S., in the south hemisphere, MAGIC and VERITAS, both in the north hemisphere, are the three largest IACTs currently operating.

The H.E.S.S. observatory contains four telescopes of 12 m of diameter that are in operation since 2003. In 2012 another telescope with surface area of about 600 m^2 was included in the array.

The MAGIC observatory in the Canary Islands operates since 2004 and contains 2 telescopes, each with 17 m in diameter.

It is foreseen that new satellites already approved will significantly improve the sensitivity the of photon detection in the range of keV to PeV. Below we list future instruments and the expected improvements

- The ATHENA (78) experiment, expected for 2028, will improve the sensitivity in the keV region by two orders of magnitude;

- It is expected that e-ASTROGAM (79) and AMEGO (80) will also improve the MeV by two orders of magnitude in 2028 and 2029, respectively;

- The TeV astrophysics is the one expected to suffer the best improvements in the next decades. Both EAS and IACT telescopes will be push with new observatories, like the HAWC (81) and the CTA;

- For the PeV energy range, LHAASO (82), in China, already started tacking signals in 2019 and the HiSCORE (Hundred Square-km Cosmic ORigin Explorer) (83) is already under construction in Russia.

4.2 The Cherenkov Telescope Array

The CTA observatory is operated by an international collaboration of more than 1000 scientists from more than 32 countries. The telescopes are still in the construction phase and its first light is expected to be seen in 2022. The scientific projects include understanding the origin of relativistic cosmic particles, probing extreme environments and exploring the frontier of physics, which includes understanding the nature of dark matter.

The main configurations of the CTA observatory are:

- There will be two array of telescopes, located in the two hemispheres: one in the island of La Palma in the Canary Islands (Spain), expected to cover most of extra-galactic sources, and the other near Paranal (Chile), mainly dedicated for galactic observations. Due to this configuration, the CTA will be the first ground-based observatory to cover the entire sky. The spatial configuration of the telescopes, illustrated in figure 21, will cover 4 km^2 in the south and 0.6 km^2 in the north hemisphere.

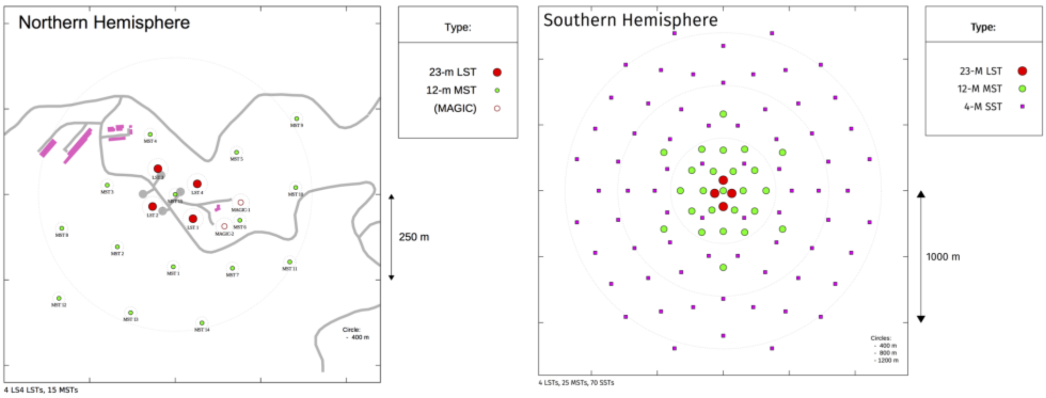

Figure 21 – The configuration of telescopes at the north and south sites.

Source: THE CTA COLLABORATION (10)

- The CTA will explore the energy window from about 20 GeV up to 300 TeV. For this to be accomplished, a complex system with three different sized telescopes was proposed. The Small Sized Telescopes (SST), with 4 m of diameter, are dedicated to the highest energies (1 - 300 TeV), while the Large Sized Telescopes (LST), with 23 m of diameter, will focus on the lowest energies (20 GeV - 3 TeV). The Medium Sized Telescopes (MST) will have 12 m of diameter and will dedicate to the intermediate energies (80 GeV - 50 TeV). Figure 22 brings a schematic view of the three different telescopes.

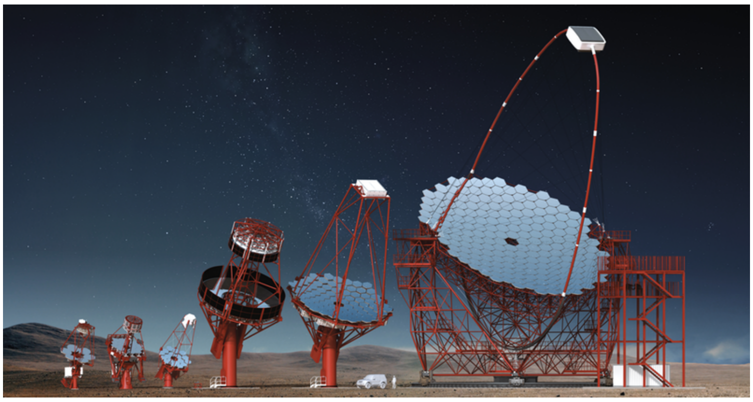

Figure 22 – Schematic representation of telescopes, from left to right: small sized telescope (SST), medium sized telescopes (MST) and large size telescopes (LST).

Source: THE CTA COLLABORATION (40)

- The CTA will have unprecedented sensitivity in the TeV energy region. Figure 23 contains the sensitivity for the south and north sites of CTA and other telescopes from the third generation.

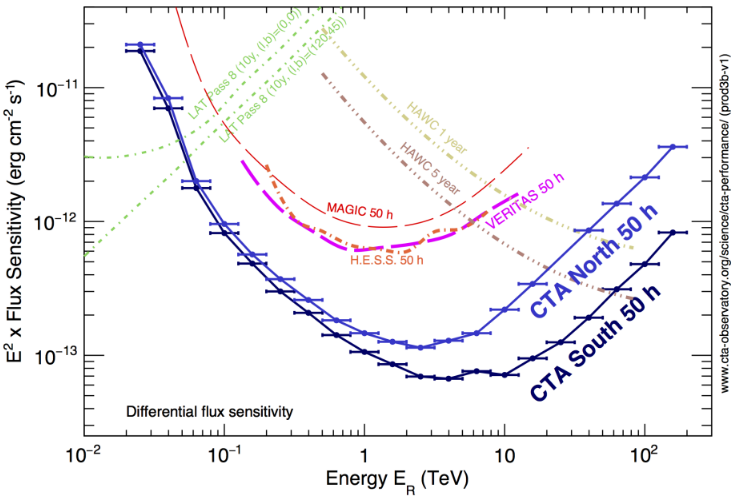

Figure 23 – Differential energy flux sensitivities: CTA south (dark blue) and north (light blue) sites, Veritas (pink-dashed), Magic (orange-dashed) and H.E.S.S. (orange-dashdot), all for 50 hours of sky observation; HAWC for 1 and 5 years of observation and FERMI-LAT for different fields of views. The comparison is only indicative as the criteria applied in the calculation of the curves are different. For the CTA it is required 5σ detection in five independent energy bins in each energy decade, at least ten detected photons in each bin and signal/background ratio of at least 1/20.

Source: THE CTA COLLABORATION (10)

- The CTA is expected to have a few dozens of telescopes in both hemispheres, which enables the detection of different sources simultaneously.

Table 3 – Hours of sky observation from the CTA dedicated to the search of dark matter. In the first three years, 300 hours will be dedicated for observing the best dwarf spheroidal galaxy, and 525 hours, for the galactic center. The strategy for each target after the first three years depends on the first results.

Year	1	2	3	4	5	6	7	8	9	10
Galactic halo	175 h	175 h	175 h							
Best dSph	100 h	100 h	100 h							
				in case of detection at GC, large σv						
Best dSph				150h	150 h	150 h	150h	150 h	150 h	150h
Galactic halo				100h	100 h	100 h	100h	100 h	100 h	100h
				in case of detection at GC, small σv						
Galactic halo				100h	100 h	100 h	100h	100 h	100 h	100h
				in case of no detection at GC						
Best Target				100h	100 h	100 h	100h	100 h	100 h	100h

Source: GASKINS (6)

The CTA targets include the galactic center, the galactic plane, the LMC and other extra-galactic objects. From observing particles coming from these targets, the CTA collaborations expects to get hints of the science behind cosmic-ray PeVatrons, formation of star systems, Active Galactic Nuclei (AGNs) and exotic processes.

The dark matter program will observe the following targets: the Milky Way, dwarf spheroidal galaxies and dark clumps, the Large Magellanic Cloud (LMC) and clusters of galaxies. Table 3 contains the expected observation hours for each target. As can be seen, the Milky Way center is the main target for dark matter searches. However, due to its large uncertainties on account of the high and diverse background, the dSphs will also be a primary target of investigation. The strategy of dSphs observation will be determined according to the results of the first years of observation.

Figure 24 contains the sensitivity of the CTA for the galactic halo, the Sculptor dwarf galaxy and the LMC, together with the sensitivities of H.E.S.S. and Fermi. For a given set of IRFs, the sensitivity of an instrument corresponds to the detection of a point source with test statistics $TS = 25$ (see next chapter for the definition of TS). It is possible to see that the CTA has the best sensitivity for the galactic halo between the telescopes. Moreover, the CTA also has a better sensitivity for dSphs for higher energies.

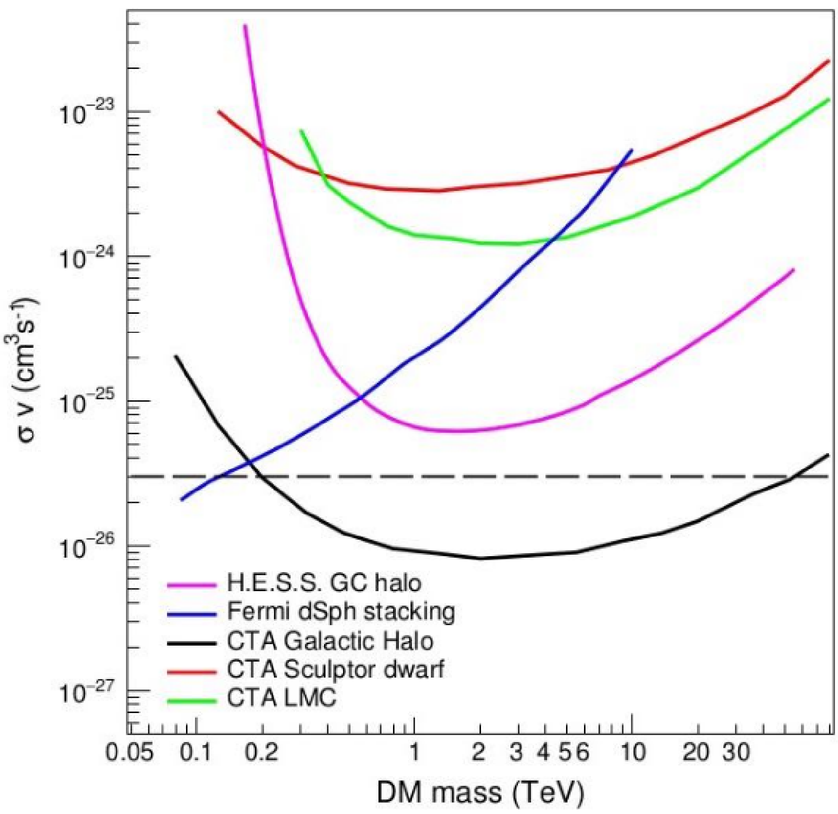

Figure 24 – The constraints on the parameter phase space given by expected observational data of the LMC, Sculptor dwarf galaxy and the galactic halo by the CTA, the galactic halo by H.E.S.S. and dSph by FERMI.

Source: THE CTA COLLABORATION (10)

5 SIMULATING THE DARK MATTER SIGNAL

5.1 Simulating dark matter sources

To evaluate the detectability of Milky Way sub-halos by the CTA it is necessary, first, to simulate the substructure distribution and J-factors. For this purpose, we adopt the `CLUMPY` (84) code, written in C/C++ and developed to calculate gamma-ray and neutrino signals and astrophysical J-factors from dark matter annihilation and decay from the Galaxy and its substructures. The tool also allows the computation of all-sky J-factor maps, calculated for observers at the sun location.

N-body simulations characterise a high clumpiness degree of the dark matter distribution, so that the total dark matter density corresponds to $\rho_{tot} = \rho_{sm} + \langle\rho_{subs}\rangle$, where ρ_{sm} is the average contribution of the smooth galactic halo and ρ_{subs} is the contribution from clumps. The term $\langle\rho_{subs}\rangle$ can be described as

$$\langle\rho_{subs}\rangle = \int_{m_0}^{m_1} m \frac{d^2N}{dV\ dm}(r,m)\ dm \tag{5.1}$$

with

$$\frac{d^2N}{dV\ dm}(r,m) = N_{tot} \times \frac{dP_r}{dV}(r) \times \frac{dP_m}{dm}(m). \tag{5.2}$$

In equation 5.1, m_0 and m_1 are the masses of the lightest and heaviest sub-halos, while in equation 5.2, N_{tot} is the total number of sub-halos, dP_r/dV is the probability function of finding a sub-halo in the volume element of integration and dP_m/dm is the probability function of finding a sub-halo of mass m in the respective mass integration element.

Following equation 3.2, the J-factor from annihilating dark matter is then

$$J = \int_0^{\Delta\Omega} \int_{l_{min}}^{l_{max}} \left(\rho_{sm} + \sum_i \rho_{cl}^i\right)^2\ dl\ d\Omega, \tag{5.3}$$

where ρ_{cl}^i is the inner dark matter density from the i-th sub-halo drawn in the skymap mode, contained in the volume element.

From equation 5.3, three terms arise

$$J_{sm} = \int_0^{\Delta\Omega} \int_{l_{min}}^{l_{max}} \rho_{sm}^2\ dl\ d\Omega, \tag{5.4}$$

$$J_{subs} = \int_0^{\Delta\Omega} \int_{l_{min}}^{l_{max}} \left(\sum_i \rho_{cl}^i\right)^2\ dl\ d\Omega, \tag{5.5}$$

$$J_{cross-prod} = 2 \int_0^{\Delta\Omega} \int_{l_{min}}^{l_{max}} \rho_{sm} \sum_i \rho_{cl}^i \; dl \; d\Omega. \tag{5.6}$$

To calculate the J-factor of a single sub-halo, we need first to define the following quantities: the mean mass

$$\langle M \rangle = \int_{m_0}^{m_1} m \, \frac{dP_m}{dm}(m) \; dm, \tag{5.7}$$

and the mean luminosity

$$\langle \mathcal{L} \rangle (m) = \int_{m_0}^{m_1} \mathcal{L}(m) \, \frac{dP_m}{dm}(m) \; dm, \tag{5.8}$$

in which $\mathcal{L}$ is the intrinsic luminosity of a sub-halo, given by

$$\mathcal{L} \equiv \int_{V_{cl}} \rho_{cl}^2 dV. \tag{5.9}$$

In equation 5.9, ρ_{cl} is the inner dark matter profile of a single sub-halo, integrated in its volume, V_{cl}. Using the point like approximation, the J-factor of a single clump of mass m and distance l is given by

$$J_{cl} = \frac{\mathcal{L}(M)}{l^2}. \tag{5.10}$$

Several steps have to be followed by the code in order to determine how many sub-halos will be drawn in a given mass decade. First, we also define the average distance to the power n as

$$\langle l^n \rangle = \int_0^{\Delta\Omega} \int_{l_{min}}^{l_{max}} l^n \, \frac{dP_r}{dV}(r) \; l^2 \; dl \; d\Omega. \tag{5.11}$$

Combining the equations above, it can be proved that the average contribution in equation 5.5 is given by

$$\langle J_{subs} \rangle = \int_0^{\Delta\Omega} \int_{l_{min}}^{l_{max}} \frac{dP_r}{dV}(r) \; dl \; d\Omega \times \int_{m_0}^{m_1} \mathcal{L}(m) \, \frac{dP_m}{dm}(m) \; dm. \tag{5.12}$$

This contribution can also be written as

$$\langle J_{subs} \rangle = \langle n_{cl} \rangle \langle J_{cl} \rangle \,, \tag{5.13}$$

in which $\langle n_{cl} \rangle$ is the average number of sub-halos in the volume determined by an integration angle α_{int}, line of sight $[l_{min}, l_{max}]$ and mass range $[m_0, m_1]$. $\langle J_{cl} \rangle$ is the average J-factor of the sub-halos, given by

$$\langle J_{cl} \rangle = \langle \mathcal{L}(M) \rangle \left\langle \frac{1}{l^2} \right\rangle. \tag{5.14}$$

The variance in the J-factor of single sub-halos is given by

$$\sigma_{cl}^2 = \langle J_{cl}^2 \rangle - \langle J_{cl} \rangle^2 = \langle \mathcal{L} \rangle^2 \left\langle \frac{1}{l^4} \right\rangle - \langle J_{cl} \rangle^2 . \tag{5.15}$$

Therefore, the variance of a population $\langle n_{cl} \rangle$ of sub-halos is

$$\sigma_{n_{cl}}^2 = \langle n_{cl} \rangle \, \sigma_{cl}^2. \tag{5.16}$$

For a specific *l.o.s.* domain of integration, there is a mass limit above which the average description fails, because the number of clumps is not numerous enough. For the same reason, for each mass decade, there is a critical distance l_{crit} below which sub-halos should be resolved. The average description, however, can be safely used as long as the relative error of the clump component with respect to the total J-factor, given by

$$RE = \frac{\sqrt{n_{cl}}\sigma_{cl}}{n_{cl} \langle J_{cl} \rangle + J_{sm}}, \tag{5.17}$$

is not above a threshold set by the user.

Figure 25 shows the relation between RE and l_{crit} for a sky direction towards the galactic center (blue), towards the galactic East (red) and towards the anti-centre (black). Dashed lines represent values for $\alpha_{int} = 0.01°$, while solid lines, $\alpha_{int} = 0.1°$. The results from figure 25 are valid for the 1 - 10 $M_\odot$ mass decade.

As exemplified in figure 25 by the green line, the l_{crit} for a required precision of 5% is 2 kpc for a direction towards the anti-center and for $\alpha_{int} = 0.1°$. For all precisions, the codes sets a l_{crit} of at least $l_{crit}^0 = 10^{-3}$ kpc.

The average number of clumps to be drawn in the mass decade $[m_{d0}, m_{d1}]$ is, then, given by

$$\langle n_{cl} \rangle = N_{tot} \times \int_{m_{d0}}^{m_{d1}} \frac{dP_m}{dm}(m) \, dm \times \int_{l_{crit}^0}^{l_{crit}} \frac{dP_r}{dV}(r) \, dV. \tag{5.18}$$

The true number of sub-halos n_{cl} in that mass decade and below a certain l_{crit} is defined by a Poisson distribution with mean $\langle n_{cl} \rangle$.

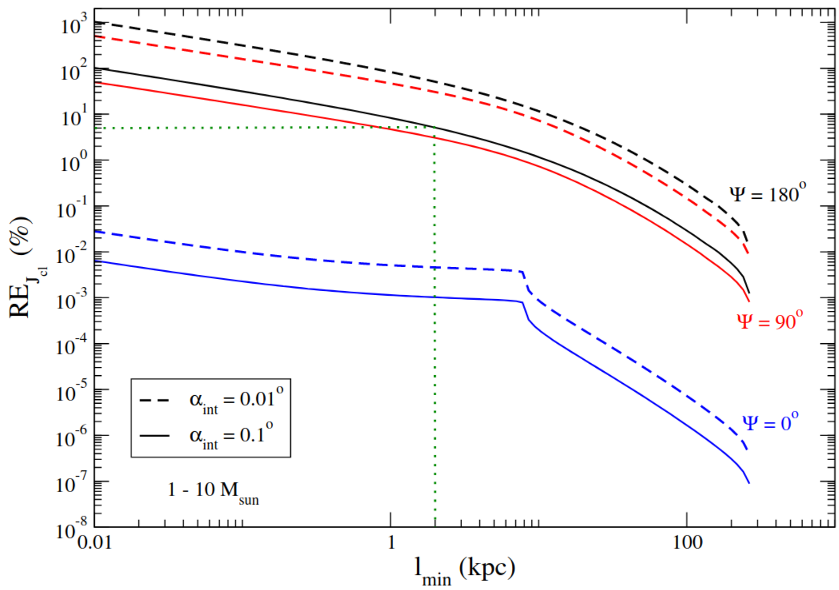

Figure 25 – The relation between the relative error of the clump component with respect to the total J-factor (equation 5.17) and the value of l_{crit} below which sub-halos are drawn in the [1-10] M$_\odot$ mass decade, for observers located at the galactic center (blue), towards the galactic East (red) and towards the anti-centre (black) for integration angles of $\alpha_{int} = 0.01°$ (dashed-line) and $\alpha_{int} = 0.1°$ (solid-line). The value of l_{crit} is determined at the point that corresponds to the maximum relative error, set by the user.

Source: CHARBONNIER (85)

An example of the number n_{cl} for each mass decade and the correspondent l_{crit} is shown in table 4.

Calculating the J-factor of astrophysical objects requires the definition of a set of physical parameters related to the host and sub-halos. Such parameters can be varied to study the impact on the J-factors of substructures, therefore, the impact on the detection of a gamma-ray signal from dark matter annihilation.

Our modelling of the Milky Way start by setting its inner dark matter profile by an Einasto parametrisation, with $\alpha = 0.17$ and $r_s = 15.14$ kpc. (86) The ρ_s parameter is determined by knowing the local density of dark matter: $\rho(R_\odot = 8.5 \text{ kpc}) = 0.4 \text{ GeV}^2/\text{cm}^5$. In the simulations, all clumps are set to have the same parametrisation profile as the host halo, but with different parameters ρ_s and r_s. The dark matter halo of the Milky Way is set to extent until $R_{vir} = 260$ kpc and has a mass $M_{vir} = 1.1 \times 10^{12}$ M$_\odot$ (86). The second modelling of the Milky Way halo is set by a NFW parametrisation, with $r_s = 15.14$ kpc.

The series of parameters corresponding to sub-halos can be independently chosen from the ones of the host halo. We analyse 10 substructure models, summarised in table 6. The first model, defined as SM1, is set as a default model, to which comparisons regarding simulated sub-halos will be made. Below we analyse the varied criteria:

Table 4 – An example of total number of clumps, l^0_{crit}, $\langle n_{cl}\rangle$ and n_{cl} to be drawn in each mass decade.

Mass decade $\log_{10}\left(\frac{M_{\rm cl}}{M_\odot}\right)$	# clumps (Galaxy)	$l_{\rm crit}$ (kpc) kpc	<# clumps> $(5^\circ \times 5^\circ)$	# to draw $(5^\circ \times 5^\circ)$
$-6:-5$	3.5×10^{14}	1.0×10^{-3}	1.5×10^{-3}	0
$-5:-4$	4.4×10^{13}	1.0×10^{-3}	1.8×10^{-4}	0
$-4:-3$	5.6×10^{12}	1.0×10^{-3}	2.4×10^{-5}	0
$-3:-2$	7.0×10^{11}	7.3×10^{-3}	1.2×10^{-3}	0
$-2:-1$	8.8×10^{10}	5.8×10^{-2}	7.6×10^{-2}	0
$-1:0$	1.1×10^{10}	4.0×10^{-1}	2.8	3
$0:1$	1.4×10^{9}	2.0	$3.7\times10^{+1}$	45
$1:2$	1.7×10^{8}	6.7	$1.0\times10^{+2}$	117
$2:3$	2.2×10^{7}	1.6×10^{1}	$8.7\times10^{+1}$	99
$3:4$	2.8×10^{6}	3.3×10^{1}	$3.6\times10^{+1}$	44
$4:5$	3.5×10^{5}	5.8×10^{1}	$1.0\times10^{+1}$	7
$5:6$	4.4×10^{4}	9.5×10^{1}	2.2	1
$6:7$	5.6×10^{3}	1.5×10^{2}	4.1×10^{-1}	0
$7:8$	7.0×10^{2}	2.5×10^{2}	6.6×10^{-2}	0
$8:9$	8.8×10^{1}	2.9×10^{2}	9.5×10^{-3}	0
$9:10$	1.1×10^{1}	2.9×10^{2}	1.3×10^{-3}	0

Source: CHARBONNIER (85)

- *sub-halos inner profile*: in the code, all substructures have the same parametrisation for the inner profile. We set an Einasto (E) profile ($\alpha = 0.17$, such as for the MW) as default and analyse in model SM2 the effect of a NFW parametrisation for the sub-halos and host.

- *Spatial distribution of sub-halos:* the spatial distribution of sub-halos dP_r/dV is usually set via results of N-body simulations. We test the spatial distribution of the total population of satellites expected by N18, described by

$$\frac{dP_r}{dV} = \rho_0 \, exp\left[-\frac{2}{\alpha}\left(\left(\frac{r}{r_s}\right)^{\alpha} - 1\right)\right], \tag{5.19}$$

with $r_s = 43.0$ kpc and $\alpha = 0.24$; the radial distribution from H14,

$$\frac{dP_r}{dV} = \frac{\rho_0}{1 + \frac{r}{r_s}}, \tag{5.20}$$

with $r_s = 37.5$ kpc, and the model from K8, described by

$$\frac{dP_r}{dV} = \frac{\rho_0}{\frac{r}{r_s}\left(1 + \frac{r}{r_s}\right)^2}, \tag{5.21}$$

with with $r_s = 16.7$ kpc [1]. In equations 5.19, 5.19 and 5.21, ρ_0 is a normalisation

[1] Instead of using $r_s = 10$ kpc, as suggested by K8, we decide to slightly increase this parameter by a factor of 1.1 in respect with the typical scale radius of the MW. This is done so the radial distribution of substructures is not steeper than the dark matter distribution of the host.

parameter, such that $\int \frac{dP_r}{dV}\, dV = 1$. The plot of the three different options for the radial distribution is shown in figure 26.

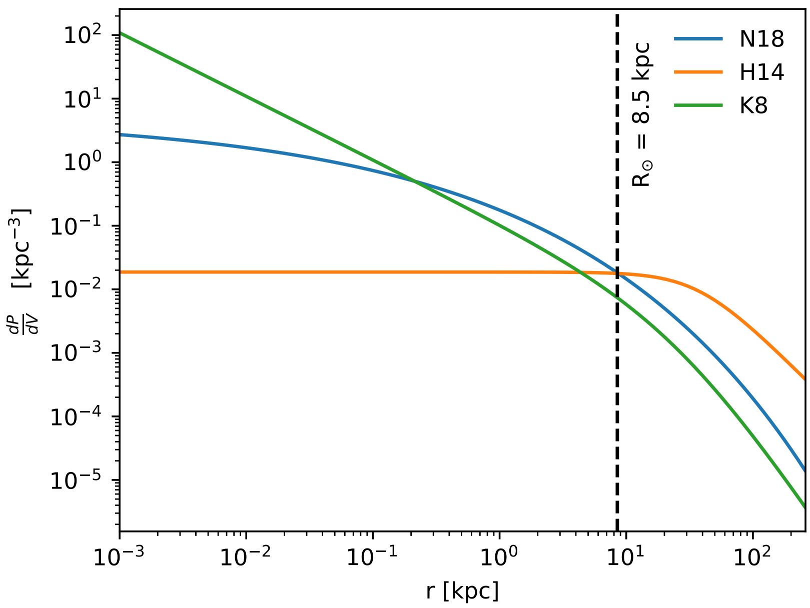

Figure 26 – The radial distribution of sub-halos around the host halo from N18 (magenta), H14 (orange) and modified K8 (green).

Source: By the author

- *Mass distribution of sub-halos:* `AQUARIUS` and `ELVIS` simulations show that the mass distribution of sub-halos follows a power law such as

$$\frac{dP_m}{dm} = a_0 \left(\frac{m}{m_0}\right)^{-\alpha_m}, \tag{5.22}$$

in which a_0 is a normalisation parameter so that $\int \frac{dP_m}{dm}\, dm = 1$. The spectral index α_m can assume the values 1.9 or 1.95, for the `AQUARIUS` or `ELVIS` set of simulations, respectively. This determines $\alpha_m = 1.9$ and $\alpha_m = 1.95$ for the N18 and H14 models, respectively. We also analyse a variation of $\alpha_m = 2.0$ in model SM3, while assuming the radial profile from N18. Because the model K8 is not based on the results of simulations, we assumed the same mass distribution as the one from N18.

- *Number of sub-halos:* To determine the the total number of substructures to be resolved (N_{tot}) in each all-sky simulation, it is necessary a calibration number of sub-halos N_{calib} between a certain mass range $[m_{min}, m_{max}]$. Table 5 summarizes the calibration number of sub-halos predicted by the studies from N18, H14 and K8. The values of m_{min} is defined by the mass resolution of the correspondent simulation. The value of m_{max} is determined by, first, knowing the differential sub-halo abundance by mass, $\frac{dN_m}{dm}$, for each simulation. Following, m_{max} is such that $\int_{m_{max}}^{M_{vir}} \frac{dN_m}{dm}(m)\, dm$ < 1. Since no assumption about the mass distribution is made by K8, we assume the same mass range of N18. For the N18 model, we test the mean (m.), set as the default value, upper limit (u. l.) and lower limit (l. l.) for the expected number of sub-halos in models SM1, SM5 and SM6, respectively. For the H14 model, we test the upper limit and lower limit of the expected number of sub-halos in models S10 and S11, respectively. For K8, we use equation 3.5 to calculate the total number of sub-halos between M_V = -20 and M_V = 0.

Table 5 – Values of N_{calib} and respective mass range for each radial model. From N18, we test the mean value, upper and lower limits of the 68 % C. L. of the expected total population of sub-halos. From H14 we test only the upper and lower limits of the 90 % C. L. For K8, we use equation 3.5 to calculate the total number of sub-halos between M_V = -20 and M_V = 0. The mass range $[m_{min}, m_{max}]$ is set by the resolution of the `AQUARIUS` (N18) and `ELVIS` (H14) set of simulations and by the value of m_{max} such that $\int_{m_{max}}^{M_{vir}} \frac{dN_m}{dm}(m)\, dm < 1$. Because the model K8 is not based on results of dark matter simulations, it receives the same inputs as N18 for the characterisation of the mass distribution.

Model	N_{calib} $(< R_{vir})$	$[m_{min}, m_{max}]$ $(M_\odot, M_\odot)$
N18 (68 % m. C. L.)	115	$[2 \times 10^5, 1 \times 10^{11}]$
N18 (68 % u. l. C. L.)	151	$[2 \times 10^5, 1 \times 10^{11}]$
N18 (68 % l. l. C. L.)	90	$[2 \times 10^5, 1 \times 10^{11}]$
H14 (90 % u. l. C. L.)	896	$[2.35 \times 10^4, 2.14 \times 10^9]$
H14 (90 % l. l. C. L.)	168	$[2.35 \times 10^4, 2.14 \times 10^9]$
K8 (-20 < M_V < 0)	136	$[2 \times 10^5, 1 \times 10^{11}]$

Source: By the author

With N_{calib} given, N_{tot} is defined by

$$N_{tot} = \frac{N_{calib}}{\int_{m_{min}}^{m_{max}} \frac{dP_m}{dm}\, dm}. \tag{5.23}$$

- *The concentration parameter,* c_{200}: once the inner profile is chosen, r_s and ρ_s can be determined by the mass-concentration relation. Possible c_{200} for sub-halos are chosen from results given in reference (87) (MO17), based on results of Via-Lactea II and `ELVIS` simulations, and from results given in reference (88) (P11), calculated for sub-halos from the `AQUARIUS` set of simulations. The c_{200} from MO17 is described by

$$c_{200}(m_{200}, x_{sub}) = a_0 \left\{ 1 + \sum_{i=1}^{3} a_i \times \left[log\left(\frac{m_{200}}{10^8 h^{-1} M_\odot} \right) \right]^i \right\} \times \left[1 + a_4\, log(x_{sub}) \right], \tag{5.24}$$

where $x_{sub} \equiv r/R_{vir}$ is the ratio between the distance of the sub-halo from the host by the virial radius of the host and $a_i = \{19.9, -0.195, 0.089, 0.089, -0.54\}$. The concentration relation from P11 is given by

$$c_{200}(m_{200}, r) = \left(\frac{r}{R_{vir}}\right)^{\alpha_R}\left[c_0 \times \left(\frac{m_{200}}{M_\odot}\right)^{\alpha_0} + c_1 \times \left(\frac{m_{200}}{M_\odot}\right)^{\alpha_1}\right], \tag{5.25}$$

in which $(c_0, c_1, \alpha_0, \alpha_1, \alpha_R, R_{AQ})$ = (119.75, -85.16, -0.012, -0.0026, 0.286, 433 kpc). Figure 27 illustrates both parametrisations.

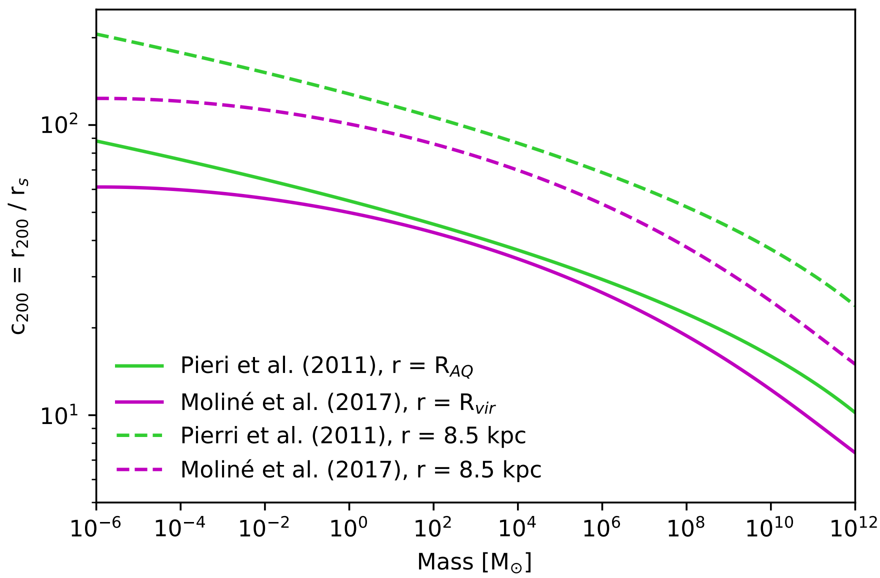

Figure 27 – The MO17 (P11) concentration parameter in magenta (green) for $r = 8.5$ kpc (dashed line), and $r = R_{vir}$ (solid line).

Source: By the author

We set MO17 as the default concentration relation and analyse the effect of P11 in model SM8.

- *Scattering of* c_{200}*:* N-body simulations show a halo-to-halo scatter in the concentration relation of sub-halos. (89) The scatter is assumed to be a log-normal, of constant width σ_{200} and mean $\bar{c}_{200}(m_{200}, R_{sub})$:

$$\frac{dP_c}{dc}(c, \bar{c}_{200}) = \frac{exp\left[-\left(\frac{ln\ c - ln\ \bar{c}_{200}}{\sqrt{2}\sigma_{200}}\right)^2\right]}{\sqrt{2\pi}\ c\ \sigma_{200}}. \tag{5.26}$$

The value $\sigma_{200} = 0.14$ is suggested P11 for the concentration relation of `AQUARIUS` sub-halos. As for MO17, the typical scatter is $\sigma_{200} = 0.11$, tested in model SM4, and $\sigma_{200} = 0.13$, set as default, for sub-halos resolved from `ELVIS` and Via Láctea II (90), respectively.

As we saw that c_{200} suffers a scattering, we can update equation 5.2 to

$$\frac{d^3N}{dV\ dm\ dc} = N_{tot} \times \frac{dP_r}{dV}(r) \times \frac{dP_m}{dm}(m) \times \frac{dP_c}{dc}(c, \bar{c}_{200}). \tag{5.27}$$

Table 6 – Summary of set of parameters for each model. The varied criteria are: the inner profiles of substructures, the radial distribution, the index of power law that described the mass distribution (α_m), the calibration number of substructures (N_{calib}), the concentration relation (c_{200}), the scatter of the concentration relation σ_{200}, and the presence of sub-sub-halos.

Parameter	SM1	SM2	SM3	SM4	SM5	SM6	SM7	SM8	SM9	SM10
inn. prof.	E	NFW	E	E	E	E	E	E	E	E
spat. dist	N18	N18	N18	N18	N18	N18	N18	K8	H14	H14
α_m	1.9	1.9	2.0	1.9	1.9	1.9	1.9	1.9	1.95	1.95
N_{calib}	115	115	115	115	151	90	115	136	896	168
c_{200}	MO17	MO17	MO17	MO17	MO17	MO17	P11	MO17	MO17	MO17
σ_{200}	0.13	0.13	0.13	0.11	0.13	0.13	0.14	0.13	0.13	0.13

Source: By the author

For each model SMi defined in table 6, we computed 500 sky-maps with the `CLUMPY` code. From each simulated sky-map, we select only the brightest one to proceed the analysis. This leads to a list with only the 500 brightest sub-halos resolved in all simulations, for each model. Following, we calculate the 95 % C. L. J_f^i $i \in \{1, ..., 10\}$ from this sample of sources. Finally, the gamma-ray flux is calculated for a sub-halo with J-factor given by 95 % upper limit (u. l.) C. L. J_f^i and 95 % lower limit (l. l.) C. L. J_f^i.

With the values of J-factors in hands, the gamma-ray differential flux is determined via equation 3.1. We analyse the $\tau^+\tau^-$ and $b\bar{b}$ annihilation channels, because of their different shapes of the dark matter spectrum. For each channel, we assume 100 % branching ratio.

5.2 Simulating the photon flux from dark matter sources

We use the CTOOLs package (91, 92), a software developed to perform a scientific analysis of IACTs data, to simulate signal and background events and to perform the subsequent analysis. CTOOLs was developed based on the `gammalib` package, which comprises a set of tools for the investigation of gamma-ray physics. Besides the CTA, `gammalib` also supports the scrutiny of other IACTs (such as H.E.S.S., MAGIC and VERITAS), which allows the joint analysis of instruments by CTOOLs.

As described in section 4.1, the IRFs of an instrument convert the measured data of a photon into its true physical quantities. The chosen IRFs for a CTA analysis depend on the following parameters:

- site (north or south) used for source observation;
- the right ascension (RA) and declination (DEC) of the source;
- the radius of the CTA field of view;
- the total observation time (t_{obs});
- the calibration database (caldb)[2];
- the number of telescopes active in the observation;
- the type of telescopes active in the observation (SST, MST, LST).

The IRFs of CTA are indexed by three information: the site of observation, the observation angle of the telescope from the zenith and the observation time. A sketch of the CTOOLs functions used in the analysis is shown in figure 28.

First, observation definition files from a pointing list are generated with *csobsdef*. Each observation definition file contains n_{obs} observations, characterized by the observation name, a string that uniquely identifies the observation, the RA and DEC of the source, the duration of pointing in hours, the maximum and minimum energy of photons, the radius of the region of interest, the dead-time correction [3], the name of the instrument response function and the calibration database. The duration of pointing is set to 5h. Therefore, an observation definition file with $n_{obs} = 60$ corresponds to a total of 300 h of observation. We calculate the parameter phase space for 300 h ($n_{obs} = 60$).[4].

Next, *ctobssim* simulates photon counts from the astrophysical source and background using the parameters in the observation definition files. Moreover, *ctobssim* requires a model input file, that describes the background model [5] and the spectrum and spatial

[2] CTOOLs uses the HEASARC-NASA (93) calibration database format to store IRFs. The last calbd released by the CTA collaboration was *prodb3-v2* (40).

[3] The dead-time correction is set to 5%. Therefore, the during 0.05 t_{obs} no data is recorded, and the overall observation time is $t_{live} = 0.95\ t_{obs}$.

[4] Note that the total time held for dSPhs observation in the first 3 years of CTA operation is 300 h.

[5] The CTA IRFs already contain the expected background rate as a function of the position and measured energy. Therefore, using the `CTAIrfBackground` pre-defined model, there is no need to define a spatial parametrisation for the background, as it is already contained as a template from the IRF. This spectral model is multiplied by a power law with free spectral index and normalisation, i.e., contains 2 degrees of freedom, that will be fitted according to the simulated background events.

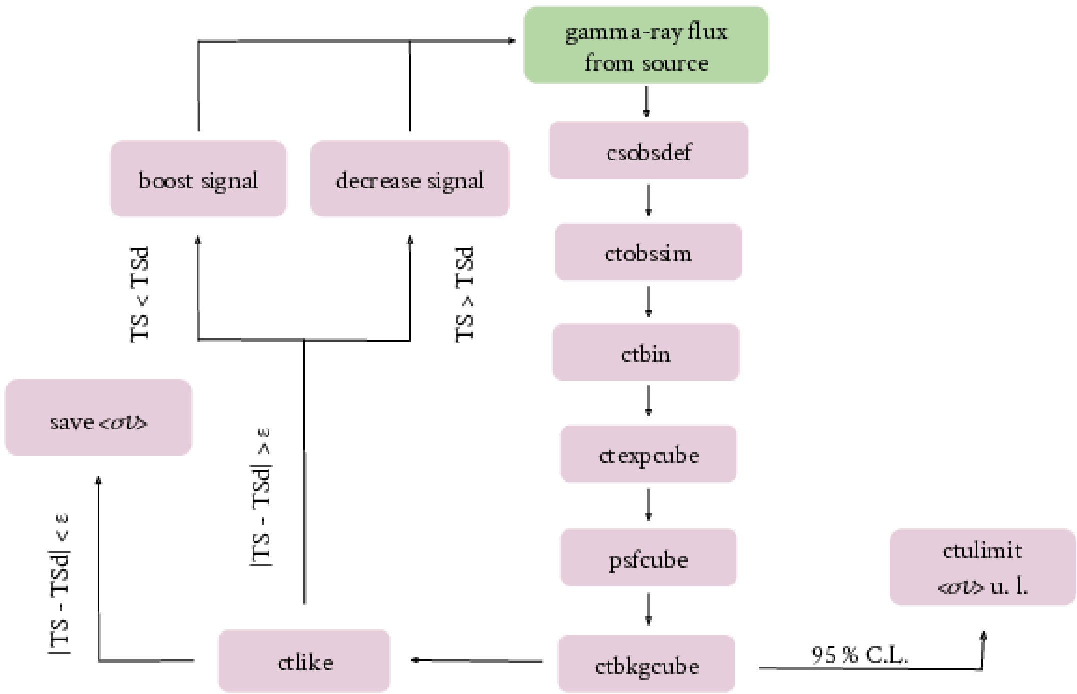

Figure 28 – A sketch of the CTOOLs functions used to calculate the parameter phase space for WIMP annihilation with the CTA. The analysis is separated in two methods: detection of a signal with CTA (ctlike) and no detection (ctulimit). In the last case, only the upper limit of $\langle \sigma v \rangle$ will be known.

Source: By the author

models of the source. The spectrum of the source is stored in a table of the energy versus the differential gamma-ray signal, calculated as described in the last section.

The function *ctbin* is used to divide the events generated by *ctobssim* into energy bins specified by the user. This step saves a considerable amount of time when running the script.

An exposure cube is then generated using *ctexpcube*. An exposure cube is a 3-dimensional cube with axis established by Right Ascension (RA), Declination (DEC) and energy, that gives the exposure as function of true sky direction and energy.

Following, a point spread function (PSF) cube is generated with *ctpsfcube*. A point spread function cube is a 4-dimensional cube spanned by Right Ascension (RA), Declination (DEC), energy and offset angle between true and measured arrival direction of a photon.

A background cube based on the input model is created with *ctbkgcube*. A background cube is a 3-dimensional cube spanned by Right Ascension (RA), Declination (DEC) and energy. The input model is used to define the expected number of background events in each cube bin.

The last step of the analysis is the calculation of the expected $\langle\sigma v\rangle$ for the astrophysical model. This step is divided into *i) detection of a signal with CTA* and *ii) no detection of a signal*, i.e., the calculation of the $\langle\sigma v\rangle$ upper limit with 95% C. L.

- In *i)*, the function *ctlike* performs a maximum likelihood fitting of the model to the binned data. In this context, $\langle\sigma v\rangle$, which is marked as free parameter, is adjusted to the value that maximises the probability that the data corresponds to the model. *ctlike* also computes the Test Statistics (TS), which measures the source significance.

  Given a model hypothesis $\mathcal{M}$ to be tested within a dataset, the likelihood ratio λ is

$$\lambda = \frac{\mathcal{L}(\mathcal{M}_{bkg}(\mathbf{\Theta}_{bkg})|\mathbf{X})}{\mathcal{L}(\mathcal{M}_{bkg}(\mathbf{\Theta}_{bkg}) + \mathcal{M}_{sig}(\mathbf{\Theta}_{sig})|\mathbf{X})}, \tag{5.28}$$

  where $\mathbf{X} = (N_{obs}, E', \mathbf{p}')$ stores the simulated number of events, reconstructed energy and reconstructed incident direction of the photons. $\mathbf{\Theta}$ contains the adjusted free parameters that maximise the likelihood function $\mathcal{L}$. The function λ tests whether the probability of only background events, known as alternative hypothesis, is statistically preferable over the null hypothesis, i.e. the presence of background and signal events. In the case of the source model, $\mathbf{\Theta}_{sig} = \langle\sigma v\rangle$, which adds one more degree of freedom to the statistics. In equation 5.28,

$$\mathcal{L}(\mathcal{M}|N_{obs}, E', \mathbf{p}') = \wp(N_{obs}|N_{pred}(\mathcal{M})) \times \prod_{1}^{N_{obs}} \wp(E'|\mathcal{M}), \tag{5.29}$$

  in which N_{pred} is the number of predict events, N_{obs} is the number of observed events and $\wp$ is a Poisson distribution. Given a Poisson distribution of events,

$$\wp(N_{obs}|N_{pred}) = \frac{N_{pred}^{N_{obs}} e^{-N_{pred}}}{N_{obs}!}. \tag{5.30}$$

  The total number of expected events is set by

$$N_{pred} = t_{obs} \int_{E'} \int_{\Delta\Omega} \wp(E', \mathbf{p}'|\mathcal{M})\, dE'\, d\Omega, \tag{5.31}$$

  where $\wp(E, \mathbf{p}|\mathcal{M})$ is the probability that an event with energy E and incident direction $\mathbf{p}$ has been drawn from the differential intensity $\frac{d\Phi_{\mathcal{M}}}{dE\, d\Omega}$ of the model, integrated over the solid angle, effective area and energy after convolved with the instrument response:

$$\wp(E', \mathbf{p}'|\mathcal{M}) = \int_{E,\Delta\Omega,A_{eff}(E)} \wp(E'|E, \mathbf{p}) \times \wp(\mathbf{p}'|E, \mathbf{p}) \times \frac{d\Phi_{\mathcal{M}}}{dE\, d\Omega}(E, \mathbf{p})\, dA_{eff}\, d\Omega\, dE. \tag{5.32}$$

In the last equation, E and $\mathbf{p}$ are the true energy and incident direction of photons, $\wp(E'|E, \mathbf{p}) = \delta(E - E')$ and $\wp(\mathbf{p}'|E, \mathbf{p})$ is modelled as a 2-dimensional Gaussian distribution whose width depends on the energy. For the source model, $\frac{d\Phi_{\mathcal{M}_{sig}}}{dE\, d\Omega}$ is given by equation 3.1, while for the background, $\frac{d\Phi_{\mathcal{M}_{bkg}}}{dE\, d\Omega}$ is the irreducible residual of the background from cosmic rays.

The Test Statistics of a likelihood λ,

$$TS = -2\ log\lambda, \tag{5.33}$$

is used to reject the alternative hypothesis at a given confidence level. According to the Wilks theorem (94), TS asymptotically approaches a χ^2 distribution with a number of degrees of freedom n_{dof} given by the difference of free parameters from the alternative and null hypothesis [6]. This is true under the hypothesis that the input model $\mathcal{M}$ provides an adequate fit of the data.

In a scenario that the test statistics has no significance ($TS_d < 2.71$, i.e, C. L. ≈ 1.6 σ), the alternative hypothesis can not be rejected. On the other hand, if $TS_d > 25$ (i.e, $> 5\sigma$ C. L.), the alternative hypothesis can be rejected and it is known that a dark matter signal was identified by the CTA.

In this analysis, we set a tolerance of $\epsilon = \pm 3.5$ in the value of TS. In case $|TS - TS_d|$ $< \epsilon$, the fitted value of $\langle\sigma v\rangle$ is saved. In the case of $|TS - TS_d| > \epsilon$, the gamma-ray flux from the astrophysical source is boosted or reduced by a multiplicative factor μ,

$$\frac{d\phi_\gamma}{dE} = \mu \frac{\langle\sigma v\rangle}{4\pi m_\chi^2} \frac{dN_f}{dE} \times J_f. \tag{5.34}$$

Practically, this is done by modifying a prefactor that multiplies the source spectrum in the input model file. This procedure effectively means that the value of $\langle\sigma v\rangle$ is increased or reduced.

In this scenario, we compute the dark matter parameter phase space for a total observation time of 300 h.

- At the *ii)* scenario, the value of the velocity averaged cross-section is set to $\langle\sigma v\rangle =$ 10^{-28} cm^3/s for the calculation of the source spectrum. This value is low enough to guarantee that only background events will be simulated, i.e., $TS < 2.71$. In this case, it is necessary to find the parameters from the source model $\mathcal{M}_{sig,up}$ that leads to a decrease $\Delta ln\mathcal{L}$ of the log-likelihood with respect to the maximum log-likelihood estimate:

$$\Delta ln\mathcal{L} = max(ln\mathcal{L}(\mathcal{M}_{bkg}(\mathbf{\Theta}_{bkg}) + \mathcal{M}_{sig}(\mathbf{\Theta}_{sig})|\mathbf{X})) - ln\mathcal{L}(\mathcal{M}_{sig,up}(\mathbf{\Theta}_{sig})|\mathbf{X}). \tag{5.35}$$

[6] In this case, $n_{dof} = 1$.

The value of $\Delta ln\mathcal{L}$ is calculated from the chance probability (p-value) associated with a C. L. defined by the user:

$$\Delta ln\mathcal{L} = (erf^{-1}(p))^2. \tag{5.36}$$

CTOOLS uses the iterative Levenberg-Marquardt algorithm (91, 95) to calculate the maximum log-likelihood estimate. The calculation of the $\langle \sigma v \rangle$ is done with the routine *ctulimit* for a 95% C. L. The output of $\langle \sigma v \rangle$ corresponds, in this case, to the upper limit of the velocity averaged cross-section.

In both *i*) and *ii)* scenarios, the $\langle \sigma v \rangle$ value is calculated for a dark matter particle mass ranging from 0.15 TeV to 100 TeV.

6 RESULTS AND DISCUSSION

The sensitivity of the CTA can be applied to the gamma-ray flux generated by annihilating dark matter, giving the sensitivity curve of the source, i.e, $\langle\sigma v\rangle \times m_\chi$. This chapter is ordered as follows: in section 6.1, we present the distribution of J_f and characteristics of the sources resolved with the `CLUMPY` sky-mode. Section 6.2 brings the sensitivity curves in case of detection with the CTA (Section 6.2.1) for each model contained in table 6. Section 6.2.2 contains the same results, but in event of no detection with the CTA.

6.1 Simulation of the CTA skymaps

For each model presented in table 6 we calculated 500 sky-maps with the `CLUMPY` code. In each realisation, it was selected the sub-halo with the highest J_f. The distribution of the 500 highest J_f^i, from models SM$_i$ $i \in \{1, ..., 10\}$, is shown in Appendix A.

Table 7 shows the mean right ascension ($\widetilde{\mathrm{RA}}$), declination ($\widetilde{\mathrm{DEC}}$), distance to the observer ($\widetilde{D_{obs}}$), virial mass ($\widetilde{M_{200}}$) and J-factor ($\widetilde{J_f}$) of the 500 brightest sub-halos resolved in each model. It also brings the median ($\widehat{J_f}$) maximum (J_f^{max}), lowest (J_f^{min}), 95 % C. L. upper limit (95 % C. L. u. l. J_f^i) and 95 % C. L. lower limit (95 % C. L. l. l. J_f^i) J-factors among the set. Statistically, the 95 % C. L. interval means that for each simulated sky-map there is a 95 % probability that the highest J_f resolved will lie between the proposed range. This interval, however, is not a definitive range of plausible results. Instead, it is an estimation based on the observed data. The higher the number of simulations used in the calculation of the confidence level, the more precise is the interval. We run 500 realisations of each model due to the time to generate each sky-map, which takes in average 15 minutes to be complete.

From table 7, it is possible to infer the following of $\widehat{\mathrm{J}}_f^i$ from model SM$_i$ in respect to $\widehat{\mathrm{J}}_f^1$ [1]:

- Assuming the NFW profile for the host and substructures, with the same r_s, M_{200} and c_{200} parameters in respect with model SM1, the flux of gamma-rays is reduced by 52%;

- Increasing the slope of the mass distribution to $\alpha_m = 2.0$, the flux of gamma-rays is reduced by 15 %. A steeper mass distribution favours lower mass sub-halos to be resolved, what could explain the lower $\widehat{\mathrm{J}}_f^3$;

1 Keep in mind that the J_f acts as a boost or decrease of the flux of gamma-rays, as it is pointed in equation 3.1.

- Reducing the σ_{200} to 0.11, only decreases $\widehat{\mathrm{J}}_f$ by 4%;
- Considering N_{calib} = 151 (N18 68 % u. l. C. L.), increases $\widehat{\mathrm{J}}_f^5$ by a factor 1.2. The left panel of figure 29 plots the histogram of the mass distribution from both models. Each histogram was divided in 15 logarithmic bins from the lower to the higher sub-halo mass of the resolved sub-halos in each set. The mass distribution from SM5 has a tail towards higher masses that overcomes the one from SM1 for $\mathrm{M}_{200} > 1.0 \times 10^9\ \mathrm{M}_\odot$. Indeed, SM5 has 3 times more sub-halos with $\mathrm{M}_{200} > 1.0 \times 10^9\ \mathrm{M}_\odot$ than SM1, which shifts the $\widehat{\mathrm{J}}_f^5$ to the right;
- On the other hand, considering N_{calib} = 90 (N18 68 % l. l. C. L.), $\widehat{\mathrm{J}}_f^6$ is decreased by a factor 0.7. By analysing the mass distribution of SM1 and SM6 in the right panel of figure 29, it is seen that in SM6 more low mass sub-halos were resolved in comparison with SM1, which shifts the $\widehat{\mathrm{J}}_f^6$ to the left;
- Setting c_{200} to the P11 parametrisation provided one of the most significant effects in the flux of particles, which was boosted by a factor of 1.9;
- For model SM8, $\widehat{\mathrm{J}}_8$ was reduced by 40%;
- Considering the radial distribution of sub-halos given by H14 and N_{calib} = 896 (H14 90 % u. l. C. L.), $\widehat{\mathrm{J}}_f^9$ is reduced by a factor of 0.15;
- Considering the radial distribution of sub-halos given by H14 and N_{calib} = 168 (H14 90 % l. l. C. L.) provided the most drastic change in comparison with the default model, with $\widehat{\mathrm{J}}_f^{10}$ reduced by a factor of 0.03.

We can conclude that the inner dark matter profile, the value of N_{calib}, the parametrisation of c_{200} and the radial distribution of sub-halos provided the most drastic changes in comparison with the default model.

It is interesting to note from table 7 that $\widetilde{\mathrm{RA}}$ and $\widetilde{\mathrm{DEC}}$ do not coincide with the position of the galactic center (RA = 266.4°, DEC = -28.9°), which could disfavour the observation of the sources due to the astrophysical background. In fact, for all models, $\widetilde{\mathrm{DEC}}$ is located in the south hemisphere.

In the next section we show the results of applying the sensitivity of the CTA to the gamma-ray flux generated by annihilating dark matter.

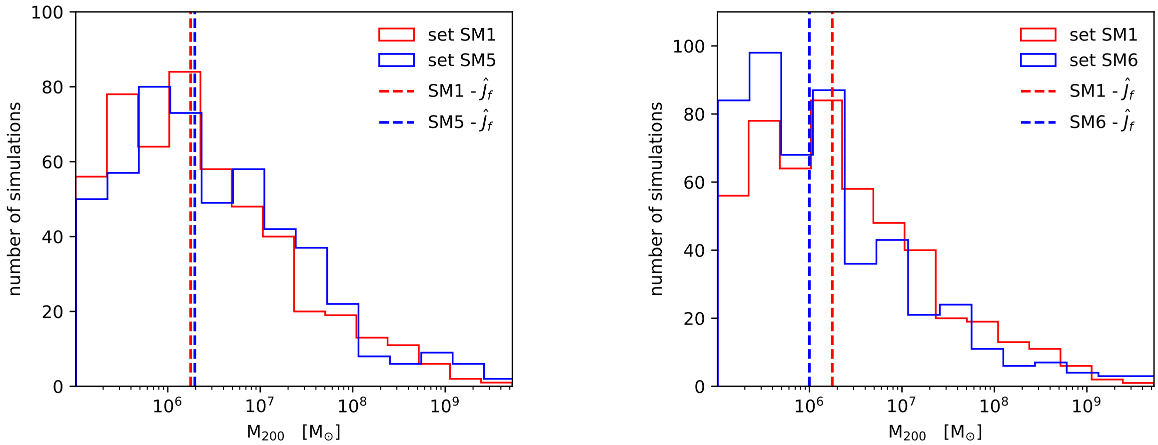

Figure 29 – Left panel: Mass distribution of the 500 brightest sub-halos from models SM1 (red) and SM5 (blue). Each histogram was divided into 15 logarithmic bins from the lower to the higher sub-halo mass in each set. The red (blue) dashed line represents $\widehat{\mathrm{J}}_f$ for model SM1 (SM5). Right panel: Mass distribution of the 500 brightest sub-halos from models SM1 (red) and SM5 (blue). Each histogram was divided into 15 logarithmic bins from the lower to the higher sub-halo mass in each set. Red dashed line represents $\widehat{\mathrm{J}}^i_f$ for model SM1, while blue, for SM6.

Source: By the author

6.2 Simulation of the signal

Given the statistical meaning of the 95 % C. L. J_f, we proceed the calculation of the sources sensitivity curve assuming a gamma-ray flux with J_f = 95 % C. L. u. l. J^i_f and J_f = 95 % C. L. l. l. J^i_f. The location of the source and IRF chosen for this procedure are summarized in table 8. We decide to place the source in both hemispheres to account for a random position of the flux.

Following, we present our results derived using methods for signal *ii)*, described in section 5.2.

6.2.1 $\langle \sigma v \rangle$ in case of detection with the CTA

In this section we present the results of the $\langle \sigma v \rangle \times m_\chi$ phase space if a signal of dark matter is detected by the CTA, calculated by following the methodology *i)* presented in section 5.2.

A summary of the parameters used for this calculation can be seen in table 9.

Figures 30, 32, 34, 36, 38, 40, 42, 44, 46 and 48 present a comparison of the source with J_f = 95 % C. L. u. l. J^i_f, $i = \{1, ..., 11\}$, located in the south (right panel) and north (left panel) hemisphere for the $\tau^+\tau^-$ (red points) and $b\bar{b}$ (black points) annihilation channels. The sensitivity curves were calculated for an observation time of 300 hours. In

Table 7 – Mean properties of sub-halos resolved for each model SM_i $i \in \{1, ..., 10\}$: right ascension ($\widetilde{RA}$), declination ($\widetilde{DEC}$), distance to the observer ($\widetilde{D}_{obs}$), virial mass ($\widetilde{M}_{200}$) and J-factor ($\widetilde{J}_f$). Table also brings the median ($\widehat{J}_f$) maximum (J_f^{max}), lowest (J_f^{min}), 95 % C. L. upper limit (95 % C. L. u. l. J_f^i) and 95 % C. L. lower limit (95 % C. L. l. l. J_f^i) J-factors among the set.

	SM1	SM2	SM3	SM4	SM5	SM6	SM7	SM8	SM9	SM10
$\widetilde{\mathrm{RA}}$ [deg]	195.0	208.1	201.9	208.4	205.4	206.7	206.1	196.6	192.9	190.0
$\widetilde{\mathrm{DEC}}$ [deg]	-6.9	-7.1	-5.2	-6.4	-4.7	-4.5	-7.8	-5.2	-0.3	-5.6
$\widetilde{\mathrm{D}}_{\mathrm{obs}}$ [kpc]	11.1	11.6	10.5	11.0	11.0	11.9	11.0	15.6	29.6	41.9
$\widetilde{M}_{200}$ [$\mathrm{M}_\odot$]	4.6	8.8	6.6	6.0	6.9	7.2	5.9	14.3	12.3	2.2
$\log\left(\frac{J_f}{10^{18}\ \mathrm{GeV}^2/\mathrm{cm}^5}\right)$	8.4	3.8	8.0	13.0	10.1	6.8	20.7	5.0	2.1	0.6
$\log\left(\frac{\widehat{\mathrm{J}}_f}{10^{18}\ \mathrm{GeV}^2/\mathrm{cm}^5}\right)$	5.2	2.5	4.4	5.0	6.3	3.8	9.9	3.1	0.8	0.2
$\log\left(\frac{\mathrm{J}_f^{max}}{10^{20}\ \mathrm{GeV}^2/\mathrm{cm}^5}\right)$	1.4	0.3	1.0	2.4	1.4	2.2	5.5	0.7	0.6	0.6
$\log\left(\frac{\mathrm{J}_f^{min}}{10^{17}\ \mathrm{GeV}^2/\mathrm{cm}^5}\right)$	9.0	2.1	6.7	9.2	8.5	2.9	5.0	4.5	1.0	0.1
$\log\left(\frac{95\%\ \mathrm{u.l.\ C.L.\ J}_f}{10^{19}\ \mathrm{GeV}^2/\mathrm{cm}^5}\right)$	2.2	1.1	2.6	2.9	2.8	1.9	6.8	1.5	0.6	0.2
$\log\left(\frac{95\%\ \mathrm{l.l.\ C.L.\ J}_f}{10^{18}\ \mathrm{GeV}^2/\mathrm{cm}^5}\right)$	1.4	0.8	1.3	1.6	1.8	1.0	2.1	1.1	0.2	0.02

Source: By the author

Table 8 – Properties chosen for the calculation of the sensitivity curve with methods of detection of a signal with the CTA (i) and no detection of signal (ii): the J-factor, right ascension (RA), declination (DEC) and CTA IRF. The values are adopted for all models SM_i.

Site	RA [deg]	DEC [deg]	IRF
South	180	-45	South_z40_5h
North	180	45	North_z40_5h

Source: By the author

the figures, the grey band represents the maximum and minimum values of the thermal $\langle\sigma v\rangle$, according to reference (31).

For all mass points except for $m_\chi = 100.0$ TeV, the $\tau^+\tau^-$ provided the most constrained sensitivity curves. When comparing both hemispheres, the sensitivity curves are essentially equivalent, with ratio reaching less than one order of magnitude.

We present in figures 31, 33, 35, 37, 39, 41, 43, 45, 47 and 49 the TS for each $\langle\sigma v\rangle \times m_\chi$ point used in the calculation of the sensitivity curves.

The results of the sensitivity curves for a source with $J_f = 95$ % C. L. l. l. J_f^i,

Table 9 – Summary of parameters used in the calculation of the source sensitivity curve in case a signal detection with the CTA.

Annihilation channel	$\tau^+\tau^-$, $b\bar{b}$
J_f (GeV^2/cm^5)	95 % C. L. u. l. J_f^i
CTOOLs version	1.6.3
Observation time (hours)	300
Calibration database	prod3b-v2
IRF	South_z40_5h, North_z40_5h
Dark matter mass points (TeV)	0.15, 1.0, 10.0, 100

Source: By the author

$i = \{1, ..., 11\}$ can be found in Appendix B.

Only model SM7 offers the possibility of probing the thermal values of $\langle\sigma v\rangle$ in a small mass range assuming the $\tau^+\tau^-$ at both hemispheres. Model SM7, which provided the highest upper limit of the 95 % C. L. J_f, gives the most constrained sensitivity curves. This was expected since the J-factor was the only term from equation 3.1 that changed according to the analysed model. On the other hand, SM10 provided the least constrained sensitivity curves. When comparing both hemispheres, the highest ratio between a $\langle\sigma v\rangle \times m_\chi$ point for the south and north hemisphere was ~ 1.05, for a source with J_f = 95 % C. L. l. l. J_f^3 and annihilation on the $b\bar{b}$ channel.

Comparing the results provided by the sources with the upper and lower limit of the 95 % C. L. J_f^i, the first presents a sensitivity much more constrained than the former. The ratio between $\langle\sigma v\rangle \times m_\chi$ for the u. l. and l. l. reach up to three orders of magnitude, for the $b\bar{b}$ annihilation channel, at the south hemisphere and for the SM10 model. This highlights that the sensitivity curve is indeed strongly dependent on the J-factor of the source.

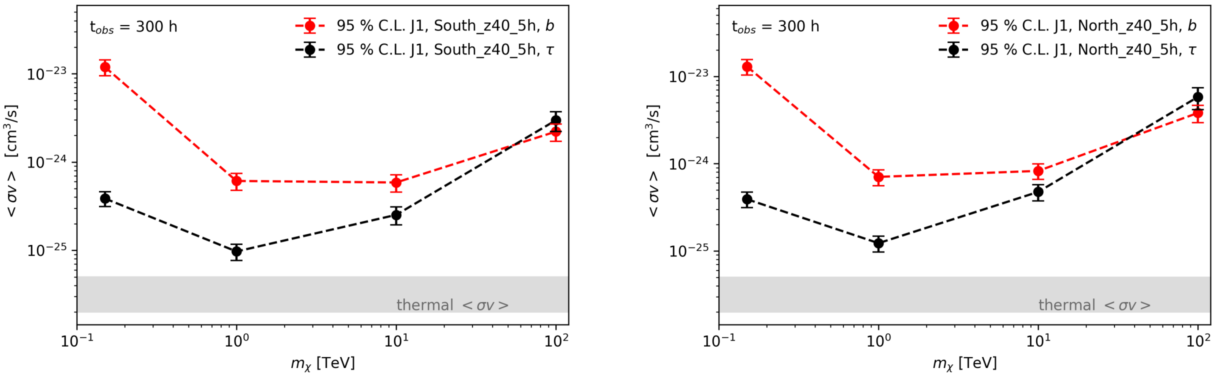

Figure 30 – Left (right) panel: The $\langle \sigma v \rangle$ values for a source with J_f = 95 % C. L. u. l. J1 in the south (north) hemisphere. The red line are the values for $b\bar{b}$, while black, for $\tau^+\tau^-$. The grey band represents the thermal values of $\langle \sigma v \rangle$.

Source: By the author

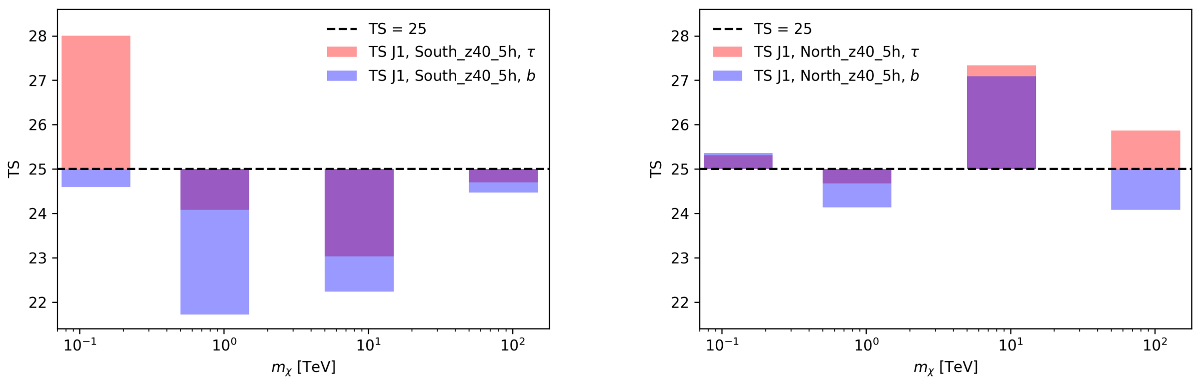

Figure 31 – Left (right) panel: The TS values for model J1 in the south (north) hemisphere. The $\tau^+\tau^-$ values are given in red and $b\bar{b}$ in blue. Source with J_f = 95 % C. L. u. l. J1.

Source: By the author

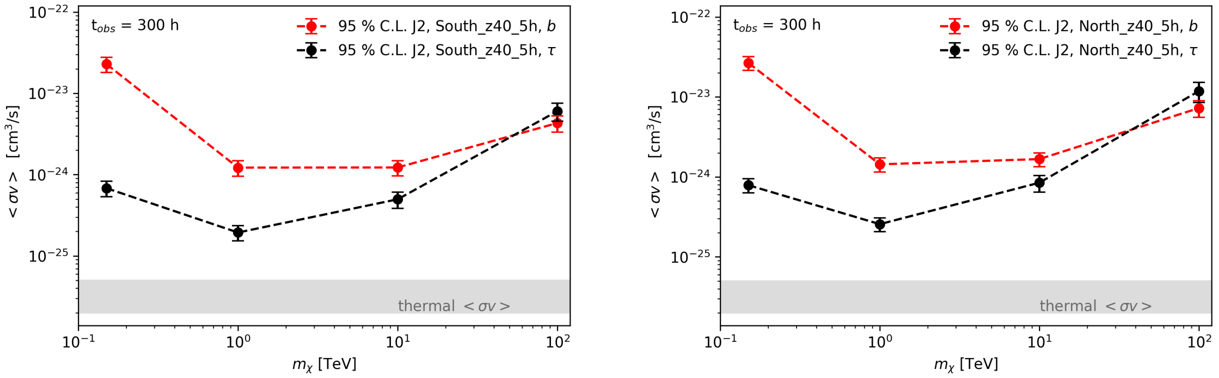

Figure 32 – Left (right) panel: The $\langle\sigma v\rangle$ values for a source with J_f = 95 % C. L. u. l. J2 in the south (north). The red line are the values for $b\bar{b}$, while black, for $\tau^+\tau^-$. The grey band represents the thermal values of $\langle\sigma v\rangle$.

Source: By the author

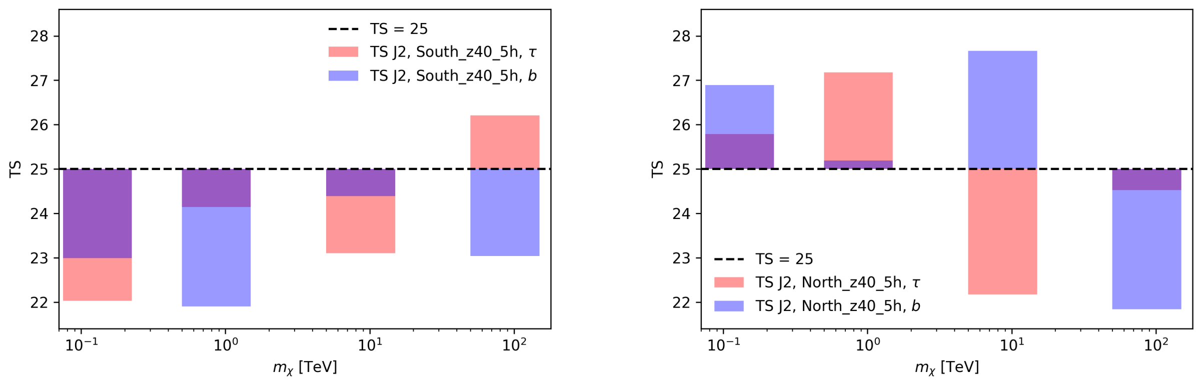

Figure 33 – Left (right) panel: The TS values for model J2 in the south (north) hemisphere. The $\tau^+\tau^-$ values are given in red and $b\bar{b}$ in blue. Source with J_f = 95 % C. L. u. l. J2.

Source: By the author

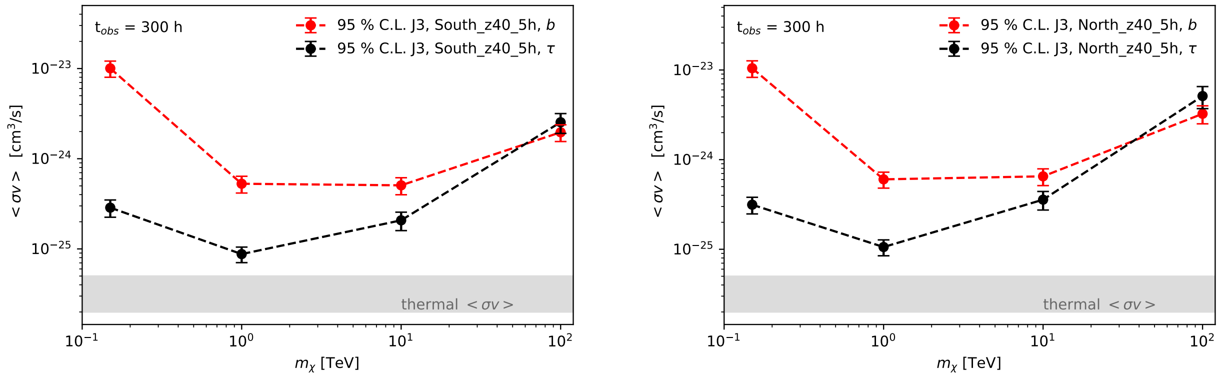

Figure 34 – Left (right) panel: The $\langle \sigma v \rangle$ values for a source with J_f = 95 % C. L. u. l. J3 in the south (north). The red line are the values for $b\bar{b}$, while black, for $\tau^+\tau^-$. The grey band represents the thermal values of $\langle \sigma v \rangle$.

Source: By the author

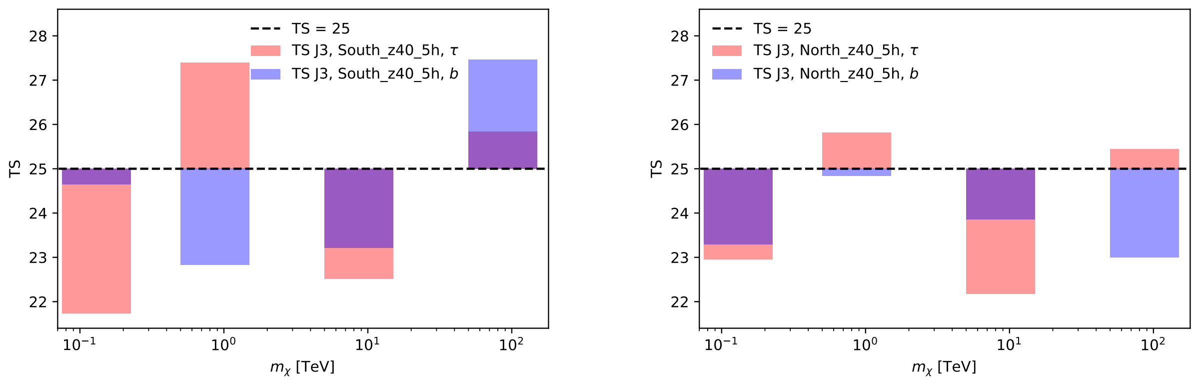

Figure 35 – Left (right) panel: The TS values for model J3 in the south (north) hemisphere. The $\tau^+\tau^-$ values are given in red and $b\bar{b}$ in blue. Source with J_f = 95 % C. L. u. l. J3.

Source: By the author

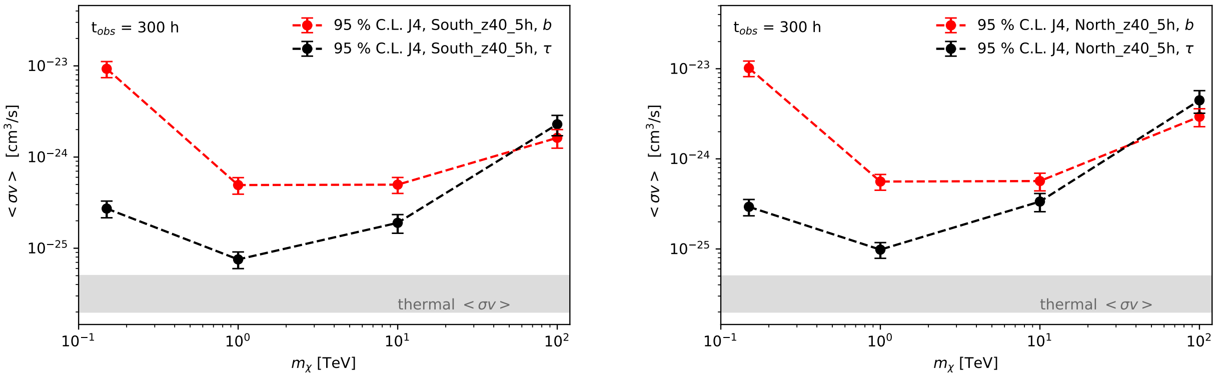

Figure 36 – Left (right) panel: The $\langle \sigma v \rangle$ values for a source with J_f = 95 % C. L. u. l. J4 in the south (north). The red line are the values for $b\bar{b}$, while black, for $\tau^+\tau^-$. The grey band represents the thermal values of $\langle \sigma v \rangle$.

Source: By the author

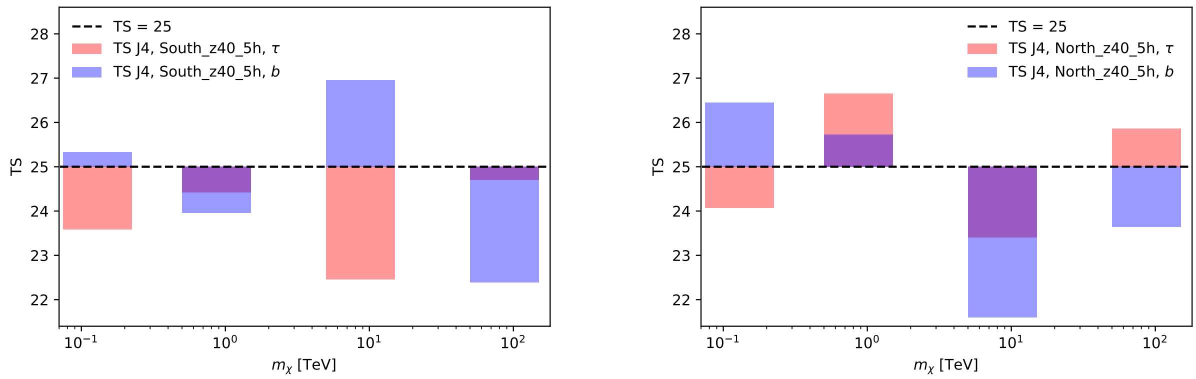

Figure 37 – Left (right) panel: The TS values for model J4 in the south (north) hemisphere. The $\tau^+\tau^-$ values are given in red and $b\bar{b}$ in blue. Source with J_f = 95 % C. L. u. l. J4.

Source: By the author

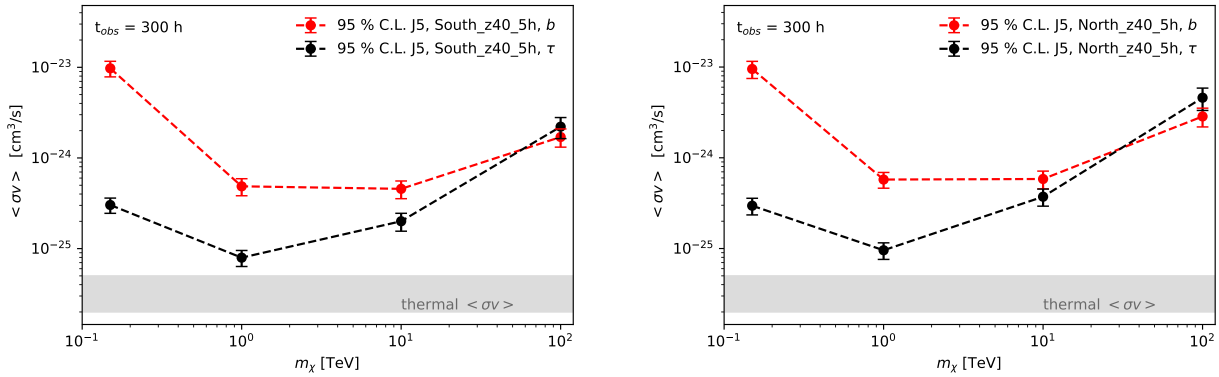

Figure 38 – Left (right) panel: The $\langle \sigma v \rangle$ values for a source with J_f = 95 % C. L. u. l. J5 in the south (north). The red line are the values for $b\bar{b}$, while black, for $\tau^+\tau^-$. The grey band represents the thermal values of $\langle \sigma v \rangle$.

Source: By the author

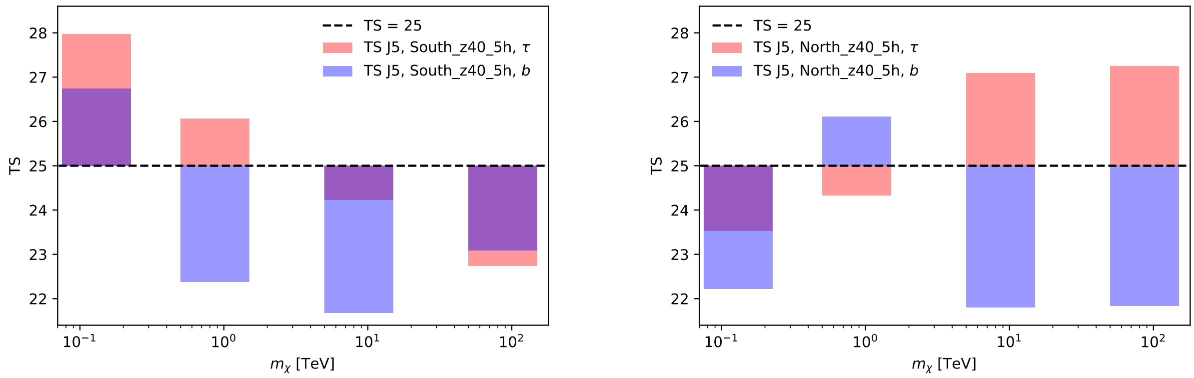

Figure 39 – Left (right) panel: The TS values for model J5 in the south (north) hemisphere. The $\tau^+\tau^-$ values are given in red and $b\bar{b}$ in blue. Source with J_f = 95 % C. L. u. l. J5.

Source: By the author

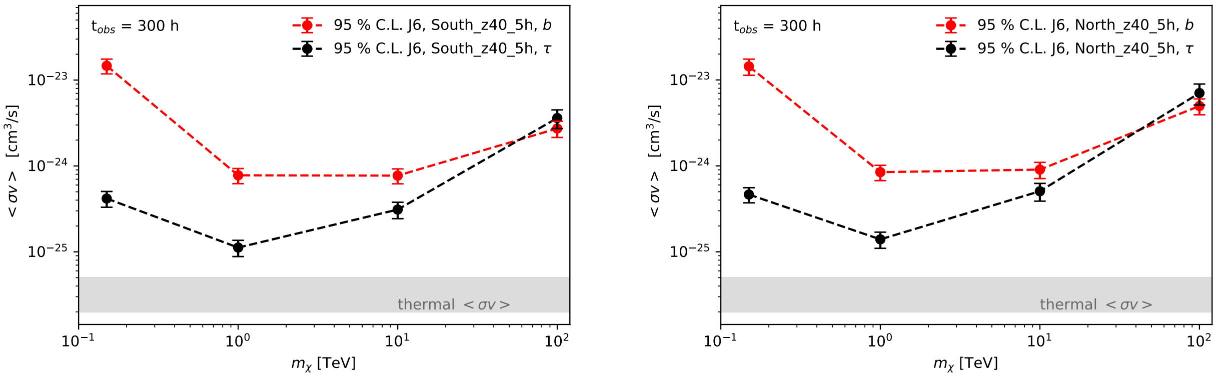

Figure 40 – Left (right) panel: The $\langle \sigma v \rangle$ values for a source with $J_f = 95$ % C. L. u. l. J6 in the south (north). The red line are the values for $b\bar{b}$, while black, for $\tau^+\tau^-$. The grey band represents the thermal values of $\langle \sigma v \rangle$.

Source: By the author

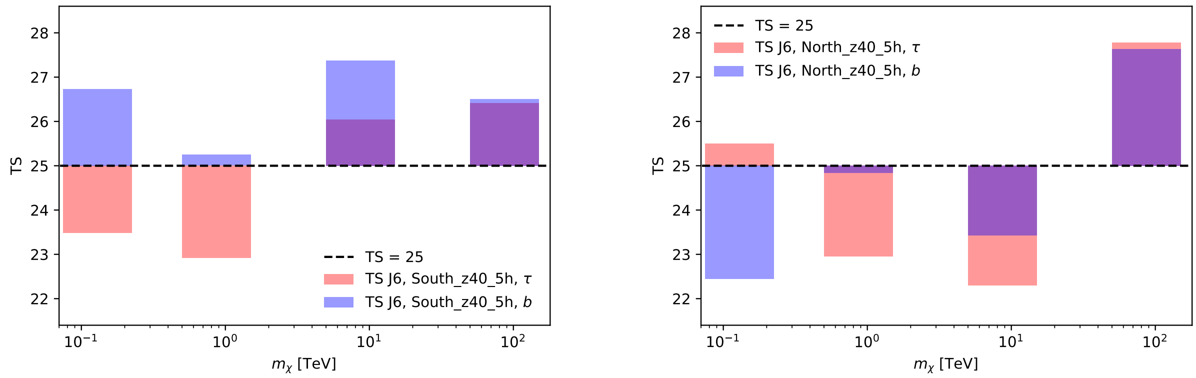

Figure 41 – Left (right) panel: The TS values for model J6 in the south (north) hemisphere. The $\tau^+\tau^-$ values are given in red and $b\bar{b}$ in blue. Source with $J_f = 95$ % C. L. u. l. J6.

Source: By the author

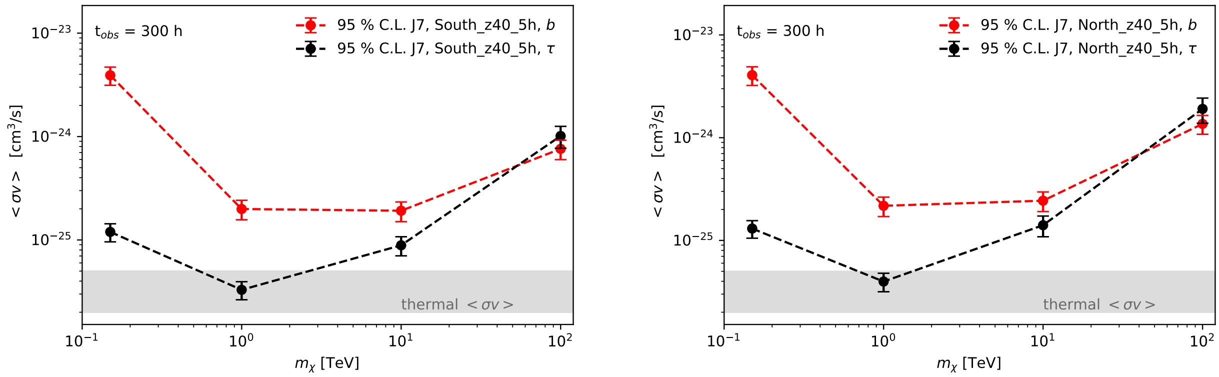

Figure 42 – Left (right) panel: The $\langle \sigma v \rangle$ values for a source with J_f = 95 % C. L. u. l. J7 in the south (north). The red line are the values for $b\bar{b}$, while black, for $\tau^+\tau^-$. The grey band represents the thermal values of $\langle \sigma v \rangle$.

Source: By the author

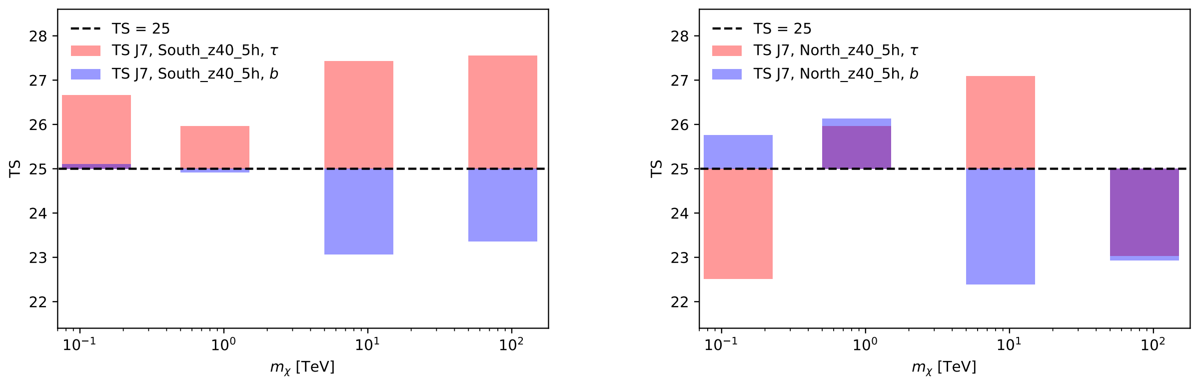

Figure 43 – Left (right) panel: The TS values for model J7 in the south (north) hemisphere. The $\tau^+\tau^-$ values are given in red and $b\bar{b}$ in blue. Source with J_f = 95 % C. L. u. l. J7.

Source: By the author

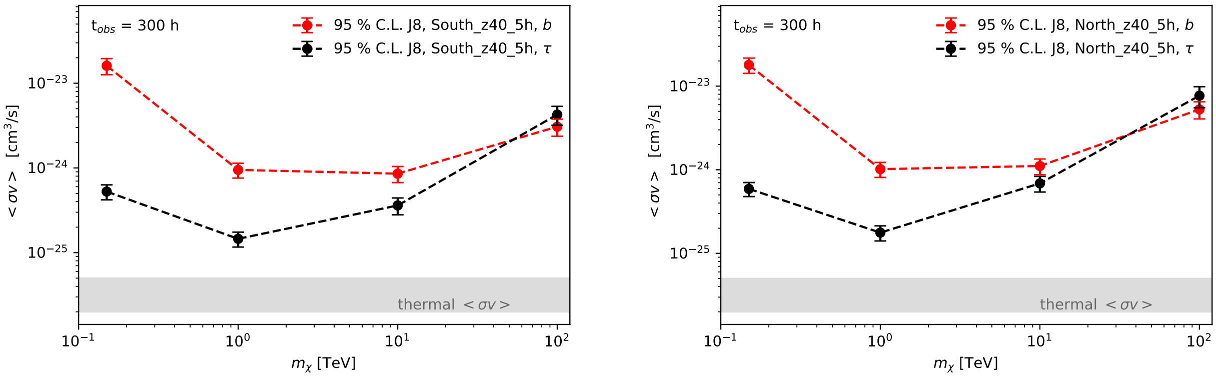

Figure 44 – Left (right) panel: The $\langle \sigma v \rangle$ values for a source with J_f = 95 % C. L. u. l. J8 in the south (north). The red line are the values for $b\bar{b}$, while black, for $\tau^+\tau^-$. The grey band represents the thermal values of $\langle \sigma v \rangle$.

Source: By the author

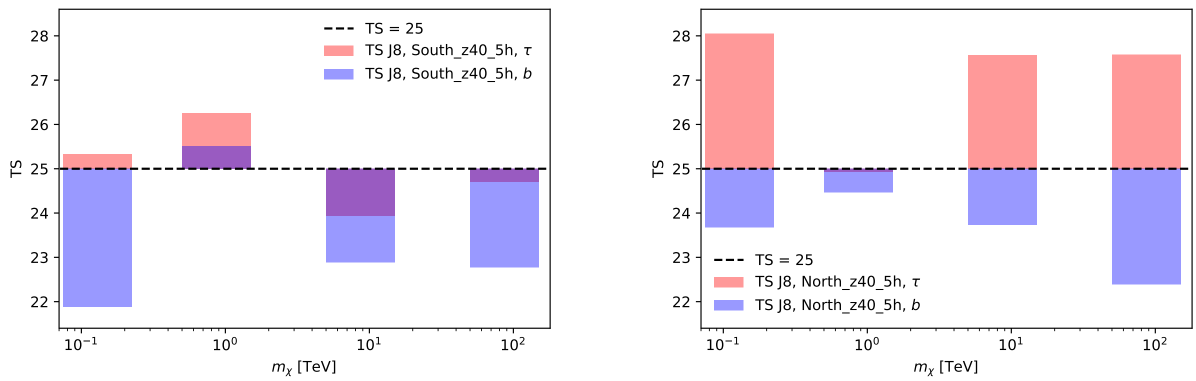

Figure 45 – Left (right) panel: The TS values for model J8 in the south (north) hemisphere. The $\tau^+\tau^-$ values are given in red and $b\bar{b}$ in blue. Source with J_f = 95 % C. L. u. l. J8.

Source: By the author

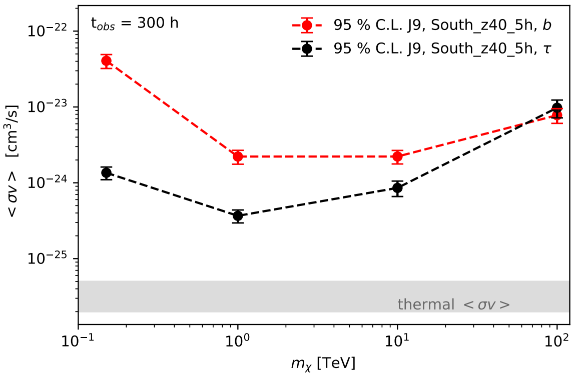

Figure 46 – Left (right) panel: The $\langle \sigma v \rangle$ values for a source with J_f = 95 % C. L. u. l. J9 in the south (north). The red line are the values for $b\bar{b}$, while black, for $\tau^+\tau^-$. The grey band represents the thermal values of $\langle \sigma v \rangle$.

Source: By the author

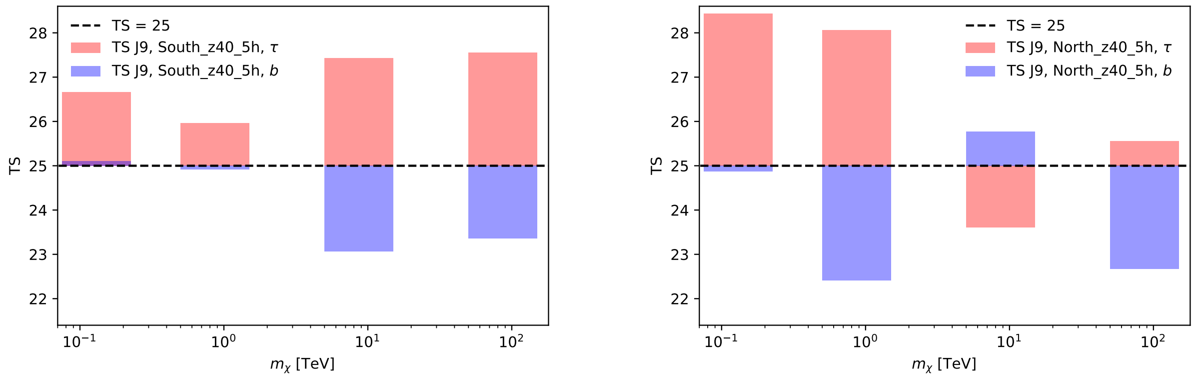

Figure 47 – Left (right) panel: The TS values for model J9 in the south (north) hemisphere. The $\tau^+\tau^-$ values are given in red and $b\bar{b}$ in blue. Source with J_f = 95 % C. L. u. l. J9.

Source: By the author

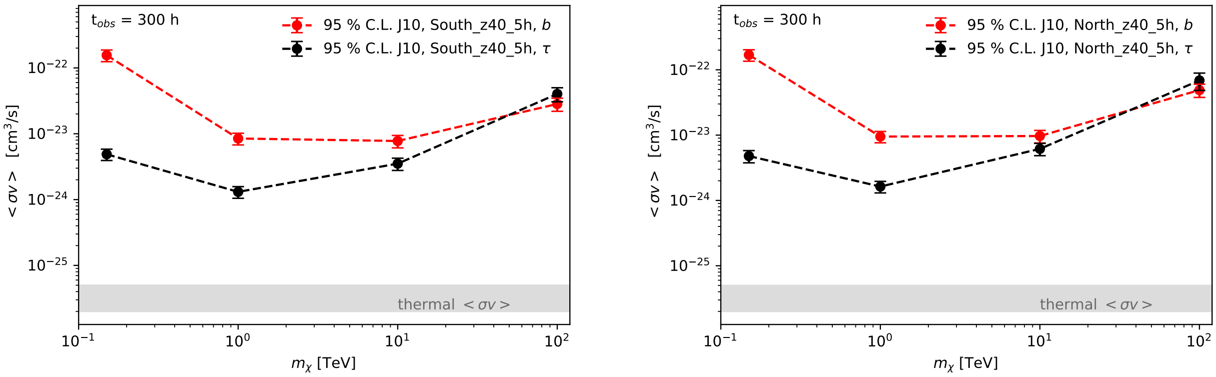

Figure 48 – Left (right) panel: The $\langle \sigma v \rangle$ values for a source with $J_f = 95$ % C. L. u. l. J10 in the south (north). The red line are the values for $b\bar{b}$, while black, for $\tau^+\tau^-$. The grey band represents the thermal values of $\langle \sigma v \rangle$.

Source: By the author

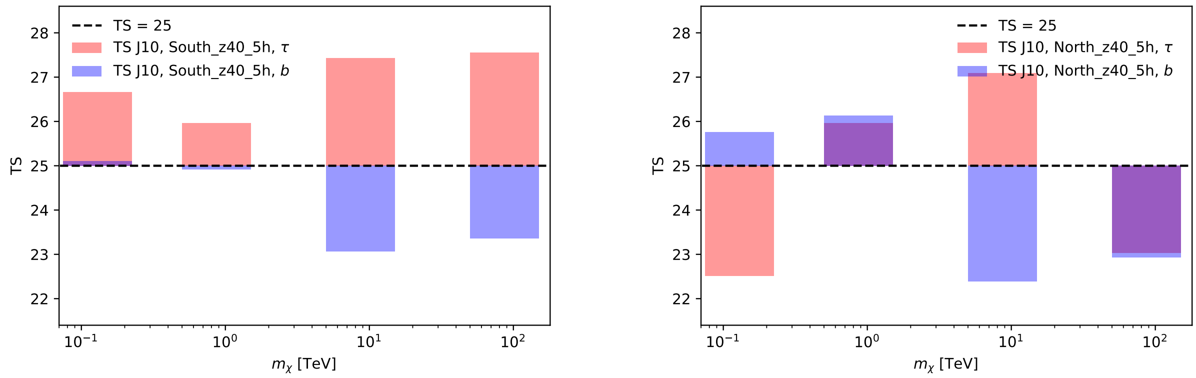

Figure 49 – Left (right) panel: The TS values for model J10 in the south (north) hemisphere. The $\tau^+\tau^-$ values are given in red and $b\bar{b}$ in blue. Source with $J_f = 95$ % C. L. u. l. J10.

Source: By the author

6.2.2 $\langle \sigma v \rangle$ in case of no detection with the CTA

In this section we show the results of the $\langle \sigma v \rangle \times m_\chi$ phase space if no signal of dark matter is detected by the CTA. The sensitivity curves presented here were calculated by following the methodology *ii)* given in section 5.2. A summary of the parameters used in this calculation can be seen in table 10.

Table 10 – Summary of parameters used in the calculation of $\langle \sigma v \rangle \times m_\chi$ via the methodology *ii)* presented in section 5.2.

Annihilation channel	$\tau^+\tau^-$, $b\bar{b}$
J_f (GeV^2/cm^5)	95 % C. L. J_f
$\langle \sigma v \rangle$	10^{-28} cm^3/s
CTOOLs version	1.6.3
Observation time (hours)	300
Calibration database	prod3b-v2
IRF	South_z40_5h, North_z40_5h
Dark matter mass points (TeV)	0.15, 0.5, 1.0, 10.0, 100

Source: By the author

Figures **??** to **??** show the sensitivity curves for a source with J_f = 95 % C. L. u. l. J_f^i (blue points) and J_f = 95 % C. L. l. l. J_f^i (red points). The curves in the top (bottom)-left panel were calculated for a source located in the south hemisphere and $\tau^+\tau^-$ ($b\bar{b}$) channel. In the top (bottom)-right panel, the curves were calculated for the north hemisphere and $\tau^+\tau^-$ ($b\bar{b}$) channel. The green hatched area contains the possible values of sensitivity curves given a J_f contained in the 95 % C. L. interval.

For all models, we calculate the $\langle \sigma v \rangle \times m_\chi$ phase space for an observation time of 300 hours. The grey band represents the possible values of the expected thermal $\langle \sigma v \rangle$, according to figure 10.

As expected, for a source with J_f = 95 % C. L. l. l. J_f^i, the parameter phase space of dark matter is less constrained in respect to a source with J_f = 95 % C. L. u. l. J_f. This is due to the fainter gamma-ray flux produced by a source with lower J-factor. The highest ratio obtained when dividing $\langle \sigma v \rangle \times m_\chi$ for sources with J_f = 95 % C. L. u. l. J_f and J_f = 95 % C. L. l. l. J_f, respectively, was $\sim$ 87, for model SM10, $b\bar{b}$ annihilation channel, for sources placed at the south hemisphere.

When calculating the ratio of the sensitivity curves at the south and and north hemisphere, the highest value obtained was $\sim$ 1.3, for model SM8, annihilation on the $b\bar{b}$ channel and for a source with J_f = 95 % C. L. l. l. J_f^8

By analysing the results, only model SM7 offers the possibility to probe the thermal values of $\langle \sigma v \rangle$ in the case of a source observed by the south or north CTA arrays and for the $\tau^+\tau^-$ annihilation channel.

7 CONCLUSIONS

This work was constructed within the framework of indirect observations of WIMP dark matter by the Cherenkov Telescope Array (CTA). We analysed the sensitivity of CTA to a signal of dark matter originated from Milky Way satellites. Although sub-halos provide a fainter dark matter signal due to their long distance to the Earth, their low astrophysical background places them as promising targets for indirect searches. The present status of known Milky Way satellites, however, is partially incomplete. The number of sub-halos as of August of 2020 stands at 56: 17 discovered by the Sloan Digital Sky Survey SR9 (SDSS) (9), 17 by the Dark Energy Survey (DES) (56, 57), 11 classical dSphs and 11 discovered by other surveys. Because of the limited sky coverage and sensitivity of sky-survey experiments and results of N-body simulations (29, 30), it is believed that this number is much larger.

Using studies that predict the total satellite population of the Milky Way to model the galactic dark matter substructure (51, 58, 71), we resolve dark matter sub-halos with the `CLUMPY` code. This is done by simulating 500 skymaps for 10 different substructure modellings (SM_i, $i \in \{1, \dots, 10\}$) with the following varying parameters: the substructure inner dark matter profile (19, 20), its mass (29, 30) and radial (51, 58, 71) distribution around the Milky Way, the expected number of satellites (51, 58, 71) provided by different studies and the mass-concentration relation. (87, 88)

For each model we assess the properties of the average population of the dark matter-brightest sub-halos. We also present the distribution of the J-factors from sources. We show that the change in in the mass-concentration parameter relation according to reference (88) gives the highest median of the source J-factor. On the other hand, the substructure modelling according to reference (58), and assuming the lower limit for the number of sub-halos expected by the same study, produced the lowest median of the source J-factor.

We proceed the analysis by calculating the upper (u. l.) and lower limits (l. l.) of the 95 % C. L. J-factor (J_f) interval estimated over the 500 brightest sub-halos from each model. Assuming sources with such J_f, we calculate the gamma-ray flux originated from dark matter annihilation into the $\tau^+\tau^-$ and $b\bar{b}$ channels. This flux was used to estimate the source sensitivity curve, i.e., the parameter space given by the velocity averaged cross-section by the dark matter mass, $\langle \sigma v \rangle \times m_\chi$.

In this step we assume two main cases: when there is a detection of a dark matter signal with the CTA and when there is not. In the first, we can calculate the true value of $\langle \sigma v \rangle$ for annihilating dark matter. Here, the value of $\langle \sigma v \rangle$ is associated with an intrinsic significance, reflected as the value of the test statistics. In the second case, we are only able to estimate the $\langle \sigma v \rangle$ upper limit.

For each dark matter substructure modelling we determine the sensitivity curve for annihilation into the $\tau^+\tau^-$ and $b\bar{b}$ channels, for sources placed at the north (RA = 45°, DEC = 180°) and south (RA = -45°, DEC = 180°) hemispheres. We assume that the sub-halos have J-factors given by the upper and lower limit of the 95 % C. L. J$_f$ interval calculated over the 500 brightest sub-halos in each model. As expected, the model with the highest median of the J-factor also gave the more constrained sensitivity curves and was the only one to access the thermal values of $\langle \sigma v \rangle$ in case of no signal detection with the CTA and in case of signal detection. We demonstrate that the $\tau^+\tau^-$ channel essentially gave the most constrained sensitivity curves. We show that the parameter space for the north and south hemisphere are roughly equivalent.

REFERENCES

1 AGHANIM, N. *et al.* Planck 2018 results. VI. Cosmological parameters. 2018. Available from: https://arxiv.org/abs/1807.06209. Accessible at: 11 Aug. 2020.

2 ZWICKY, F. English and Spanish Translation of Zwicky's (1933) the redshift of extragalactic nebulae. 2017. Available from: https://arxiv.org/abs/1711.01693. Accessible at: 11 Aug. 2020.

3 RUBIN, V. C.; FORD W. KENT, J. Rotation of the andromeda nebula from a spectroscopic survey of emission regions. **Astrophysical Journal**, v. 159, p. 379, 1970. Available from: https://ui.adsabs.harvard.edu/abs/1970ApJ...159..379R. Accessible at: 11 Aug. 2020.

4 RUBIN, V. C. Radial velocities of distant OB stars in the anticenter region of the galaxy. **Astrophysical Journal**, v. 142, p. 934, 1965. Available from: https://ui.adsabs.harvard.edu/abs/1965ApJ...142..934R. Accessible at: 11 Aug. 2020.

5 QUEIROZ, F. **WIMP theory review**, 2017. Available from: https://arxiv.org/abs/1711.02463. Accessible at: 11 Aug. 2020.

6 GASKINS, J. A review of indirect searches for particle dark matter. **Contemporary Physics**, v. 57, n. 3, 2016. Available from: https://arxiv.org/abs/1604.00014. Accessible at: 11 Aug. 2020.

7 GIANFRANCO, B. **Particle dark matter**: observations, models and searches. Cambridge: Cambridge University Press, 2010.

8 ABBOTT, T. M. C. *et al.* Dark energy survey year 1 results: cosmological constraints from galaxy clustering and weak lensing. **Physical Review D**, v. 98, p. 043526, 2018. Available from: https://link.aps.org/doi/10.1103/PhysRevD.98.043526. Accessible at: 11 Aug. 2020.

9 GUNN, J. E.; WEINBERG, D. H. The sloan digital sky survey. 1994. Available from: https://arxiv.org/abs/astro-ph/9412080. Accessible at: 11 Aug. 2020.

10 THE CTA COLLABORATION. **Science with the Cherenkov Telescope Array**, 2017. Available from: https://arxiv.org/abs/1709.07997. Accessible at: 11 Aug. 2020.

11 BEGEMAN, K. G.; BROEILS, A. H.; SANDERS, R. H. Extended rotation curves of spiral galaxies : dark haloes and modified dynamics. **Monthly Notices of the Royal Astronomy Society**, v. 249, p. 523–537, 1991. Available from: http://articles.adsabs.harvard.edu/pdf/1991MNRAS.249..523B. Accessible at: 11 Aug. 2020.

12 IOCCO, F.; PATO, M.; BERTONE, G. Evidence for dark matter in the inner Milky Way. **Nature Physics**, v. 11, n. 3, p. 245–248, 2015. Available from: https://arxiv.org/abs/1502.03821. Accessible at: 11 Aug. 2020.

13 **The Wilkinson Microwave Anisotropy Probe**, 2011. Available from: https://wmap.gsfc.nasa.gov/media/101080/. Accessible at: 11 Aug. 2020.

14 ESA AND THE PLANCK COLLABORATION. The European Space Agency. 2013. Available from: https://www.esa.int/ESAMultimedia/Images/2013/03/PlanckPowerSpectrum. Accessible at: 11 Aug. 2020.

15 LONGAIR, M. **High energy astrophysics:** an introduction. 3rd ed. Cambridge: Cambridge University Press, 2011.

16 SCHNEIDER, P. **Extragalactic astronomy and cosmology**: an introduction. 2nd ed. Berlin, Heidelberg: Springer-Verlag, 2015.

17 CLOWE, D.; BRADAC, M.; GONZALEZ, A.; MARKEVITCH, M.; RANDALL, S. W.; JONES, C.; ZARITSKY, D. A direct empirical proof of the existence of dark matter. **Astrophysical Journal**, v. 648, n. 2, p. 109–113, 2006. Available from: https://arxiv.org/abs/astro-ph/0608407. Accessible at: 11 Aug. 2020.

18 DUBINSKI, J.; CARLBERG, R. G. The structure of cold dark matter halos. **Astrophysical Journal**, v. 378, p. 496–503, 1991. Available from: https://ui.adsabs.harvard.edu/abs/1991ApJ...378..496D/abstract. Accessible at: 11 Aug. 2020.

19 NAVARRO, J.; FRENK, C.; WHITE, S. The structure of cold dark matter halos. **Astrophysical Journal**, v. 462, p. 563–575, 1995. Available from: https://arxiv.org/abs/astro-ph/9508025. Accessible at: 11 Aug. 2020.

20 LUDLOW, A. D.; ANGULO, R. E. Einasto profiles and the dark matter power spectrum. **Monthly Notices of the Royal Astronomy Society**, v. 465, n. 1, p. 84–88, 2017. Available from: https://arxiv.org/abs/1610.04620. Accessible at: 11 Aug. 2020.

21 BURKERT, A. **The Structure of Dark Matter Halos. Observation versus Theory**. 1997. Available from: https://ui.adsabs.harvard.edu/abs/1997dmap.conf...35B. Accessible at: 11 Aug. 2020.

22 BEGEMAN, K.; BROEILS, A.; SANDERS, R. Extended rotation curves of spiral galaxies: dark haloes and modified dynamics. **Monthly Notices of the Royal Astronomy Society**, v. 249, p. 523–537, 1991. Available from: https://inspirehep.net/literature/331140. Accessible at: 11 Aug. 2020.

23 CIRELLI, M. *et al.* PPPC 4 DM ID: a poor particle physicist cookbook for dark matter indirect detection. **Journal of Cosmology and Astroparticle Physics**, v. 2011, n. 3, p. 051, 2011. Available from: https://ui.adsabs.harvard.edu/abs/2011JCAP...03..051C. Accessible at: 11 Aug. 2020.

24 XUE, X-X. *et al.* The Milky Way's circular velocity curve to 60 kpc and an estimate of the dark matter halo mass from the kinematics of 2400 SDSS blue horizontal-branch stars. **Astrophysical Journal**, v. 684, p. 1143–1158, 2008. Available from: https://arxiv.org/abs/0801.1232. Accessible at: 11 Aug. 2020.

25 GILLESSEN, S. *et al.* Monitoring stellar orbits around the massive black hole in the galactic center. **Astrophysical Journal**, v. 692, n. 10, 2008. Available from: https://arxiv.org/abs/0810.4674. Accessible at: 11 Aug. 2020.

26 GRIEST, K.; KAMIONKOWSKI, M. Supersymmetric dark matter. **Physics Reports**, v. 333-334, p. 167–182, 2000. DOI: 1016/S0370-1573(00)00021-1.

27 READ, J. The local dark matter density. **Journal of Physics G**, v. 41, n. 6, p. 063101, 2014.

28 DIEMER, B.; KRAVTSOV, A. V. A universal model for halo concentrations. **Astrophysical Journal**, v. 799, n. 1, p. 108, 2015.

29 SPRINGEL, V. *et al.* The Aquarius project: the subhaloes of galactic haloes. **Monthly Notices of the Royal Astronomical Society**, v. 391, n. 4, p. 1685–1711, 2008.

30 GARRISON-KIMMEL, S.; BOYLAN-KOLCHIN, M.; BULLOCK, J.; LEE, K. ELVIS: exploring the local colume in simulations. **Monthly Notices of the Royal Astronomy Society**, v. 438, n. 3, p. 2578–2596, 2014.

31 STEIGMAN, G.; DASGUPTA, B.; BEACOM, J. F. Precise relic WIMP abundance and its impact on searches for dark matter annihilation. **Physical Review D**, v. 86, p. 023506, 2012. Available from: https://link.aps.org/doi/10.1103/PhysRevD.86.023506. Accessible at: 11 Aug. 2020.

32 GRIEST, K. The search for the dark matter: WIMPs and MACHOs. **Annals of the New York Academy of Sciences**, v. 688, n. 1, p. 390–407, 1993.

33 DINE, M. Particle astrophysics from the particle perspective. **AIP Conference Proceedings**, v. 302, n. 1, p. 695, 1994.

34 BI PENG-FEI YIN, Q. Y. X.-J. Status of dark matter detection. **Frontiers of Physics**, v. 8, n. 6, p. 794, 2013.

35 THE COSINE-100 COLLABORATION. An experiment to search for dark-matter interactions using sodium iodide detectors. **Nature**, v. 564, p. 83–86, 2018. DOI: 10.1038/s41586-018-0739-1.

36 ANGELIS, A. D.; GALANTI, G.; RONCADELLI, M. Transparency of the Universe to gamma rays. **Monthly Notices of the Royal Astronomy Society**, v. 432, p. 3245–3249, 2013.

37 THE FERMI-LAT COLLABORATION. **The FERMI-LAT website**. Available from: https://www.nasa.gov/content/fermi-gamma-ray-space-telescope. Accessible at: 18 Aug. 2020.

38 THE MAGIC COLLABORATION. **The MAGIC Collaboration website**. Available from: http://www.magic.iac.es/. Accessible at: 11 Aug. 2020.

39 THE H.E.S.S. COLLABORATION. **The H.E.S.S. Collaboration website**. Available from: https://www.mpi-hd.mpg.de/hfm/HESS/. Accessible at: 11 Aug. 2020.

40 THE CTA COLLABORATION. **The CTA Collaboration website**. Available from: https://www.cta-observatory.org/. Accessible at: 11 Aug. 2020.

41 HECK, D.; PIEROG, T. **Extensive air shower simulation with CORSIKA**: a user's guide (version 7.100 from december 17, 2019). Available from: https://web.ikp.kit.edu/corsika/usersguide/usersguide.pdf. Accessible at: 11 Jul. 2020.

42 SCIUTTO, S. **The AIRES system for air shower simulations. An update**. 2001. Available from: https://arxiv.org/abs/astro-ph/0106044. Accessible at: 2 Sep. 2020.

43 DE ANGELIS, A.; PIMENTA, M. **Introduction to particle and astroparticle physics**: multimessenger astronomy and its particle physics foundations. 2nd ed. Cambridge: Springer International Publishing, 2018.

44 THE ICECUBE COLLABORATION. **The IceCube website**. Available from: https://icecube.wisc.edu/. Accessible at: 11 Aug. 2020.

45 THE AMS-02 COLLABORATION. **The AMS-02 website**. Available from: https://ams02.space/. Accessible at: 11 Aug. 2020.

46 THE PAMELA EXPERIMENT COLLABORATION. **The PAMELA experiment website**. Available from: https://pamela-web.web.roma2.infn.it/. Accessible at: 11 Aug. 2020.

47 CONRAD, J.; REIMER, O. Indirect dark matter searches in gamma- and cosmic rays. **Nature Physics**, v. 13, p. 224–231, 2017. Available from: https://arxiv.org/abs/1705.11165. Accessible at: 11 Aug. 2020.

48 DEIL, C. *et al.* **Gammapy - A prototype for the CTA science tools**, 2017. Available from: https://arxiv.org/abs/1709.01751. Accessible at: 11 Aug. 2020.

49 OLIVE, K. A. t. Review of particle physics. **Chinese Physics**, C38, p. 090001, 2014. DOI: 10.1088/1674-1137/38/9/090001.

50 RINCHIUSO, L. *et al.* **Dark matter gamma-ray line searches toward the Galactic Center halo with H.E.S.S. I**. 2017. Available from: https://arxiv.org/abs/1708.08358. Accessible at: 11 Aug. 2020.

51 NEWTON, O.; CAUTUN, M.; JENKINS, A.; FRENK, C. S.; HELLY, J. C. The Milky Way's total satellite population and constraining the mass of the warm dark matter particle. **Proceedings of the International Astronomical Union**, v. 14, n. S344, p. 109–113, 2018. Available from: https://arxiv.org/abs/1708.04247. Accessible at: 11 Aug. 2020.

52 SIMON, J. et al. Stellar kinematics and metallicities in the ultra-faint dwarf galaxy reticulum ii. **The Astrophysical Journal**, v. 808, p. 95, 04 2015. DOI: 10.1088/0004-637X/808/1/95.

53 BONNIVARD, V. *et al.* Spherical Jeans analysis for dark matter indirect detection in dwarf spheroidal galaxies - impact of physical parameters and triaxiality. **Monthly Notices of the Royal Astronomical Society**, v. 446, n. 3, p. 3002–3021, 2015.

54 BONNIVARD, V.; COMBET, C.; MAURIN, D.; WALKER, M. **Dark matter annihilation and decay factors in the Milky Way's dwarf spheroidal galaxies**. 2016. Available from: https://inspirehep.net/literature/1483458. Accessible at: 11 Aug. 2020.

55 GENINA, A.; FAIRBAIRN, M. The potential of the dwarf galaxy Triangulum II for dark matter indirect detection. **Monthly Notices of the Royal Astronomical Society**, v. 463, n. 4, p. 3630–3636, 2016. Available from: https://arxiv.org/abs/1604.00838. Accessible at: 11 Aug. 2020.

56 KOPOSOV, S. *et al.* Beasts of the southern wild: discovery of nine ultra faint satellites in the vicinity of the magellanic clouds. **Astrophysical Journal**, v. 805, n. 2, p. 130, 2015.

57 THE DES COLLABORATION. Eight new Milky Way companions discovered in first-year Dark Energy Survey data. **Astrophysical Journal**, v. 807, n. 1, p. 50, 2015. Available from: https://ui.adsabs.harvard.edu/abs/2015ApJ...807...50B. Accessible at: 11 Aug. 2020.

58 KIM, S. Y.; PETER, A. H. G.; HARGIS, J. R. Missing satellites problem: completeness corrections to the number of satellite galaxies in the Milky Way are consistent with cold dark matter predictions. **Physical Review Letters**, v. 121, p. 211302, 2018. Available from: https://link.aps.org/doi/10.1103/PhysRevLett.121.211302. Accessible at: 11 Aug. 2020.

59 BROUGH, S. *et al.* The Vera Rubin observatory legacy survey of space and time and the low surface brightness universe. **Proceedings IAU Symposium**, n. 355, 2020. Available from: https://arxiv.org/abs/2001.11067. Accessible at: 11 Aug. 2020.

60 SAWALA, T. *et al.* The chosen few: the low-mass haloes that host faint galaxies. **Monthly Notices of the Royal Astronomical Society**, v. 456, n. 1, p. 85–97, 2015.

61 WALSH, S. M.; WILLMAN, B.; JERJEN, H. The invisibles: a detection algorithm to trace the faintest Milky Way satellites. **Astrophysical Journal**, v. 137, n. 1, p. 450–469, 2009. Available from: https://ui.adsabs.harvard.edu/abs/2009AJ....137..450W. Accessible at: 11 Aug. 2020.

62 JETHWA, P.; ERKAL, D.; BELOKUROV, V. A magellanic origin of the DES dwarfs. **Monthly Notices of the Royal Astronomical Society**, v. 461, n. 2, p. 2212–2233, 2016.

63 THE SDSS COLLABORATION. The eighth data release of the sloan digital sky survey: first data from SDSS-III. **Astrophysical Journal Supplement Series**, v. 193, p. 29, 2011. Available from: https://arxiv.org/abs/1101.1559. Accessible at: 11 Aug. 2020.

64 BOVILL, M. S.; RICOTTI, M. Where are the fossils of the first galaxies? Local volume maps and properties of the undetected dwarfs. **Astrophysical Journal**, v. 741, n. 1, p. 17, 2011. Available from: https://doi.org/10.1088%2F0004-637x%2F741%2F1%2F17. Accessible at: 11 Aug. 2020.

65 BROWN, T. *et al.* The primeval populations of the ultra-faint dwarf galaxies. **Astrophysical Journal Letters**, v. 753, 2012. DOI: 10.1088/2041-8205/753/1/L21.

66 SAND, D. *et al.* A deeper look at Leo IV: star formation history and extended structure. **Astrophysical Journal**, v. 718, p. 530, 2010.

67 WEISZ, D. R. *et al.* The star formation histories of the local group dwarf galaxies. II. searching for signatures of reionization. **Astrophysical Journal**, v. 789, n. 2, p. 148, 2014. Available from: https://arxiv.org/abs/1405.3281. Accessible at: 11 Aug. 2020.

68 MU*n*OZ, R.; GEHA, M.; WILLMAN, B. Turning the tides on the ultra-faint dwarf spheroidal galaxies: Coma Berenices and Ursa Major II. **The Astronomical Journal**, v. 140, p. 138, 2009. Available from: https://arxiv.org/abs/0910.3946. Accessible at: 11 Aug. 2020.

69 WILLMAN, B. *et al.* Willman 1-A probable dwarf galaxy with an irregular kinematic distribution. **The Astronomical Journal**, v. 142, p. 128, 2011. Available from: https://arxiv.org/abs/1007.3499. Accessible at: 11 Aug. 2020.

70 SAND, D. *et al.* Tidal signatures in the faintest Milky Way satellites: The detailed properties of Leo V, Pisces II and Canes Venatici II. **Astrophysical Journal**, v. 756, p. 79, 2011. DOI: 10.1088/0004-637X/756/1/79.

71 KOPOSOV, S. *et al.* The luminosity function of the Milky Way satellites. **Astrophysical Journal**, v. 686, p. 279, 2008. Available from: https://arxiv.org/abs/0706.2687. Accessible at: 11 Aug. 2020.

72 THE SDSS COLLABORATION. The fifth data release of the sloan digital sky survey. **Astrophysical Journal Supplement Series**, v. 172, n. 2, p. 634–644, 2007. Available from: https://arxiv.org/abs/0707.3380. Accessible at: 11 Aug. 2020.

73 AHARONIAN, F.; HEINZELMANN, G. The HEGRA experiment status and recent results. **Nuclear Physics B** - proceedings supplements, v. 60, n. 3, p. 193 – 198, 1998. ISSN 0920-5632. Available from: http://www.sciencedirect.com/science/article/pii/S0920563297005148. Accessible at: 11 Aug. 2020.

74 MORI, M. CANGAROO project for high-energy gamma-ray astrophysics. **Progress of Theoretical Physics Supplement**, v. 151, p. 85–94, 2003. Available from: https://academic.oup.com/ptps/article/doi/10.1143/PTPS.151.85/1838535. Accessible at: 11 Aug. 2020.

75 THE VERITAS COLLABORATION. **The VERITAS Collaboration website**. Available from: https://veritas.sao.arizona.edu/. Accessible at: 11 Aug. 2020.

76 ORAMAS, A. L. **Multi-year Campaign of the Gamma-Ray Binary LS I +61°303and Search for VHE Emission from Gamma-Ray Binary Candidates with the MAGIC Telescopes.** 2014. 230 f. Ph. D. Thesis (Doctor in Physics) — Universitat Autònoma de Barcelona, Barcelona, 2014.

77 GRIEDER, P. K. F. **Extensive air showers**: high energy phenomena and astrophysical aspects - a tutorial, reference manual and data book. Berlin: Springer-Verlag, 2010.

78 RANDO, N. *et al.* **Status of the ESA L1 mission candidate ATHENA**. 2012. DOI: 10.1117/12.924820.

79 THE E-Astrogam COLLABORATION. Science with e-ASTROGAM. a space mission for mev-gev gamma-ray astrophysics. **Journal of High Energy Astrophysics**, v. 19, p. 1–106, 2018. Available from: https://ui.adsabs.harvard.edu/abs/2018JHEAp..19....1D/abstract. Accessible at: 11 Aug. 2020.

80 MCENERY, J.; AMEGO TEAM. All Sky Medium Energy Gamma-ray Observatory (AMEGO): exploring the extreme multimessenger universe. 2020. Available from: https://arxiv.org/abs/1907.07558. Accessible at: 11 Aug. 2020.

81 PRETZ, J.; the HAWC COLLABORATION. **Highlights from the High Altitude Water Cherenkov Observatory**. 2015. Available from: https://arxiv.org/pdf/1509.07851.pdf. Accessible at: 11 Aug. 2020.

82 SCIASCIO, G. D.; THE LHAASO COLLABORATION. The LHAASO experiment: from gamma-ray astronomy to cosmic rays. **Nuclear Physics B** - proceedings supplement, v. 279-281, p. 166–173, 2016. Available from: https://arxiv.org/abs/1602.07600. Accessible at: 11 Aug. 2020.

83 TLUCZYKONT, M *et al.* The HiSCORE experiment and its potential for gamma-ray astronomy. **Journal of Physics Conference Series**, v. 409, p. 012120, 2013. Available from: https://iopscience.iop.org/article/10.1088/1742-6596/409/1/012120/pdf. Accessible at: 11 Aug. 2020.

84 HÜTTEN, M.; COMBET, C.; MAURIN, D. CLUMPY v3: γ-ray and ν signals from dark matter at all scales. **Computer Physics Communications**, v. 235, p. 336–345, 2019. Available from: https://ui.adsabs.harvard.edu/abs/2019CoPhC.235..336H. Accessible at: 11 Aug. 2020.

85 CHARBONNIER, A.; COMBET, C.; MAURIN, D. CLUMPY: A code for γ-ray signals from dark matter structures. **Computer Physics Communications**, v. 183, n. 3, p. 656–668, 2012. Available from: https://ui.adsabs.harvard.edu/abs/2012CoPhC.183..656C. Accessible at: 11 Aug. 2020.

86 HÜTTEN, M.; COMBET, C.; MAIER, G.; MAURIN, D. Dark matter substructure modelling and sensitivity of the Cherenkov Telescope Array to Galactic dark halos. **Journal of Cosmology and Astroparticle Physics**, v. 09, p. 047, 2016. Available from: https://arxiv.org/abs/1606.04898. Accessible at: 11 Aug. 2020.

87 MOLINÉ, Á.; SÁNCHEZ-CONDE, M. A.; PALOMARES-RUIZ, S.; PRADA, F. Characterization of subhalo structural properties and implications for dark matter annihilation signals. **Monthly Notices of the Royal Astronomical Society**, v. 466, n. 4, p. 4974–4990, 2017.

88 PIERI, L.; LAVALLE, J.; BERTONE, G.; BRANCHINI, E. Implications of high-resolution simulations on indirect dark matter searches. **Physical Review D**, v. 83, n. 2, p. 023518, 2011. Available from: https://arxiv.org/abs/0908.0195. Accessible at: 11 Aug. 2020.

89 BULLOCK, J. S.; KOLATT, T. S.; SIGAD, Y.; SOMERVILLE, R. S.; KRAVTSOV, A. V.; KLYPIN, A. A.; PRIMACK, J. R.; DEKEL, A. Profiles of dark haloes: evolution, scatter and environment. **Monthly Notices of the Royal Astronomical Society**, v. 321, n. 3, p. 559–575, 2001.

90 KUHLEN, M.; MADAU, P.; SILK, J. Exploring dark matter with Milky Way substructure. **Science**, v. 325, n. 5943, p. 970, 2009. Available from: https://ui.adsabs.harvard.edu/abs/2009Sci...325..970K. Accessible at: 11 Aug. 2020.

91 THE CTA COLLABORATION. **The CTOOLs website**. Available from: http://cta.irap.omp.eu/ctools/index.html. Accessible at: 11 Aug. 2020.

92 KNÖDLSEDER, J. *et al.* GammaLib and ctools. a software framework for the analysis of astronomical gamma-ray data. **Astronomy & Astrophysics**, v. 593, p. A1, 2016. Available from: https://arxiv.org/abs/1606.00393. Accessible at: 11 Aug. 2020.

93 THE NASA-HEASARC TEAM. **The High Energy Astrophysics Science Archive Research Center (HEASARC) website**. Available from: https://heasarc.gsfc.nasa.gov/. Accessible at: 11 Aug. 2020.

94 WILKS, S. S. The large-sample distribution of the likelihood ratio for testing composite hypotheses. **Annals of Mathematical Statistics**, v. 9, n. 1, p. 60–62, 1938. Available from: https://inspirehep.net/literature/1247197. Accessible at: 11 Aug. 2020.

95 LEVENBERG, K. A method for the solution of certain non-linear problems in least squares. **Quarterly of Applied Mathematics**, v. 2, n. 2, p. 164–168, 1944. Available from: https://www.jstor.org/stable/43633451?seq=1. Accessible at: 19 Aug. 2020.

Appendix

APPENDIX A – THE DISTRIBUTION OF J_f SIMULATED WITH THE CLUMPY CODE

The distribution of the 500 highest J_f^i, from models SM_i $i \in \{1, ..., 10\}$, is shown in figure 50. Each histogram was divided in 15 logarithmic bins from the lowest to the highest J_f^i. The black-dashed lines represent the 95 % C. L. upper (u. l.) and lower limits (l. l.) of J_f^i, calculated over the sample.

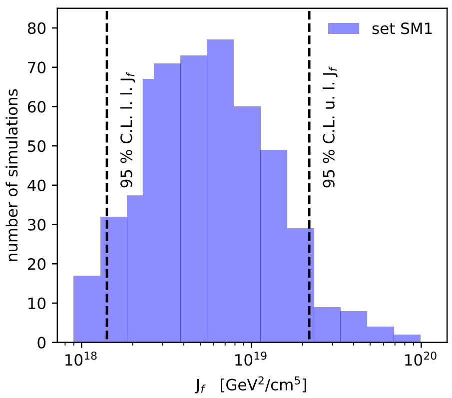

(a) Distribution of J_f^1.

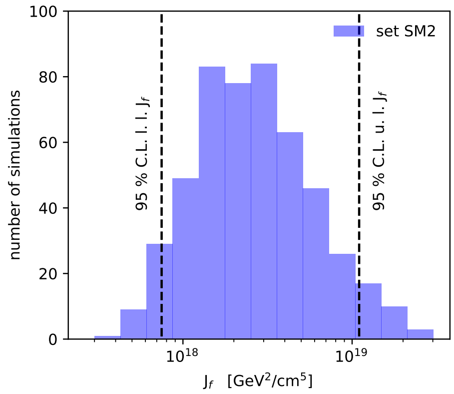

(b) Distribution of J_f^2.

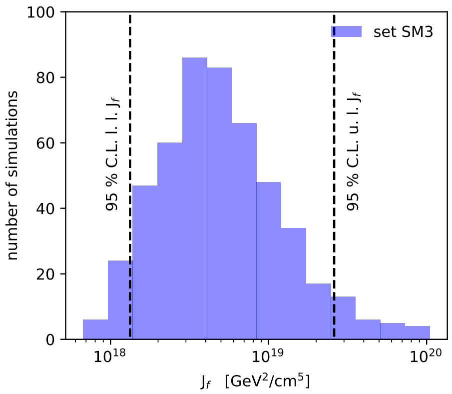

(c) Distribution of J_f^3.

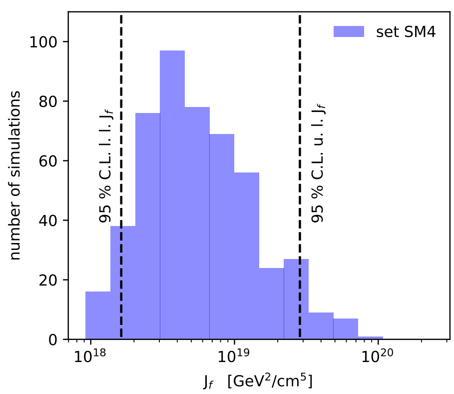

(d) Distribution of J_f^4.

continues

continuation

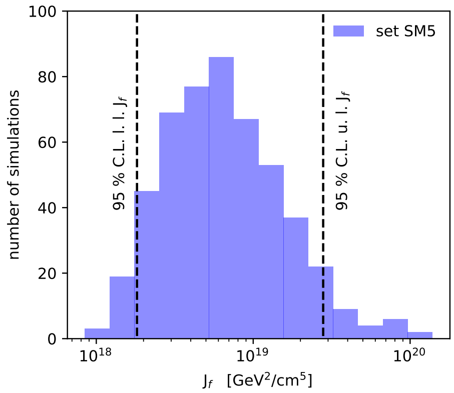

(e) Distribution of J_f^5.

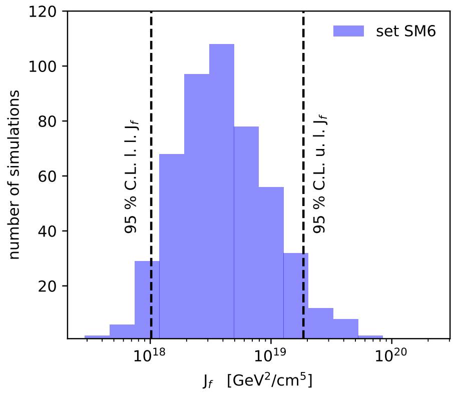

(f) Distribution of J_f^6.

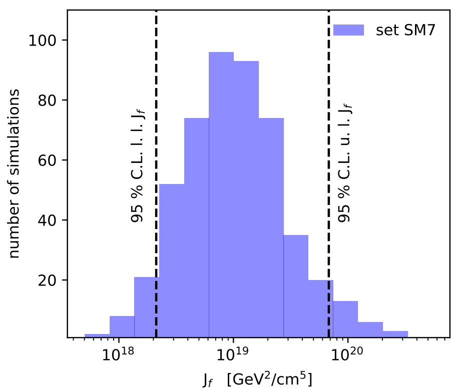

(g) Distribution of J_f^7.

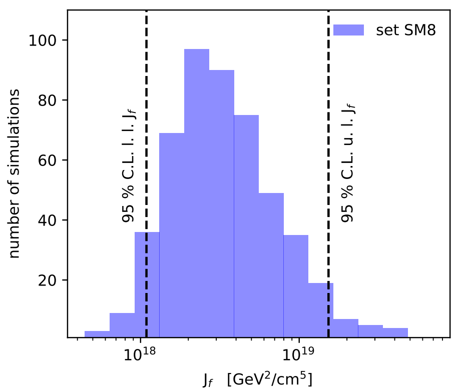

(h) Distribution of J_f^8.

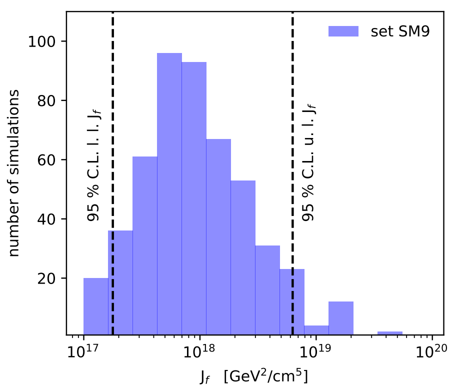

(i) Distribution of J_f^9.

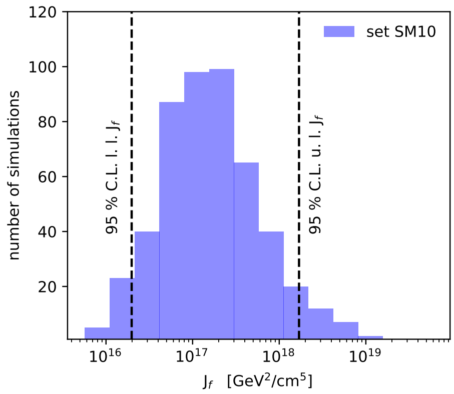

(j) Distribution of J_f^{10}.

Figure 50 – Distribution of J_f for the 500 brightest in dark matter sub-halos resolved for each model presented in table 6.

Source: By the author

APPENDIX B – THE $\langle \sigma v \rangle \times m_\chi$ IN THE CASE OF DETECTION WITH THE CTA FOR A SOURCE WITH 95 % C.L. L. L. J_f

Figures 51, 53, 55, 57, 59, 61, 63, 65, 67 and 69 present a comparison of the source with J_f = 95 % C.L. l. l. J_f^i, $i = \{1, ..., 11\}$, located in the south (right panel) and north (left panel) hemisphere for the $\tau^+\tau^-$ (red points) and $b\bar{b}$ (black points) annihilation channels. The sensitivity curves were calculated for an observation time of 300 hours. In the figures, the grey band represents the maximum and minimum values of the thermal $\langle \sigma v \rangle$, according to reference (31). A summary of the properties used in the calculation of the sensitivity curves can be seen in table 11.

Given that the 95 % C.L. l. l. J_f is by default lower than the 95 % C.L. u. l. J_f, the sensitivity curves are less constrained in comparison with the later.

The TS for each $\langle \sigma v \rangle \times m_\chi$ point in each sensitivity curve is presented in figures 31, 33, 35, 37, 39, 41, 43, 45, 47 and 49.

Table 11 – Summary of parameters used in the calculation of the source sensitivity curve in case a signal detection with the CTA.

Annihilation channel	$\tau^+\tau^-$, $b\bar{b}$
J_f ($\mathrm{GeV}^2/\mathrm{cm}^5$)	95 % C. L. l. l. J_f^i
CTOOLs version	1.6.3
Observation time (hours)	300
Calibration database	prod3b-v2
IRF	South_z40_5h, North_z40_5h
Dark matter mass points (TeV)	0.15, 1.0, 10.0, 100

Source: By the author

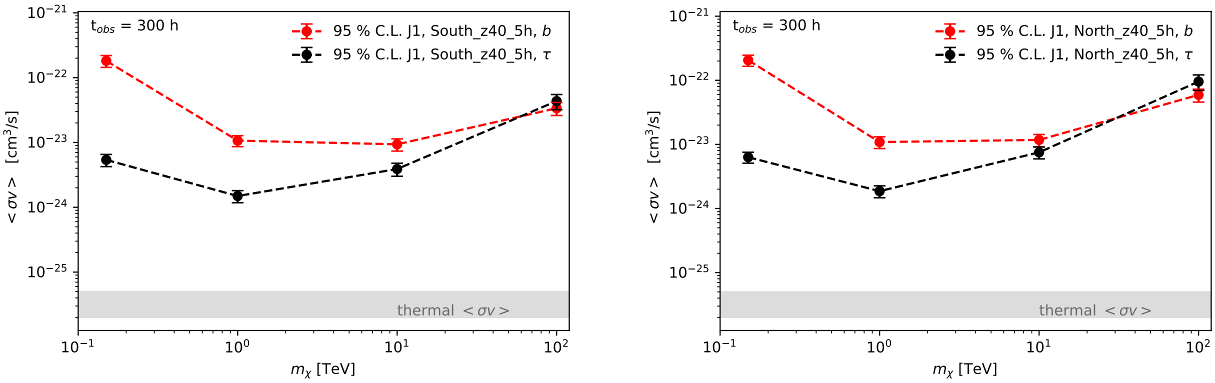

Figure 51 – Left (right) panel: The $\langle \sigma v \rangle$ values for a source with J_f = 95 % C.L. l. l. J1 in the south (north). The red line are the values for $b\bar{b}$, while black, for $\tau^+\tau^-$. The grey band represents the thermal values of $\langle \sigma v \rangle$.

Source: By the author

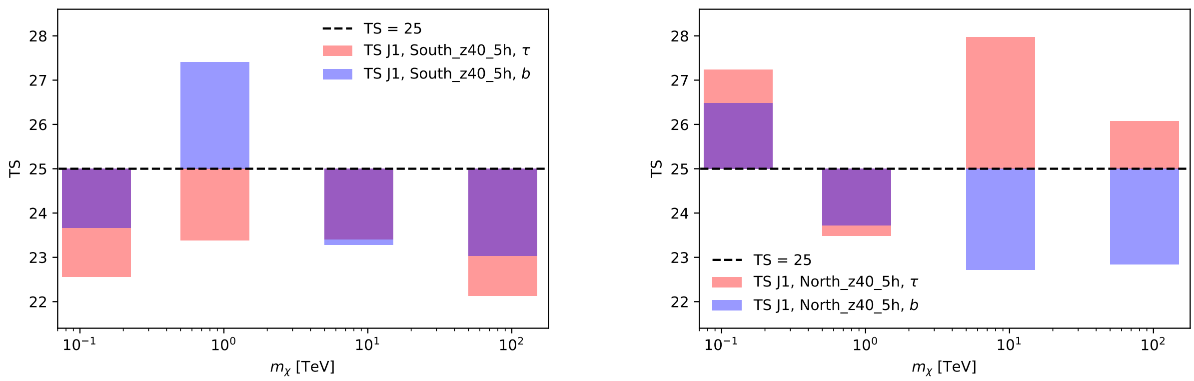

Figure 52 – Left (right) panel: The TS values for model J1 in the south (north) hemisphere. The $\tau^+\tau^-$ values are given in red and $b\bar{b}$ in blue. Source with J_f = 95 % C.L. l. l. J1.

Source: By the author

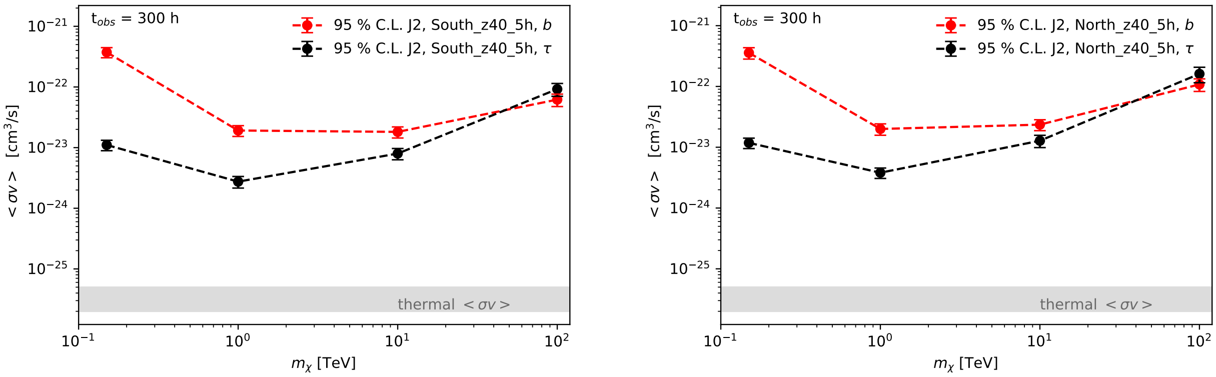

Figure 53 – Left (right) panel: The $\langle \sigma v \rangle$ values for a source with J_f = 95 % C.L. l. l. J2 in the south (north). The red line are the values for $b\bar{b}$, while black, for $\tau^+\tau^-$. The grey band represents the thermal values of $\langle \sigma v \rangle$.

Source: By the author

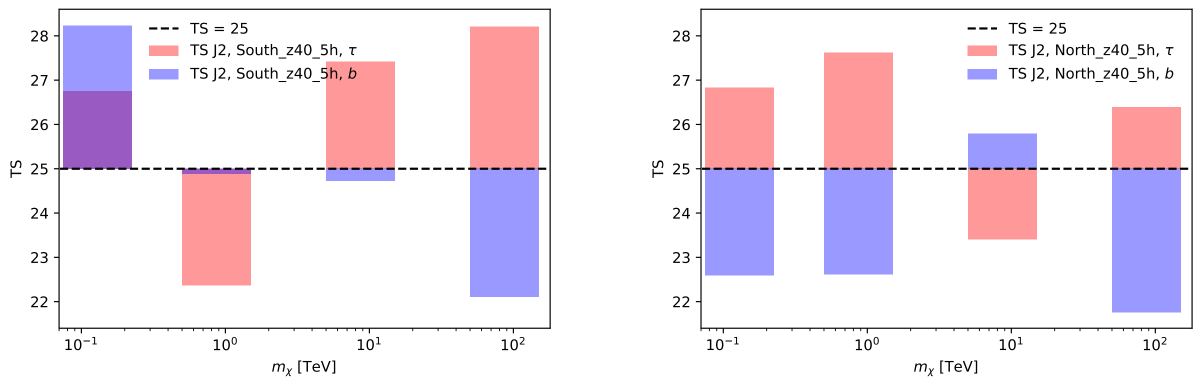

Figure 54 – Left (right) panel: The TS values for model J2 in the south (north) hemisphere. The $\tau^+\tau^-$ values are given in red and $b\bar{b}$ in blue. Source with J_f = 95 % C.L. l. l. J2.

Source: By the author

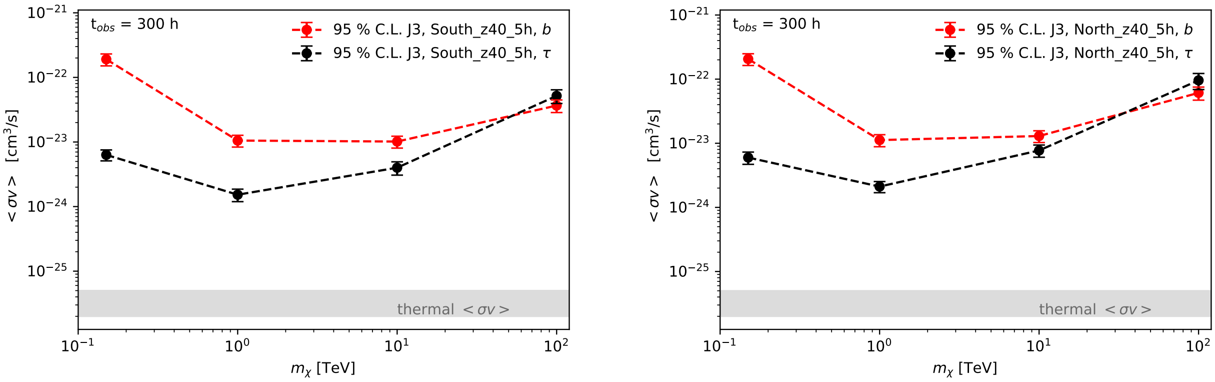

Figure 55 – Left (right) panel: The $\langle\sigma v\rangle$ values for a source with J_f = 95 % C.L. l. l. J3 in the south (north). The red line are the values for $b\bar{b}$, while black, for $\tau^+\tau^-$. The grey band represents the thermal values of $\langle\sigma v\rangle$.

Source: By the author

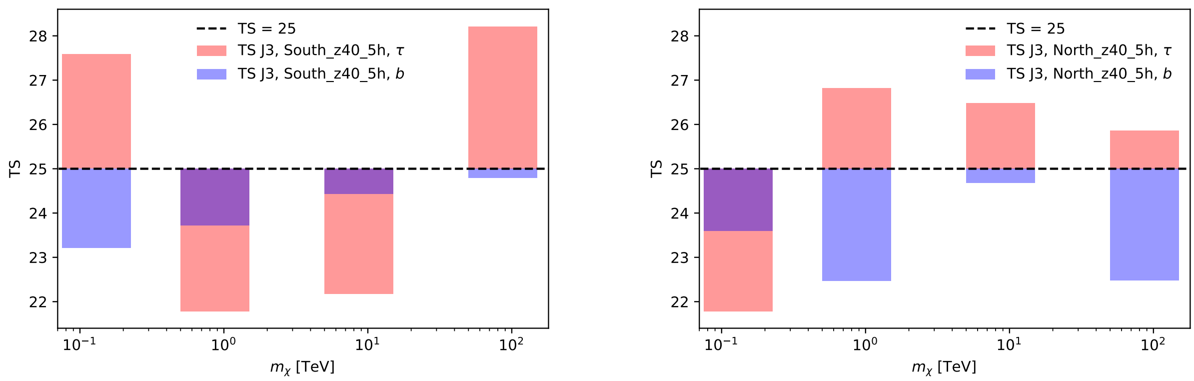

Figure 56 – Left (right) panel: The TS values for model J3 in the south (north) hemisphere. The $\tau^+\tau^-$ values are given in red and $b\bar{b}$ in blue. Source with J_f = 95 % C.L. l. l. J3.

Source: By the author

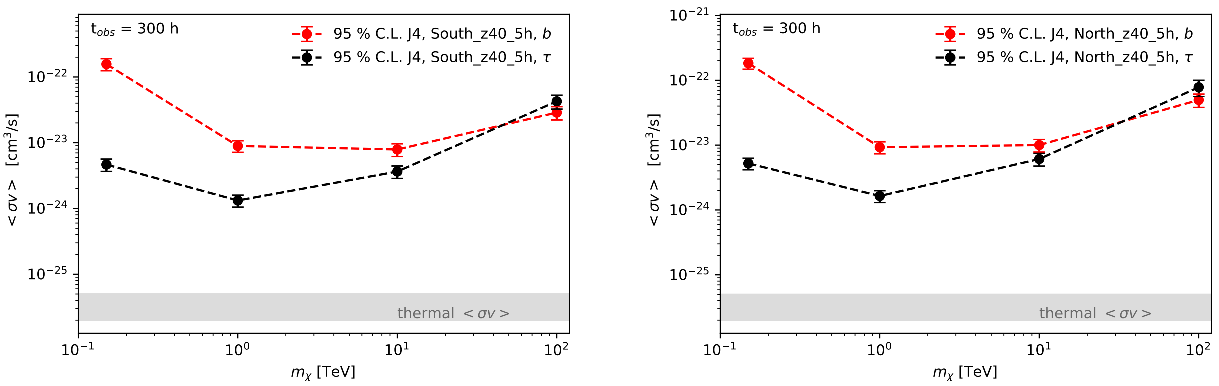

Figure 57 – Left (right) panel: The $\langle \sigma v \rangle$ values for a source with J_f = 95 % C.L. l. l. J4 in the south (north). The red line are the values for $b\bar{b}$, while black, for $\tau^+\tau^-$. The grey band represents the thermal values of $\langle \sigma v \rangle$.

Source: By the author

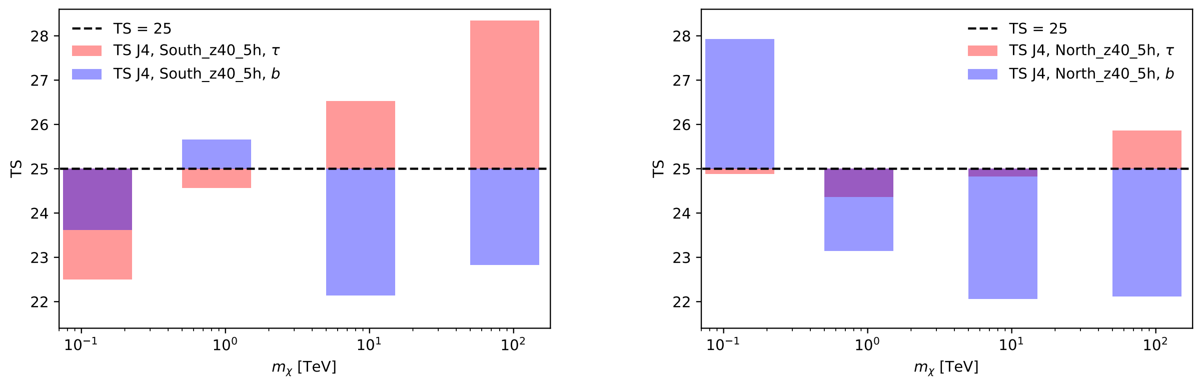

Figure 58 – Left (right) panel: The TS values for model J4 in the south (north) hemisphere. The $\tau^+\tau^-$ values are given in red and $b\bar{b}$ in blue. Source with J_f = 95 % C.L. l. l. J4.

Source: By the author

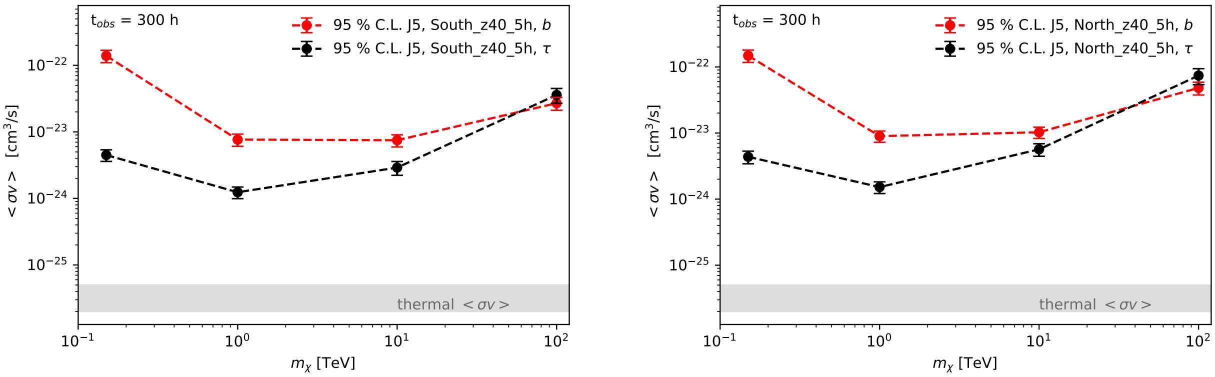

Figure 59 – Left (right) panel: The $\langle\sigma v\rangle$ values for a source with J_f = 95 % C.L. l. l. J5 in the south (north). The red line are the values for $b\bar{b}$, while black, for $\tau^+\tau^-$. The grey band represents the thermal values of $\langle\sigma v\rangle$.

Source: By the author

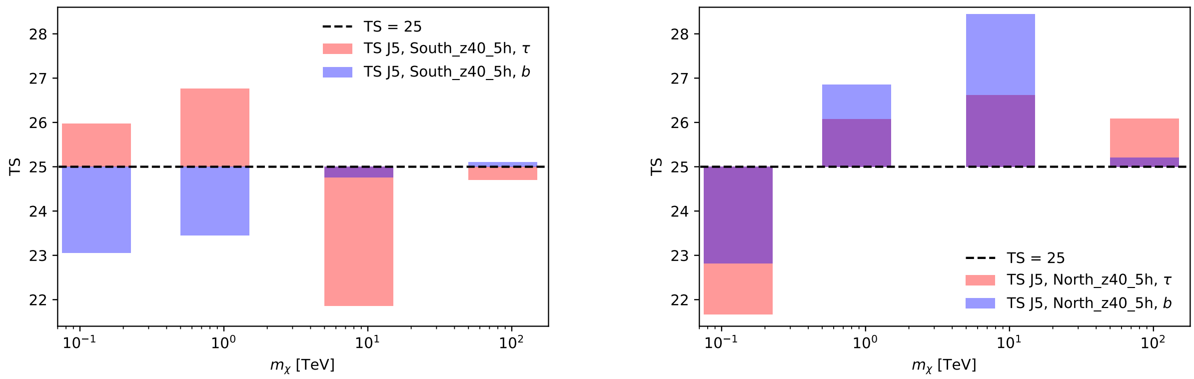

Figure 60 – Left (right) panel: The TS values for model J5 in the south (north) hemisphere. The $\tau^+\tau^-$ values are given in red and $b\bar{b}$ in blue. Source with J_f = 95 % C.L. l. l. J5.

Source: By the author

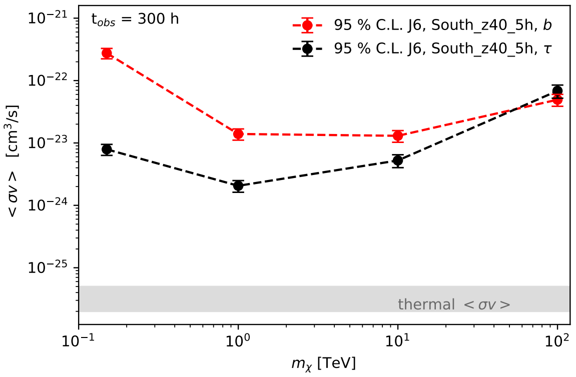

Figure 61 – Left (right) panel: The $\langle \sigma v \rangle$ values for a source with J_f = 95 % C.L. l. l. J6 in the south (north). The red line are the values for $b\bar{b}$, while black, for $\tau^+\tau^-$. The grey band represents the thermal values of $\langle \sigma v \rangle$.

Source: By the author

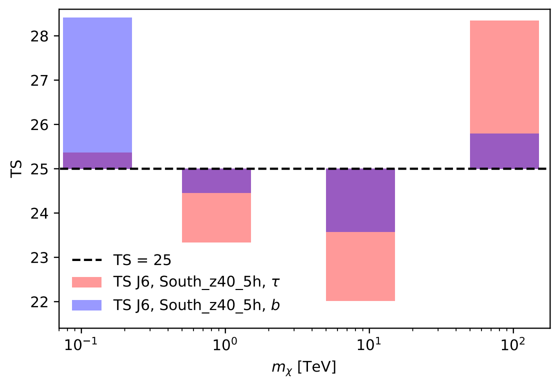

Figure 62 – Left (right) panel: The TS values for model J6 in the south (north) hemisphere. The $\tau^+\tau^-$ values are given in red and $b\bar{b}$ in blue. Source with J_f = 95 % C.L. l. l. J6.

Source: By the author

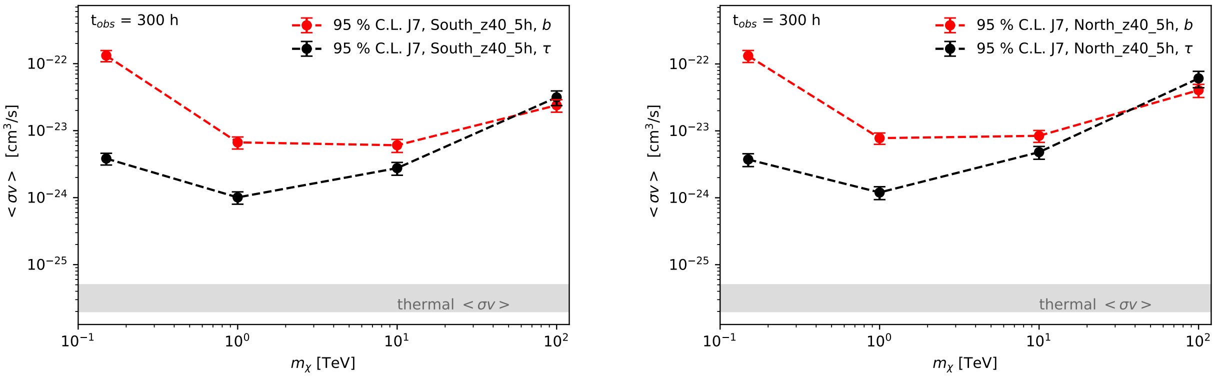

Figure 63 – Left (right) panel: The $\langle \sigma v \rangle$ values for a source with J_f = 95 % C.L. l. l. J7 in the south (north). The red line are the values for $b\bar{b}$, while black, for $\tau^+\tau^-$. The grey band represents the thermal values of $\langle \sigma v \rangle$.

Source: By the author

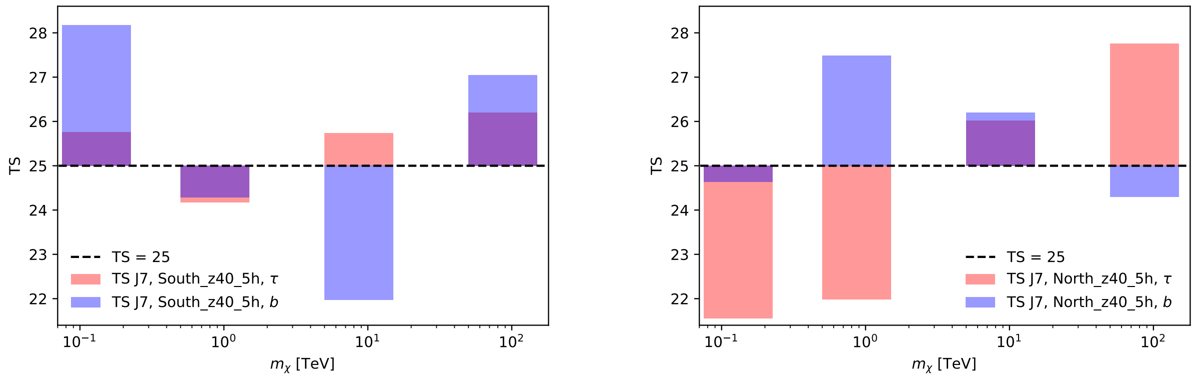

Figure 64 – Left (right) panel: The TS values for model J7 in the south (north) hemisphere. The $\tau^+\tau^-$ values are given in red and $b\bar{b}$ in blue. Source with J_f = 95 % C.L. l. l. J7.

Source: By the author

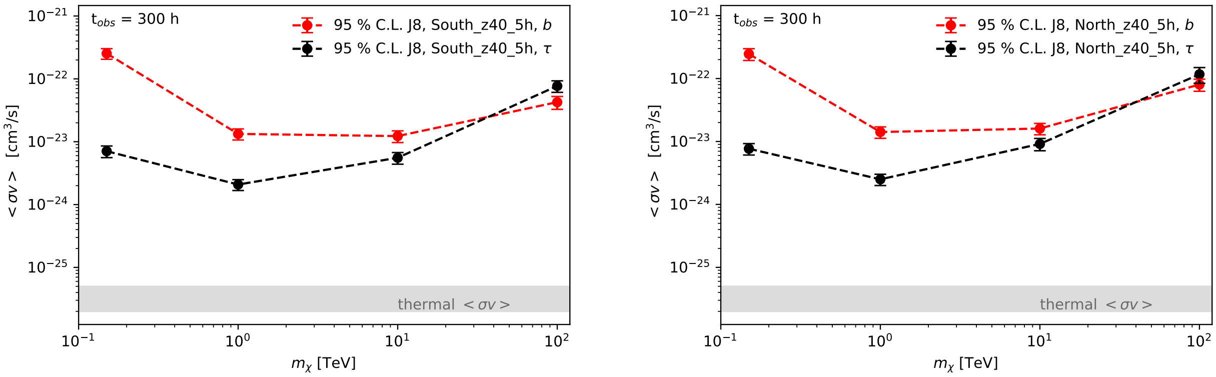

Figure 65 – Left (right) panel: The $\langle \sigma v \rangle$ values for a source with J_f = 95 % C.L. l. l. J8 in the south (north). The red line are the values for $b\bar{b}$, while black, for $\tau^+\tau^-$. The grey band represents the thermal values of $\langle \sigma v \rangle$.

Source: By the author

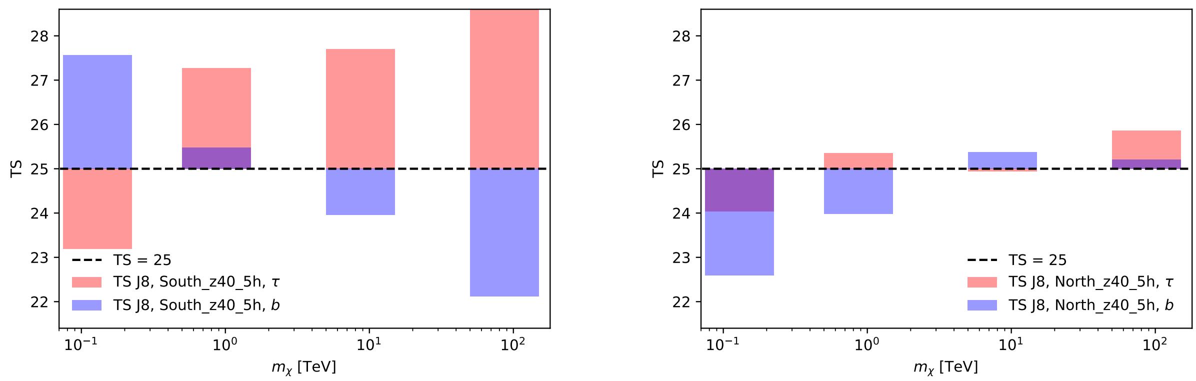

Figure 66 – Left (right) panel: The TS values for model J8 in the south (north) hemisphere. The $\tau^+\tau^-$ values are given in red and $b\bar{b}$ in blue. Source with J_f = 95 % C.L. l. l. J8.

Source: By the author

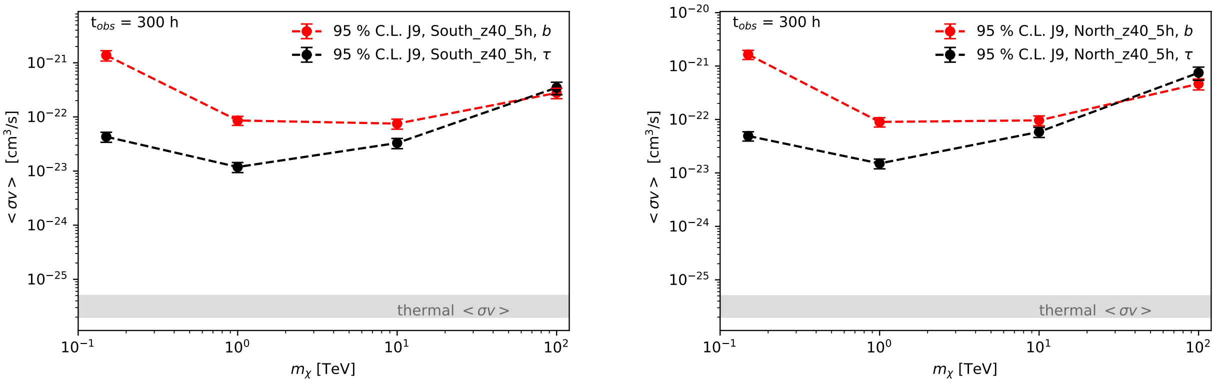

Figure 67 – Left (right) panel: The $\langle\sigma v\rangle$ values for a source with J_f = 95 % C.L. l. l. J9 in the south (north). The red line are the values for $b\bar{b}$, while black, for $\tau^+\tau^-$. The grey band represents the thermal values of $\langle\sigma v\rangle$.

Source: By the author

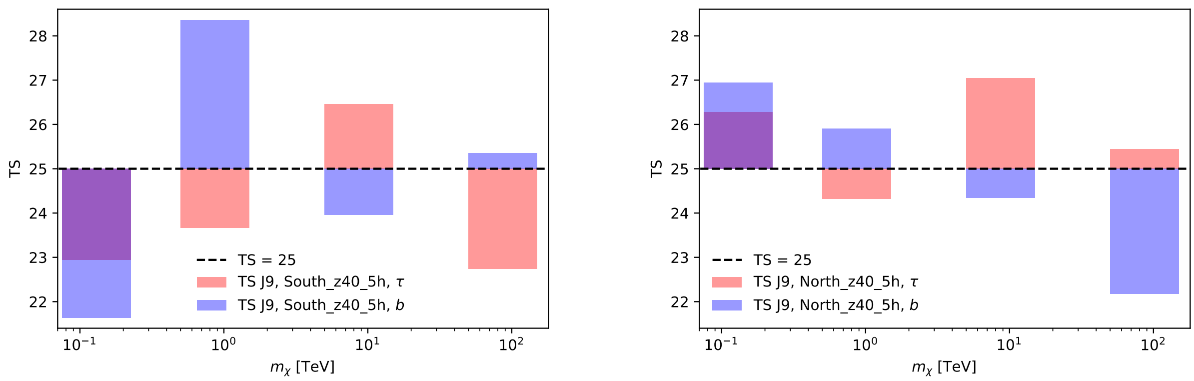

Figure 68 – Left (right) panel: The TS values for model J9 in the south (north) hemisphere. The $\tau^+\tau^-$ values are given in red and $b\bar{b}$ in blue. Source with J_f = 95 % C.L. l. l. J9.

Source: By the author

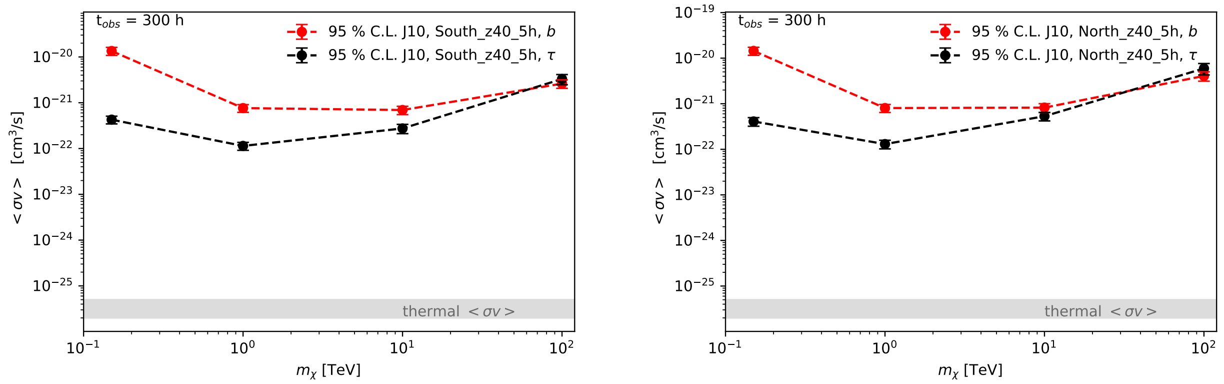

Figure 69 – Left (right) panel: The $\langle \sigma v \rangle$ values for a source with $J_f = 95$ % C.L. l. l. J10 in the south (north). The red line are the values for $b\bar{b}$, while black, for $\tau^+\tau^-$. The grey band represents the thermal values of $\langle \sigma v \rangle$.

Source: By the author

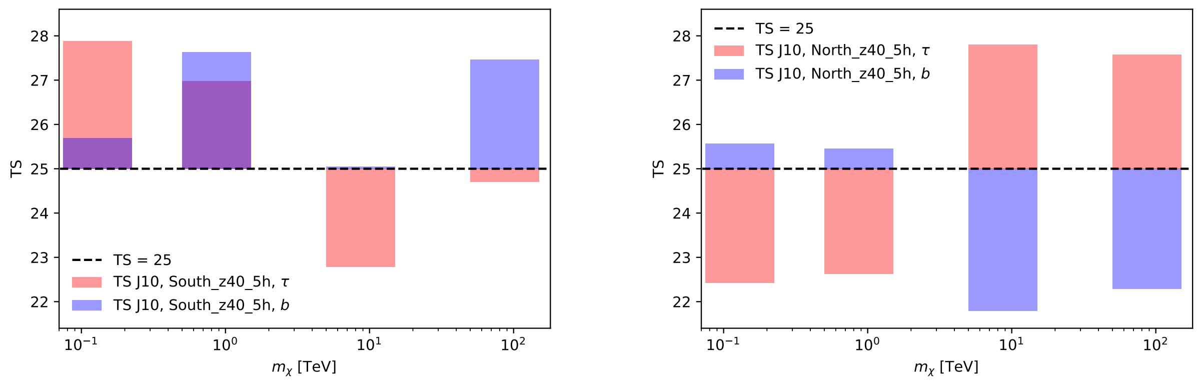

Figure 70 – Left (right) panel: The TS values for model J10 in the south (north) hemisphere. The $\tau^+\tau^-$ values are given in red and $b\bar{b}$ in blue. Source with $J_f = 95$ % C.L. l. l. J10.

Source: By the author